1-1-2012

Transformation Optics Using Graphene: One-Atom-Thick Optical Devices Based on Graphene

Ashkan Vakil
University of Pennsylvania, ashkan@seas.upenn.edu

Transformation Optics Using Graphene: One-Atom-Thick Optical Devices Based on Graphene

Abstract
Metamaterials and transformation optics have received considerable attention in the recent years, as they have found an immense role in many areas of optical science and engineering by offering schemes to control electromagnetic fields. Another area of science that has

been under the spotlight for the last few years relates to exploration of graphene, which is formed of carbon atoms densely packed into a honey-comb lattice. This material exhibits unconventional electronic and optical properties, intriguing many research groups across

the world including us. But our interest is mostly in studying interaction of electromagnetic waves with graphene and applications that might follow.

Our group as well as few others pioneered investigating prospect of graphene for plasmonic devices and in particular plasmonic metamaterial structures and transformation optical devices. In this thesis, relying on theoretical models and numerical simulations, we

show that by designing and manipulating spatially inhomogeneous, nonuniform conductivity patterns across a flake of graphene, one can have this material as a one-atom-thick platform for infrared metamaterials and transformation optical devices. Varying the graphene chemical potential by using static electric field allows for tuning the graphene conductivity in the terahertz and infrared frequencies. Such design flexibility can be exploited to create "patches" with differing conductivities within a single flake of graphene. Numerous photonic functions and metamaterial concepts are expected to follow from such platform. This work presents several numerical examples demonstrating these functions.

Our findings show that it is possible to design one-atom-thick variant of several optical elements analogous to those in classic optics. Here we theoretically study one-atom-thick metamaterials, one-atom-thick waveguide elements, cavities, mirrors, lenses, Fourier optics and finally a few case studies illustrating transformation optics on a single sheet of graphene in mid-infrared wavelengths.

Degree Type
Dissertation

Degree Name
Doctor of Philosophy (PhD)

Graduate Group
Electrical & Systems Engineering

First Advisor
Nader Engheta

Keywords
Graphene, Metamaterials, Photonics, Plasmonics, Transformation Optics

Subject Categories
Electrical and Electronics | Electromagnetics and Photonics | Physics

TRANSFORMATION OPTICS USING GRAPHENE: ONE-ATOM-THICK OPTICAL DEVICES BASED ON GRAPHENE

Ashkan Vakil

A DISSERTATION
in
Electrical and Systems Engineering

Presented to the Faculties of the University of Pennsylvania
in
Partial Fulfillment of the Requirements for
the Degree of Doctor of Philosophy

2012

Supervisor of Dissertation
Nader Engheta
H. Nedwill Ramsey Professor of Electrical and Systems Engineering

---

Graduate Group Chairperson
Saswati Sarkar
Professor of Electrical and Systems Engineering

Dissertation Committee:

Dwight L. Jaggard, Professor of Electrical and Systems Engineering

Cherie R. Kagan, Professor of Electrical and Systems Engineering

Alan T. Charlie Johnson, Jr., Professor of Physics and Astronomy

To my family and Samira,

for their unconditional love and support.

Acknowledgments

This thesis could not have been written without the support of my advisor and mentor, Professor Nader Engheta; I am truly indebted to him for his meticulous comments and his encouragements while I was writing this thesis. Professor Engheta taught me how to think independently and most importantly how to think "outside the box". Not only a great mentor, he has been a true friend throughout these years. His kindness will forever be of immense value to me.

I want to express my sincere gratitude to my committee members, Professors Dwight Jaggard, A. T. Charlie Johnson, and Cherie Kagan for their critical comments on my work and for their suggestions to improve quality of my research.

I am grateful to my friends and colleagues at Penn, who helped me in scientific aspects or otherwise during these years. Special thanks to Brian Edwards, Uday Chettiar and Marjan Saboktakin.

In addition, I would like to thank Professors Andrea Alú and Mário Silveirinha, who helped me a great deal with scientific research, and also my previous colleagues, Dr. Alessia Polemi and Dr. Olli Luukkonen for making the work environment fun and productive.

A special to thanks my friends, Pouya, Arash, Sina, Rouzbeh, Matteo and Chiara. With-

out them, my years in Philadelphia would not have been as pleasant.

And of course, my most deepest thanks to my parents, Farnaz and Farzin, for their everlasting love, and to my brother, Sam, who provided me with his unconditional support. I would not have made it this far without them...

Last but not least, I truly and deeply thank my girlfriend, Samira, for her love and endless patience, and for being by my side, even when I was irritable and frustrated...

ABSTRACT

TRANSFORMATION OPTICS USING GRAPHENE:
ONE-ATOM-THICK OPTICAL DEVICES BASED ON GRAPHENE

Ashkan Vakil

Nader Engheta

Metamaterials and transformation optics have received considerable attention in the recent years, as they have found an immense role in many areas of optical science and engineering by offering schemes to control electromagnetic fields. Another area of science that has been under the spotlight for the last few years relates to exploration of graphene, which is formed of carbon atoms densely packed into a honey-comb lattice. This material exhibits unconventional electronic and optical properties, intriguing many research groups across the world including us. But our interest is mostly in studying interaction of electromagnetic waves with graphene and applications that might follow.

Our group as well as few others pioneered investigating prospect of graphene for plasmonic devices and in particular plasmonic metamaterial structures and transformation optical devices. In this thesis, relying on theoretical models and numerical simulations, we show that by designing and manipulating spatially inhomogeneous, nonuniform conductivity patterns across a flake of graphene, one can have this material as a one-atom-thick platform for infrared metamaterials and transformation optical devices. Varying the graphene chemical potential by using static electric field allows for tuning the graphene conductivity in the terahertz and infrared frequencies. Such design flexibility can be exploited to create

“patches” with differing conductivities within a single flake of graphene. Numerous photonic functions and metamaterial concepts are expected to follow from such platform. This work presents several numerical examples demonstrating these functions.

Our findings show that it is possible to design one-atom-thick variant of several optical elements analogous to those in classic optics. Here we theoretically study one-atom-thick metamaterials, one-atom-thick waveguide elements, cavities, mirrors, lenses, Fourier optics and finally a few case studies illustrating transformation optics on a single sheet of graphene in mid-infrared wavelengths.

Contents

List of Figures

Chapter 1

Introduction

1.1 Metamaterials and transformation optics

1.1.1 Metamaterials

To build an electromagnetic (EM) device with certain functionalities, we need to be able to transmit, receive, confine, guide and manipulate EM waves. Over years, scientists and engineers have come up with myriad of brilliant designs and schemes to build devices performing these functions. For example antennas have been designed to transmit and receive waves, waveguides to confine and guide them, and polarizers and filters to manipulate them [7, 86]. All these are based on a central notion: exploiting "materials" to control, manipulate and direct fields and waves [12, 26, 83].

Although we are blessed with a wide range of materials in nature, the variety of devices that can be built from these materials is inevitably limited by spectrum of properties they exhibit. And indeed many desired electromagnetic properties, such as monopole magnets or negative refraction, seem to be missing in nature [12, 26]—or at least we have been

out of luck to find the materials exhibiting those desired properties. But why might these missing properties be important? An example may shed light on the significance of such properties. Let us take a look at the case of negative refraction.

Victor Veselago, in a paper published in 1967*, predicted if materials with simultaneously negative values of ϵ and μ – negative refractive index (NRI) or double-negative (DNG) materials – were ever found, they would exhibit unconventional properties unlike that of any known materials. For example for a plane wave in a DNG material the direction of the Poynting vector would be antiparallel to the direction of the phase velocity. The impact of such property can be tremendous; several interesting proposals can follow from such property. For instance consider perfect lensing [81] and subwavelength resonant cavities using DNG materials [22]. These examples indicate the wide scope of possibilities that can emerge from the missing properties in nature.

However no theory can be of much interest if the technology to realizing it is not available, and maybe that was why Veselago had to wait for a few decades to be praised for his work; his paper did not receive much attention at the time simply because no available material had negative ϵ and μ at the same time. But is there any physical law that precludes this possibility?

One region of frequency where permittivity and permeability attain negative values is around their resonance† as driving electric or magnetic field becomes out of phase with the huge polarization induced in the material—that is the electric and magnetic dipole moment cannot respond fast enough as the polarization of incident field flips. However materials with simultaneously negative ϵ and μ are not observed in nature simply because interestingly the fundamental electric and magnetic processes behind resonant phenomena, in materials we have identified so far, do not occur at the same frequencies [84]. The

*The English translation of the original paper was published in 1968 [111].

†In addition Drude permittivity of an electron gas can take negative values below plasma frequency.

Mother Nature leaves it for us to design structures that exhibit negative refractive index[‡].

The idea of artificially structuring composites or materials to exhibit certain properties is not new; the first attempts to build such composites can be traced back to the late nineteen century and first half of twentieth century [24, 26]. For example in late 1890's, Jagadish Chandra Bose explored twisted structure that could rotate the plane of polarization, resembling what today called chiral structures [24]. Or in 1914, Karl Ferdinand Lindman studied chiral media constructed from collection of wire helices [24]. Later in the 1940's, 1950's and 1960's, there were attempts to design and fabricate "artificial dielectric" for applications in lightweight lenses for microwave frequencies [24]. In the 1980's and 1990's, once again artificial complex materials and in particular chiral structures became subject of interest for building microwave components [21, 24].

However, due to the technological constraints, miniaturizing these structures has always been a challenge in this territory. Fortunately advances in nanotechnology and material sciences over the last couple of decades have removed some of the barriers and largely boosted our ability to fabricate different forms of materials and structures. Nowadays chemists and material engineers are able to tailor materials at atomic level. This capability allows for engineering materials with desired electromagnetic properties that might be missing or difficult to find in nature. And of course following such flexibility resides a continuum of novel ideas for electromagnetic and optical design. As a result, last few years we have witnessed resurrection of the field of "metamaterial" (in today's terminology).

Field of "metamaterial" has brought scientists and engineers from electromagnetics and material sciences to realize new classes of electromagnetic materials that are constructed by embedding subwavelength inclusions or inhomogeneities in a host medium rather than by controlling chemical composition. The geometrical characteristics (i.e., size and shape),

[‡]The first realization of an NRI material was in 2001 by a group from the University of California, San Diego [96].

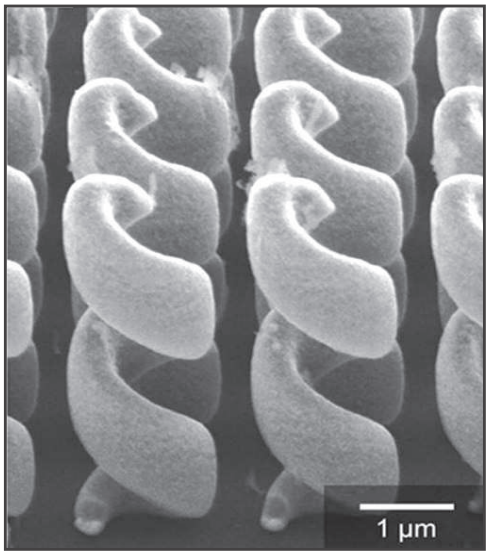

Figure 1.1: An example of a 3D optical metamaterial: uniaxial photonic metamaterial composed of three-dimensional gold helices arranged on a two-dimensional square lattice. This structure can act as a broadband circular polarizer [32]. The structure was realized by 3D direct laser-writing of helices in positive-tone photoresist. The polymer was removed by plasma etching, resulting in a square array of freestanding gold helices. Form Ref. 32 [J. K. Gansel et. al, "Gold helix photonic metamaterial as broadband circular polarizer", *Science* **325**, 5947 (2009)]. Reprinted with permission from the AAAS. [http://www.sciencemag.org/content/325/5947/1513].

periodicity, optical properties of these inclusions and inhomogeneities, and electromagnetic characteristics of host media determine the electromagnetic response of the composite materials or structures. Having control over these features the electromagnetic response of materials can be tuned at will to show a certain behavior desired by the electromagnetic design engineers. In essence, electromagnetic response of materials can be described by their effective permittivity and permeability, and depending on the value and sign of these two quantities, we can identify several classes of metamaterials: double-positive metamaterials, double-negative metamaterials, single-negative metamaterials ($\epsilon < 0$ and $\mu > 0$) or ($\epsilon > 0$ and $\mu < 0$), extreme-parameter metamaterials (for example epsilon-near-zero or epsilon-very-large metamaterials). These are materials with properties that may not be easily found in nature. Chirality and anisotropy are other material properties that can be tailored artificially to produce materials with desired optical response. A discussion of different metamaterial classes can be found in Refs. 12, 26 and 97. Figure 1.1 is an illustration of a 3D optical metamaterial fabricated by Wegener group in 2009 [32], indicating how nowadays scientists can fabricate sophisticated miniaturized metamaterial structures. This structure can act as a broadband circular polarizer.

We would like to conclude our brief discussion with a formal definition for metamaterials. As it appears the term metamaterials in the literature has been widely used and there is no universal definition for metamaterials. Cai & Shalaev [12] provide the following definition:

> *"A metamaterial is an artificially structured material which attains its properties from the unit structure rather than the constituent materials. A metamaterial has an inhomogeneity scale that is much smaller than the wavelength of interest, and its electromagnetic response is expressed in terms of homogenized material parameters."*

There are other equivalent definitions in the literature. In principle all these definitions refer to engineered structures that are constructed by embedding subwavelength inclusions in a host medium. Next we discuss transformation optics and its connection to metamaterials.

1.1.2 Metamaterials and transformation optics

As we mentioned in section 1.1.1, electromagnetic design is all about controlling and manipulating the EM fields and waves by exploiting materials in a proper way to reflect and refract and direct them to form desired patterns. Transformation optics offers a recipe to tailor material properties at subwavelength scale to exhibit a desired function [83]. Now the correspondence between transformation optics (TO) and metamaterials becomes clear. TO provides a design strategy and using metamaterials one can realize that design thanks to today's capacity in fabrication.

Transformation optics can be imagined as reverse-engineering of the optical device we seek. First the field lines in an empty space are transformed into a desired configura-

tion associated with the desired optical device [83]. Since Maxwell's equations are form-invariant, meaning that they maintain the same form in both coordinate systems [57, 83], the optical parameters for Maxwell's equations need to be scaled accordingly in the transformed coordinate system (coordinate system associated with the optical device). Then based on the transformation, the optical parameters (permittivity and permeability) for realizing the optical device can be retrieved. A famous example of transformation optics is the optical cloak [83], although this technique has other profound applications in optical design. For example later in chapter 3, we show an example of transformation optics that might find application in optical signal processing.

There have been a large interest and several developments in transformation optics since its official introduction in 2006. A recent review is given in Ref. 82. In particular transformation optics has been successfully applied to plasmonic systems to control propagation of special type of electromagnetic wave called surface plasmon-polariton (SPP) surface waves [44].

In this work our goal is to show that "graphene", which is a monolayer of carbon atoms, can serve as a new platform for *plasmonic metamaterials* and *transformation optical devices* owing to its exotic features and the design freedom it offers. Before talking about graphene, however, we would like to get a perspective of the field of plasmonics. What is an SPP surface wave? And why might graphene be a better platform for plasmonic metamaterials rather than noble metals such as silver and gold that, conventionally, have long been the favorite choices in this territory?

1.2 Integration of electronics and photonics: plasmonics as a bridge

The goal of electronic engineers has always been design of miniaturized devices that are light, cheap, low power and of course equally important fast in processing and transmitting information. Since revolutionary invention of integrated circuits (ICs) by Jack Kilby in 1959, electronics has certainly come a long way: from 7/16-by-1/16-inches IC that Kilby built to today's nanoscale electronics [51]. As Moore predicted [70], the number of transistors in integrated circuits has continuously and rapidly grown since the invention of ICs, suggesting that we have been able to process data faster without considerably increasing the size of the electronic circuits. This indicates how flourishing this field has been over the past few decades. But it seems that over the last couple of years (since 2005 [102]) we have not seen stunning improvements in microprocessors. This raises the question that whether we are approaching a plateau in rate of processing per volume. If so, what is the reason?

The answer can be traced back to constant-field scaling rule, which tells us that the voltage for operation of transistors must decrease in line with downscaled dimensions of transistors. But downscaling dimensions might be possible to a certain level, after which the minimum gate voltage-swing necessary to switch the device from "off" state to "on" state could be just too small. From design perspective this means either excessive leakage current (dissipation) in the "off" state or low current – slow circuits – in the "on" state [102]. Neither is favorable. So how can we overcome this obstacle?

Integration of electronics and photonics is one promising solution to go around this hurdle [78]. Photonic devices are generally faster simply because they carry higher frequency optical signals, enabling faster signal processing compared with electronic devices. For years Silicon has been the favorite choice for optoelectronics devices, bringing elec-

tronics and photonics under one umbrella. Probably one of the most important reasons for this popularity is the promise of Silicon for integration of electronics and photonics. But yet, further downsizing Silicon-photonics devices may not be a straightforward task, since some of these devices such as optical waveguides are necessarily bulky to carry volumetric waves. This hampers the progress toward integration of these two technologies and limits the extent of downscaling. Emerging field of nanoplasmonics, which is a major part of the field of photonics, can resolve this issue by providing a collection of techniques to confine light waves at scales much smaller than the wavelength. Nanoplasmonics then allows for design of elements (e.g., waveguide) that are much smaller than their photonic counterparts and facilitate integration of two technologies. Field of plasmonics deals with engineering of surface plasmons, exactly as electronics and photonics is science of manipulation of electrons and photons, respectively. So what are surface plasmons?

Surface plasmons are collective oscillation of electrons at an interface between two media whose values of the real part of permittivity have different signs [63]. If the light incident on such an interface can couple with these surface-plasmons, the result is a highly confined propagating electromagnetic wave known as surface plasmon polariton (SPP) surface wave. Thanks to advances in nanofabrication, nowadays ultra-small plasmonics systems, even as small as few hundreds of nanometers, are feasible [10]. The concept of metamaterials can also be applied to plasmonics structures; one can tailor electromagnetic properties of a plasmonic material or structure to obtain a certain response from the system.

Owing to their ability to support the surface-plasmon polariton surface waves, in the infrared and visible regimes, the noble metals, such as silver and gold, have been popular materials in constructing plasmonic systems and many metamaterial structures [12]. As our discussion to this point might hint, the key concept in design of metamaterials and transformation optical devices is “tunability”. However, tuning permittivity functions of noble metals is not an easy task. In addition the existence of material losses, especially

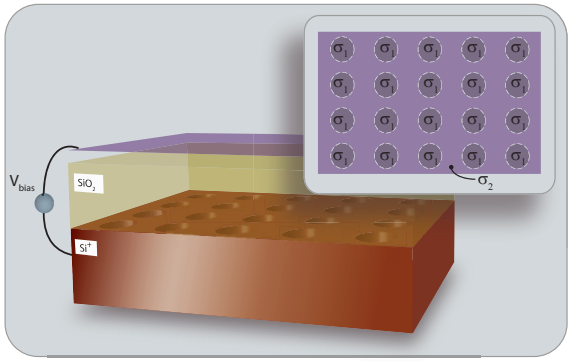

Figure 1.2: Concept of graphene metamaterial: Can we have metamaterials and transformation optics on graphene merely by varying its local conductivity?

at visible wavelengths, degrades the quality of the plasmon resonance and limits the relative propagation lengths of SPP waves along the interface between metals and dielectric materials.

These deficiencies limit the functionality of some of available metamaterials and transformation optical devices. In this work, we show that graphene can serve as a new platform for metamaterials and transformation optical devices that can, under certain conditions, alleviate these issues. Overall there are three features that make graphene an excellent choice for these purposes at least for mid-IR wavelengths

- ***Tunability***: Most probably tunability of graphene is the most exciting feature of this exotic material. We will see in chapter 2 that graphene conductivity can be controlled using chemical doping or static electric bias. The basic idea is that whether we can tailor behavior of a single layer of graphene by changing its conductivity locally and inhomogeneously (see Fig. 1.2). The ability to control and vary graphene optical properties offers flexibility in design of electromagnetic systems based on graphene.

- ***Integration***: After its first isolation in 2004 [76], graphene has been in spotlight for its exotic electronic transport properties [74, 75] and suitability for optoelectronic applications [5, 13, 69, 80, 88, 114]. As this work and several others show [41, 47,

54], graphene is also an excellent platform for plasmonics applications, suggesting prospects for graphene as the bridge between electronics and plasmonics.

- ***Low material losses***: As our studies show (see section 2.2.1) graphene has low material losses, qualifying this one-atom-thick layer as a host for electromagnetic and optical systems. It is worth mentioning that, in a recent article, Tassin et. al [101] claim that graphene losses are considerable and thus the propagation length of the SPP waves along graphene is at best just less than $3\lambda_{\mathrm{SPP}}$ for IR frequencies. Their conclusion is based on experimental results presented in Ref. 58, in which the reported real part of the conductivity, which accounts for losses, is relatively large. However graphene losses are dependent on the fabrication processes; cleaner graphene samples might result in lower losses and higher propagation lengths. To address this objection, Tassin et. al use conductivity values reported in two theoretical papers that predict large values for the real part of conductivity [36, 85]. It may not be fair to draw such a general conclusion based on only two theoretical papers, whose their results have not been confirmed by any experiments. Interestingly for the frequency region of interest in this thesis, for typical values of chemical potential, the real part of the conductivity reported by Ref. 58 (experimental paper) is much less than the one reported in Ref. 36 (theory paper). This brings into question the general conclusion of Tassin et. al in Ref. 101 that graphene is not a good host for surface plasmon polaritons. The absolute resolution of this debate is remained unanswered until further experiments are conducted in the future.

In addition, in recent years we have observed a rapid growth in graphene nanofabrication capabilities that can facilitate realization of ultra-compact photonic and plasmonic devices based on this material.

Before we start our formal discussion, it is laudable to give a brief review of literature relevant to our proposal.

1.3 Literature Review

Graphene is a mono-layer of carbon atoms arranged in a 2-dimensional hexagonal lattice. Grapahene was first isolated by Andre Geim and Konstantin Novolselov in 2004 and later in 2010 they were awarded the Nobel Prize in Physics for their groundbreaking work on graphene. Since 2004, there has been an explosion of interest in this unconventional material (and expectedly after 2010, when the Nobel Prize was awarded – see Fig. 1.3).

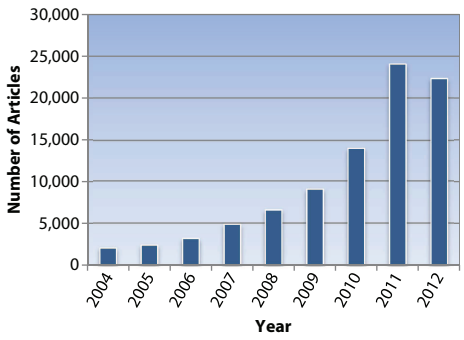

Figure 1.3: Number of articles and books on graphene since first isolation in 2004 – data is collected from Google Scholar™ search engine.

It might be difficult to review all the developments in the areas of graphene photonics, optoelectronics and plasmonics, so we only go over those that are more relevant to our work.

Tunable plasmonics devices: In Ref. 54, Koppens et. al show that owing to graphene's low loss (in certain regions of spectrum), tunability and its capability to support highly confined surface plasmons, one can envision new possibilities for light-matter interactions at the nanoscale that may not be constrained by obstacles that are associated with using noble metals. Consequently graphene can be a new platform for novel low-power, ultrafast classical and quantum optical devices.

Terahertz tunable plasmonics metamaterials: Ju et. al [50] investigate plasmon excitations

in an array of graphene micro-ribbon, which might represent a simple form of a graphene terahertz metamaterial. They show that plasmon resonances peak can be tuned across a wide range of terahertz frequency by varying width of the micro-ribbons or doping. Following this experimental work, Nikitin et. al [73] offer a theoretical study of the problem. They specifically study the transmission, reflection, and absorption resonance spectrum of the ribbons. They argue that the resonances are due to the leaky plasmonic modes existing in individual ribbons. In another related study, Thongrattanasiri et. al [103] examine possibility of 100% light absorption using a patterned layer of doped graphene. Specifically, they show that arrays of doped graphene nanodisks can result in complete absorption when lying on a dielectric-coated metal with the proper choice of thickness for the dielectric on top of the metal. Interestingly complete absorprion scenario using such geometry is almost independent of the angle of incidence and polarization. The physical mechanism for this phenomenon is similar to that for the total absorption using a Salisbury sheet [29]. An IBM group (Yan et. al [117]) report on fabrication of photonic devices composed of graphene/insulator stacks supporting plasmon resonances differing from that of a single layer graphene. They show that carrier concentration dependence of resonance peak and magnitude is stronger for the stack compared with the case of a single layer. Additionally they realize a broadband tunable far-infrared notch filter by using a stack of patterned graphene/insulator (the graphene layers are patterned into arrays of microdisks). This work can be a foundation for developing mid- and far-infrared photonic devices (e.g., detectors, modulators and three-dimensional metamaterial systems).

Photonic and optoelectronics devices: Inspired by exotic optoelectronic characteristics of graphene, many research groups have exploited this material for broadband photonic and optoelectronic applications, such as polarizers and modulators.

- *Graphene polarizer:* Kim and Choi [52] have experimentally demonstrated waveg-

uiding using graphene strips at wavelength 1.31 μm. They have managed to transmit a 2.5 Gbps optical signal successfully via 6 mm-long graphene waveguides. As we will see in chapter 2, depending on its carrier density graphene can support two kinds of polarization for SPP: TE and TM. This dependence forms the basis for developing waveguides that support either TE or TM waves. Such waveguiding component can be used as a polarizer to transform unpolarized incident wave into polarized wave. Based on this notion Bao et. al [9] have fabricated a graphene/silica hybrid waveguide that only supports TE waves and as a result it filters out the TM polarized waves (TE-pass polarizer). As we will see in the present work, doping the graphene layer above a certain level enables this atomically thin layer to support TM waves, while TE waves are not supported anymore. Such component might then be used as a TM-pass polarizer since it can filter out TE waves.

- *Graphene modulator:* Liu et. al [60] have experimentally demonstrated a broadband graphene-based optical modulator that can operate between 1.35 μm to 1.6 μm. The proposed device is as small as 25 μm^2 and operated by electrically tuning the carrier concentration (chemical potential) of the graphene layer. Based on this mechanism, authors achieved modulation bandwidth of 1.2 GHz at 3 dB. In a follow-up work the same group improve efficiency of their device by using bi-layer graphene (two layers of graphene and an oxide layer in between), achieving modulation depth of 0.16 dB/μm [61]. The fundamental idea behind this type of modulation is modulating the interband transitions (modulating between TM-supporting and TE-supporting modes). However one can, as well, modulate the intraband transitions, which forms the basis for the proposal by Anderson in Ref. 5 – the modulation can be realized using static electric gating. This theoretical study builds upon dependence of plasmon losses (intraband losses) in mid-IR on the level of carrier concentrations (chemi-

cal potential). Theoretically the modulation based on plasmon losses should enable higher switching speeds as the relaxation time for intraband carriers are longer than that for interband carriers. The experimental verification of this type of modulators is reported in Ref. 95.

In addition other optoelectronic elements such as photodetector, saturable absorber and limiters have been designed and fabricated based on graphene (see Ref. 8 for a review of these components).

It is also worth mentioning of the proposal "graphene-based soft hybrid optoelectronic systems" by Kim et. al [53]. Among various exotic characteristics of graphene is its tensile strength, which might enable a futuristic category of graphene-based optoelectronic devices that could be flexible, stretchable, and foldable. As a proof of concept for their proposal, Kim et. al have fabricated a graphene-based plasmonic waveguide and a waveguide polarizer for wavelength 1.3 μm that can be used for realization of optical interconnection in flexible human-friendly optoelectronic devices.

Lastly, once again we would like to point out that there are many exciting proposed novel ideas and studies that are left out of this review, as we did not intend to cover all the literature available on the topic of graphene, but only those studies that are more relevant to the present work—there are definitely several excellent proposals that we did not refer to (for example cloaking using graphene [15]), but reviewing all these studies appears to be out of scope of the present work.

Chapter 2

Theoretical Background

As discussed in chapter 1, our goal is to bring several concepts and functions already developed in the field of metamaterials and transformation optics on to the graphene. In this chapter we will explore the theoretical background that forms the basis for this proposal.

We start our study by discussing a complex conductivity model for graphene, which we will use to study interaction of electromagnetic waves with graphene. We then continue the discussion by elaborating on propagation of surface plasmon-polariton surface waves across the graphene and how the luxury to tune the graphene conductivity can provide a degree of freedom to manipulate and route light signals on this exotic platform.

2.1 Complex conductivity model for graphene

2.1.1 Analytic expression for complex conductivity

In its most general form, the graphene sheet can be modeled as an infinitesimally-thin, non-local two-sided surface characterized by a magneto-optical surface complex conductivity

tensor [28, 37–39] (see Appendix A for a brief analogy between graphene conductivity and circuit equivalent). The elements of this tensor can be derived from microscopic, semi-classical and quantum mechanical considerations. A large body of recent literature focuses on different techniques to model complex conductivity of graphene, however thorough review of this literature is not in scope of this work. We will just briefly mention and review the well-known model we have utilized in our studies.

To begin, let us assume that a graphene layer is suspended in free space in the *x*-*y* plane*. An extended non-local anisotropic model for conductivity follows the tensor form [39, 42]

$$\overleftrightarrow{\sigma}(\omega, \mu_c(\mathbf{E_0}), \Gamma, T, \mathbf{B}_0) = \hat{\mathbf{x}}\hat{\mathbf{x}}\sigma_{xx} + \hat{\mathbf{x}}\hat{\mathbf{y}}\sigma_{xy} + \hat{\mathbf{y}}\hat{\mathbf{x}}\sigma_{yx} + \hat{\mathbf{y}}\hat{\mathbf{y}}\sigma_{yy}, \tag{2.1}$$

where ω is radian frequency, Γ is charged particle scattering rate representing the loss mechanism, T denotes temperature, and μ_c is chemical potential. $\mathbf{E}_0$ and $\mathbf{B}_0$ are respectively the dc electric and magnetic bias field. In general the scattering rate Γ can be function of frequency, temperature, field and the Landau level index. The chemical potential, which is related to density of charged carriers, can be controlled by chemical doping [113] or by applying dc bias field ($\mathbf{E}_0 = \hat{\mathbf{z}}E_0$) [76].

Noting that $\sigma_{xx} = \sigma_{yy}$ and $\sigma_{xy} = -\sigma_{yx}$, we can rewrite Eq. (2.1) as following

$$\overleftrightarrow{\sigma}(\omega, \mu_c(\mathbf{E}_0), \Gamma, T, \mathbf{B}_0) = \sigma_d\overleftrightarrow{\mathbf{I}}_t + \sigma_o\overleftrightarrow{\mathbf{J}}_t, \tag{2.2}$$

where σ_d and σ_o are, respectively, the diagonal and off-diagonal (Hall) conductivities, and $\overleftrightarrow{\mathbf{I}}_t = \hat{\mathbf{x}}\hat{\mathbf{x}} + \hat{\mathbf{y}}\hat{\mathbf{y}}$ and $\overleftrightarrow{\mathbf{J}}_t = \hat{\mathbf{x}}\hat{\mathbf{y}} - \hat{\mathbf{y}}\hat{\mathbf{x}}$ are the symmetric and antisymmetric dyads. Following Kubo formalism†, in Eq. (2.2), in the presence of both electric potential and magnetic bias field,

*In this work we always consider the case of free-standing graphene in free-space, unless otherwise stated. The physical concepts introduced here remain unaffected when graphene lies at the interface of two different media with different permittivites and permeabilities. Further discussion on this issue will follow in the future sections.

†This formalism is within the linear response theory. Other techniques within this theory such as the random phase approximation (RPA), or the self-consistent-field approach result in the same qualitative optical response [47].

one can obtain [39]

$$\begin{aligned}\sigma_d = & \frac{e^2 v_F^2 |eB_0| \hbar \left(\omega + i2\Gamma\right)}{i\pi} \\ & \times \sum_{n=0}^{\infty} \left\{ \left(1 - \frac{\Delta^2}{M_n M_{n+1}}\right) \frac{[n_F(M_n) - n_F(M_{n+1})] + [n_F(-M_{n+1}) - n_F(-M_n)]}{(M_{n+1} - M_n)^2 - (\omega + 2i\Gamma)^2} \right. \\ & \times \frac{1}{M_{n+1} - M_n} + \left(1 + \frac{\Delta^2}{M_n M_{n+1}}\right) \\ & \left. \times \frac{[n_F(-M_n) - n_F(M_{n+1})] + [n_F(-M_{n+1}) - n_F(M_n)]}{(M_{n+1} + M_n)^2 - (\omega + 2i\Gamma)^2} \frac{1}{M_{n+1} + M_n} \right\}, \end{aligned} \tag{2.3}$$

and

$$\begin{aligned}\sigma_o = & -\frac{e^2 v_F^2 eB_0}{\pi} \sum_{n=0}^{\infty} \left([n_F(M_n) - n_F(M_{n+1})] + [n_F(-M_{n+1}) - n_F(-M_n)]\right) \\ & \times \left\{ \left(1 - \frac{\Delta^2}{M_n M_{n+1}}\right) \frac{1}{(M_{n+1} - M_n)^2 - (\omega + 2i\Gamma)^2} \right. \\ & \left. + \left(1 + \frac{\Delta^2}{M_n M_{n+1}}\right) \frac{1}{(M_{n+1} + M_n)^2 - (\omega + 2i\Gamma)^2} \right\}, \end{aligned} \tag{2.4}$$

where $n_F(\epsilon) = 1/\left\{1 + \exp\left[(\epsilon - \mu_c)/(k_B T)\right]\right\}$ is the Fermi-Dirac distribution, $v_F = 10^6$ m/s is the Fermi velocity, $M_n = \sqrt{\Delta^2 + 2n\hbar v_F^2 |eB_0|}$ is the energy of the nth Landau level (this formalism assumes $e^{-i\omega t}$ time harmonic dependence) and Δ is the excitonic band gap. Also note that we have assumed scattering rate Γ is not dependent on frequency and Landau level index. In the low magnetic field limit, it is fair to assume $\Delta = 0$. As such Eqs. (2.3) and (2.4) can be simplified to

$$\begin{aligned}\sigma_d = & -\frac{ie^2 \left(\omega + 2i\Gamma\right)}{\pi\hbar^2} \left[\frac{1}{\left(\omega + 2i\Gamma\right)^2} \int_0^{\infty} d\epsilon \left(\frac{\partial n_F(\epsilon)}{\partial \epsilon} - \frac{\partial n_F(-\epsilon)}{\partial \epsilon} \right) \epsilon \right. \\ & \left. - \int_0^{\infty} d\epsilon \frac{n_F(-\epsilon) - n_F(\epsilon)}{\left(\omega + 2i\Gamma\right)^2 - 4\left(\epsilon/\hbar\right)^2} \right], \end{aligned} \tag{2.5}$$

and

$$\sigma_o = -\frac{e^2 v_F^2 eB_0}{\pi\hbar^2} \left[\frac{1}{\left(\omega + 2i\Gamma\right)^2} \int_0^{\infty} d\epsilon \left(\frac{\partial n_F(\epsilon)}{\partial \epsilon} + \frac{\partial n_F(-\epsilon)}{\partial \epsilon} \right) + \int_0^{\infty} d\epsilon \frac{1}{\left(\omega + 2i\Gamma\right)^2 - 4(\epsilon/\hbar)^2} \right]. \tag{2.6}$$

In our studies we assume no magnetic bias field, so the off-diagonal terms vanish for $B_0 = 0$ and graphene can be assumed to be isotropic. The diagonal terms however, as can be seen from Eq. (2.5), are independent of the dc magnetic field.

The first term in Eq. (2.5) is due to intraband contributions and the second term is related to interband transitions. The intraband term can be analytically evaluated as [39, 41]

$$\sigma_{d,\,\text{intra}} = i\frac{e^2 k_B T}{\pi\hbar^2\,(\omega + i2\Gamma)}\left[\frac{\mu_c}{k_B T} + 2\ln\left(e^{-\frac{\mu_c}{k_B T}} + 1\right)\right]. \tag{2.7}$$

This has the familiar Drude form that describes the collective behavior of free electrons (intraband transitions).

Although in general the interband term cannot be evaluated analytically, when $k_B T \ll |\mu_c|$ and $k_B T \ll \hbar\omega$, an approximate analytic expression for this term is given in literature [40]

$$\sigma_{d,\,\text{intra}} \approx \frac{ie^2}{4\pi\hbar}\ln\left(\frac{2|\mu_c| - (\omega + i2\Gamma)\,\hbar}{2|\mu_c| + (\omega + i2\Gamma)\,\hbar}\right). \tag{2.8}$$

As can be seen from Eq. (2.8) for low values of scattering rate (low loss), for $2|\mu_c| > \hbar\omega$ the interband contribution is purely imaginary (this imaginary part is negative), while for $2|\mu_c| < \hbar\omega$, that term is complex with the real part taking the value $\frac{\pi e^2}{2h}$ and the imaginary part still taking negative values (further discussion on importance of sign of the imaginary part will be presented in the following sections).

2.1.2 Numerical results for optical conductivity

In this part, we present some numerical results for optical conductivity based on the Kubo formalism just reviewed above. Throughout this discussion we assume a constant scattering rate $\Gamma = 0.43$ meV[‡]. Fig. 2.1, **A** and **B**, shows real and imaginary parts of graphene

[‡]As Gusynin et al. point out, constant value for Γ is a good assumption in practice and results are in good agreement with more general cases considered in previous other works [39]. Also the value we have chosen here is adapted from other references [37, 39].

conductivity for $\Gamma = 0.43$ meV and temperature $T = 3^\circ$ K[§]. Also in panels **C** and **D**, we repeat the same plots for room temperature ($T = 300^\circ$ K).

As can be seen from Fig. 2.1, for low temperatures, there are regions of frequencies and chemical potentials for which $\sigma_{g,i} < 0$, whereas for other regions $\sigma_{g,i} > 0$. As we will discuss in detail in section 2.2, when $\sigma_{g,i} > 0$ a mono-layer of graphene can effectively behave as a very thin "metal" layer, supporting a transverse-magnetic (TM) electromagnetic surface plasmon-polariton (SPP) surface wave [41, 47, 67, 107].

Since we are mostly interested in the frequency band 28 to 32 THz[¶], we take a closer look at the graphene conductivity and its inter- and intra-band contributions in this band. Figure 2.2, **A** and **B**, demonstrates total complex conductivity of graphene as a function of frequency for different values of chemical potential at $T = 3^\circ$ K. In panels **C** and **D** we have demonstrated values of conductivity in the region that will be mostly dealt with throughout this work. As can be seen, in the frequency band 28 to 32 THz, for $\mu_c = 150$ meV and 300 meV, the imaginary part of the conductivity is positive, while for $\mu_c = 0$ meV and $\mu_c = 65$ meV, this quantity is respectively zero and negative.

Figure 2.3, **A** and **B**, depicts the complex conductivity due to inter- and intra-band transitions at low temperature ($T = 3^\circ$ K). The intraband contribution follows a Drude form and, in mid-IR region, results in lower losses compared to interband contribution, which shows higher losses for higher energies due to lossy interband transitions. We note that at much lower frequencies, the loss of Drude contribution becomes larger. For example for $\mu_c = 150$ meV the transitions happen for frequencies large than approximately 72.4 THz, i.e., high-enough energy electrons are able to make the interband transition. These transitions are lossy and as we can see in Fig. 2.3, **A**, for frequencies higher than 72.4 THz, we have considerable amount of loss. An interesting feature of interband is that

[§]This temperature is readily achievable in most experimental laboratories as these days one is more concerned about much lower temperatures, e.g., micro-, nano- and even pico-Kelvins [55].

[¶]We are interested in this region of frequency because CO_2-based lasers operate in this region.

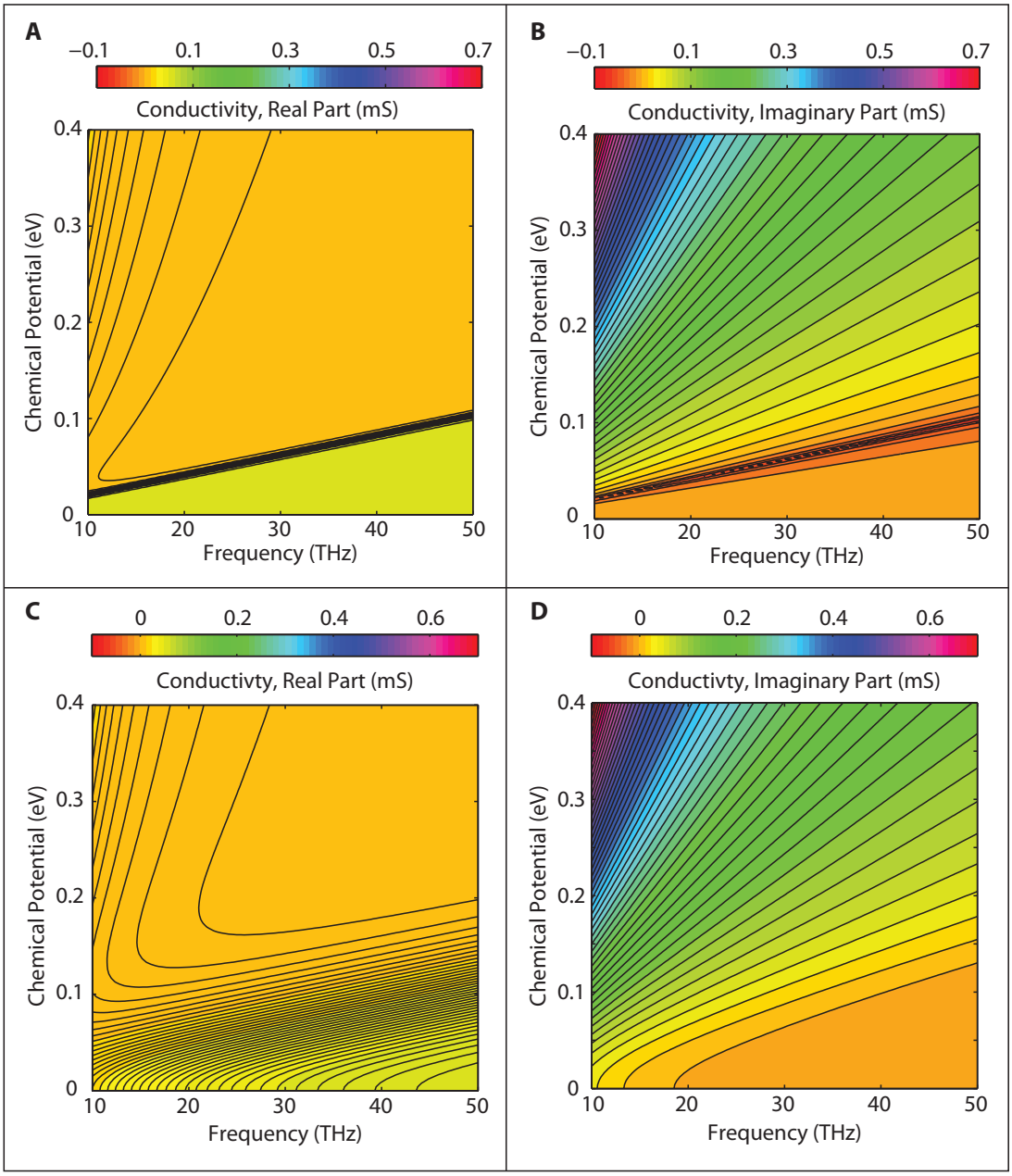

Figure 2.1: Real and imaginary part of the conductivity. Panel **A** and **B** respectively display real and imaginary part of the conductivity as a function of the chemical potential and frequency ($T = 3°$ K, $\Gamma = 0.43$ meV), following the Kubo formula [39]. Panel **A** and **B** are reprinted from Ref. 106 (by permission of the AAAS). [http://www.sciencemag.org/content/332/6035/1291]. Panel **C** and **D** show the same but for room temperature ($T = 300°$ K).

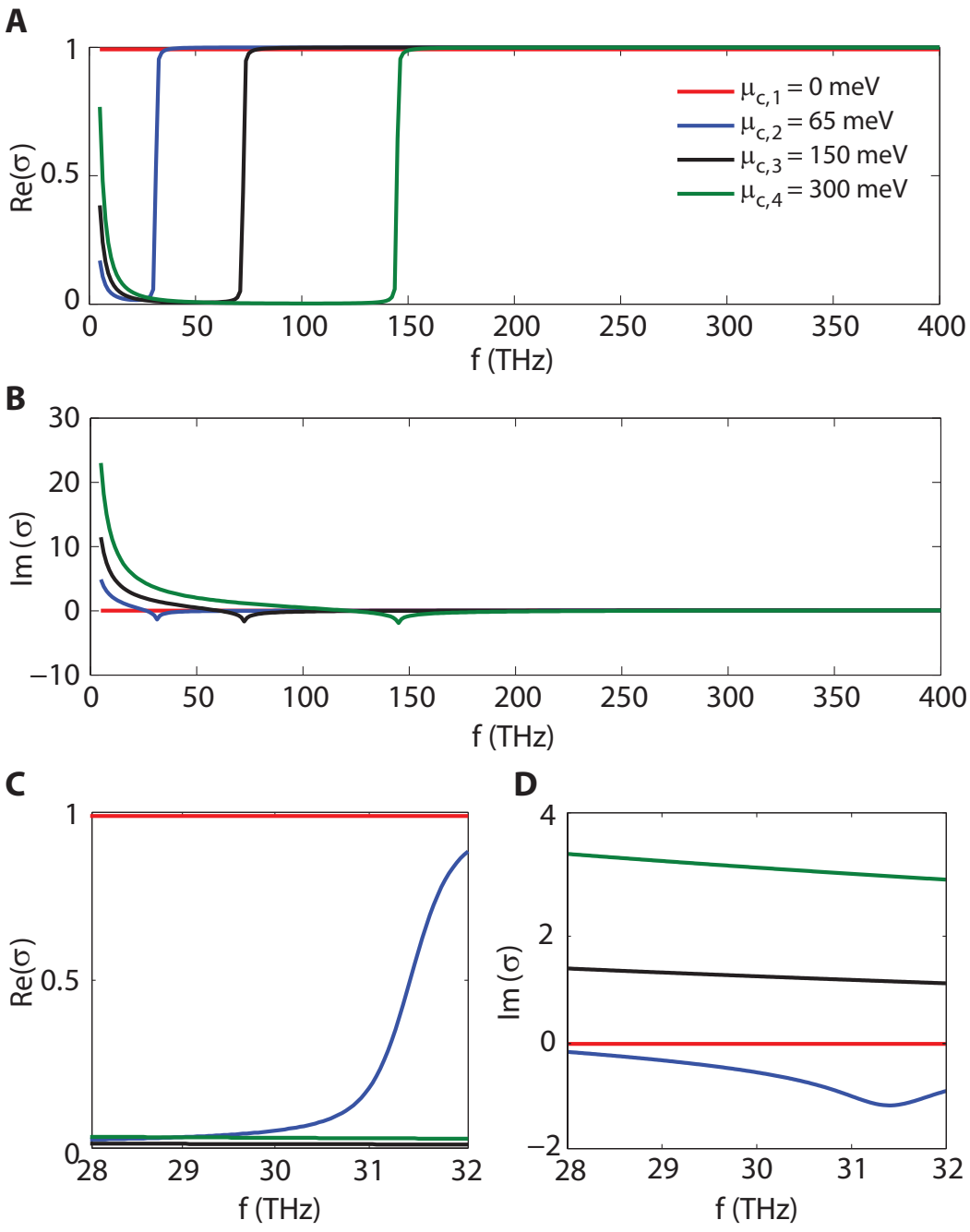

Figure 2.2: Complex conductivity as a function of frequency for different values of chemical potential at $T = 3°$ K normalized to $\sigma_{\text{min}} = \frac{\pi e^2}{2h}$. Panels **A** and **B** show the real and imaginary part of conductivity for the frequency range 5 to 400 THz, while panels **C** and **D** display the portion of mid infra-red region in which we are interested.

for energies ($\hbar\omega$) lower than $2\mu_c$, the real part of conductivity, which represents losses in graphene, is vanishing whereas for $\hbar\omega > 2\mu_c$ this quantity is approximately always equal to $\sigma_{\min} = \frac{\pi e^2}{2h} \approx 6.085 \times 10^{-2}$ mS. Note that in Figs. 2.2 and 2.3 the values of real and imaginary parts of conductivity are normalized to $\sigma_{\min}$. These numerical results (obtained from Kubo formula) are in good agreement with experimental results in Refs. 58 and 64— For low frequencies the experimental results tend to show higher losses compared with Kubo formula prediction [59]. However the amount of loss can be highly dependent on the fabrication process.

It is worth mentioning that for frequencies higher than $\approx$ 50 THz ($\hbar\omega$ = 200 meV), plasmons decay channel via emission of optical phonons together with electron-hole pairs (second-order process) is open, resulting in a shorter relaxation time τ and a higher scattering rate Γ ($\tau^{-1} = 2\Gamma$) [47]. As pointed out in this work the frequency range of interest is form 28 to 32 THz, so we are not in the regime in which this second order process is active (of course neither is the interband losses).

Lastly, before we transition our discussion to the theory underpinning SPP surface waves on the graphene, we would like to briefly mention about two issues regarding graphene conductivity:

(i) *Nonlinearity of optical conductivity of graphene:* It has been shown that graphene can exhibit strongly non-linear electromagnetic response especially in Terahertz regime [66, 68, 115]. For frequencies up to 30 THz, in Ref. 68, assuming an external electric field $\mathbf{E}^{\text{ext}}(t) = \mathbf{E}_0 \cos \omega t$, Mikhailov & Ziegler show that nonlinearity effects emerge when

$$E_0 \gg \frac{\hbar\omega \sqrt{\pi n_s}}{e}, \tag{2.9}$$

where $E_0 = |\mathbf{E}_0|$ and n_s denotes the charge carrier density ($\sim 10^{11}$ cm^{-2}). According to this condition, graphene exhibits nonlinearity in the far-infrared to terahertz regime for electric fields higher than $\sim$ 300–10^3 V/cm and for room temperature [68]. For

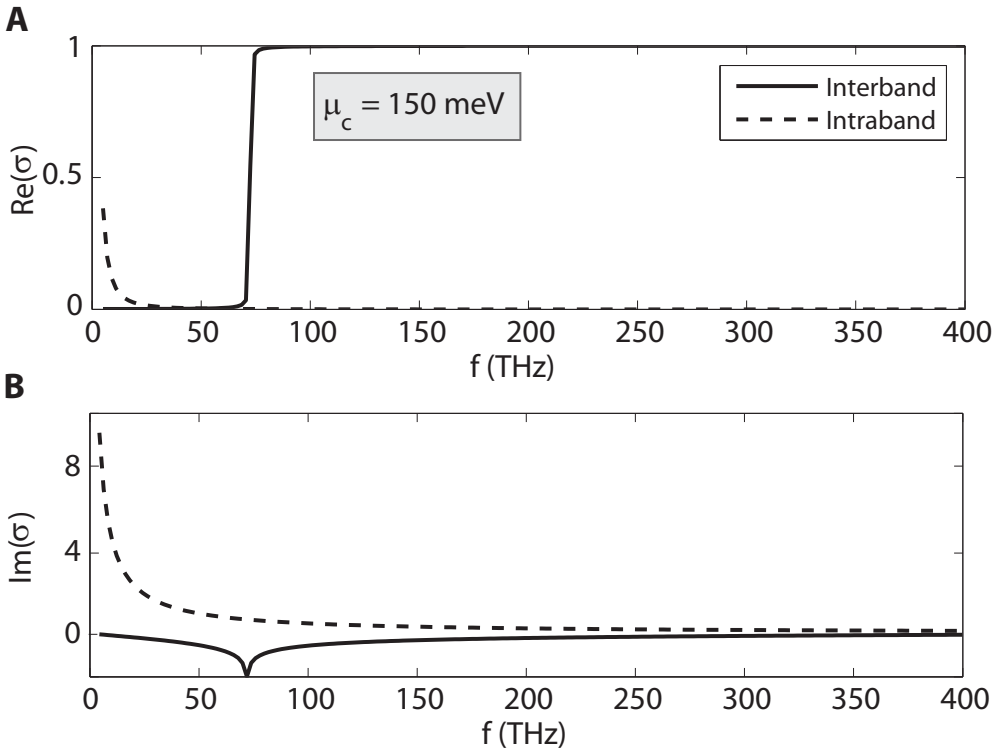

Figure 2.3: Contribution of inter- and intra-band transitions to graphene conductivity for $\mu_c = 150\ meV$ and $T = 3°$ K. Values are normalized to $\sigma_{\min} = \frac{\pi e^2}{2h}$. Clearly the intraband contribution has the familiar form of Drude, while the interband transition results in higher real part of conductivity for sufficiently high energies (i.e., higher losses for higher frequencies).

mid-IR the required electric field is even higher (as the required electric field grows linearly with ω). In our study we assume the amplitude of excitation is less than values mentioned here so we do not account for the nonlinearity effect.

(ii) *Kramers-Krönig relation of graphene conductivity:* As we know any physical system must have an analytic response function due to causality of input-output of the system, resulting in the familiar Kramers-Krönig relation between real and imaginary parts of response function. In our case the optical conductivity of graphene must also follow such relation

$$\Im\{\sigma(\omega)\} = -\frac{2\omega}{\pi}\mathcal{P}\int_0^\infty \frac{\Re\{\sigma(\Omega)\}}{\Omega^2-\omega^2}d\Omega \tag{2.10a}$$

$$\Re\{\sigma(\omega)\} = \frac{2}{\pi}\mathcal{P}\int_0^\infty \frac{\Omega\Im\{\sigma(\Omega)\}}{\Omega^2-\omega^2}d\Omega \tag{2.10b}$$

Using Eqs. (2.3) and (2.4), one can show that Kramers-Krönig relation hold for Kubo formula. The proof is lengthy as such we do not provide the mathematical derivation here.

2.2 Surface Plasmon-Polariton Surface Waves on Graphene

As pointed out briefly in section 2.1.2, for low temperatures (e.g., $T = 3^\circ$ K), depending on the frequency of operation and value of chemical potential one can see negative or positive values for imaginary part of conductivity. But why is this important? The answer to this question lies within the solution to Maxwell's equation in the presence of graphene. So let us investigate how electromagnetic waves interact with graphene.

We present two approaches to this problem: one is the approach followed by several authors such as Hanson [41], Mikhailov & Ziegler [67], and Jablan et. al [47]. The second approach is our proposal [106], which is intuitive and is the basis for the method we use in our numerical simulations.

First approach: One can find the solutions to Maxwell's equations by matching the boundary conditions that include the surface conductivity of the graphene layer. We derive and present the dispersion relation for TM mode, while skip the steps for TE mode and just show the final result for $\omega - \beta$ relation (β being the wave-number).

Suppose we have a free-standing graphene lying in *x-y* plane (see Fig. 2.4). Consider a TM_y mode and assume that the electric field has the following form in two regions above

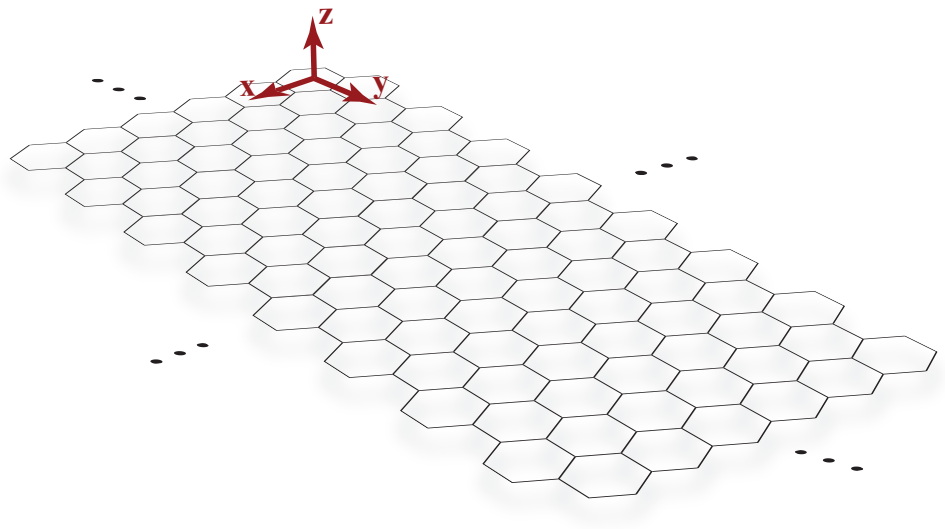

Figure 2.4: A free-standing graphene layer lying in *x*-*y* plane. The mode is propagating in *y*-direction and structure is uniform in *x*-direction.

and below the graphene layer (also assume $\partial/\partial x = 0$)

$$E_x = 0, \quad E_y = Ae^{i\beta y - pz}, \quad E_z = Be^{i\beta y - pz}, \quad \text{for } z > 0, \tag{2.11a}$$

$$E_x = 0, \quad E_y = Be^{i\beta y + pz}, \quad E_z = De^{i\beta y + pz}, \quad \text{for } z < 0, \tag{2.11b}$$

where β is the wave-number in *y*-direction and $p = \sqrt{\beta^2 - k_0^2}$ is the attenuation constant in *z*-direction (the geometry is uniform in *x*-direction). Substituting Eqs. (2.11a) and (2.11b) into Maxwell's equations and satisfying the boundary condition $\hat{\mathbf{z}} \times (\mathbf{H}^+ - \mathbf{H}^-) = \mathbf{J}^s = \sigma_g \mathbf{E}$, one arrives at following equation

$$\frac{2}{\sqrt{\beta^2 - k_0^2}} = -\frac{i\sigma_g}{\omega\epsilon_0}, \tag{2.12}$$

which can be recast to following dispersion relation for TM_y mode, reported by Refs. 41 and 47

$$\boxed{\beta = k_0 \sqrt{1 - \left(\frac{2}{\eta_0 \sigma_g}\right)^2}}, \tag{2.13}$$

in which k_0 is the wave number of the free space and η_0 is the intrinsic impedance of free space [41]. To have a slow surface wave on the proper Riemann sheet, we must have $\Re\{p\} > 0$. As such according to Eq. (2.12) this constraint requires $\Im\{\sigma_g\} > 0$ (i.e., when the intraband contribution dominates and the conductivity has the classical Drude form). If $\Im\{\sigma_g\} < 0$, which happens when interband contribution takes over, this mode is exponentially growing in the z-direction and is a leaky wave on the improper Riemann sheet [41]. In case conductivity is real-valued, the TM_y modes are on the improper sheet and no surface wave propagation is possible.

For TE_y mode, as shown in Refs. 67 and 41, following the same steps results in the dispersion relation

$$\boxed{\beta = k_0 \sqrt{1 - \left(\frac{\eta_0 \sigma_g}{2}\right)^2}} \tag{2.14}$$

In this case if $\Im\{\sigma_g\} < 0$, then the mode is slow surface wave on the proper sheet (when interband contribution dominates). For $\Im\{\sigma_g\} > 0$ the mode is exponentially growing in the vertical direction and is a leaky wave on the improper sheet. If conductivity is purely real (low temperature and small chemical potentials), since the condition $\Re\{p\} > 0$ is violated, all TE modes are on the improper sheet and fast leaky modes may contribute to radiation from graphene—for real values of conductivity, when $(\sigma_{g,r}\eta_0/2)^2 < 1$ we have fast propagating modes while for $(\sigma_{g,r}\eta_0/2)^2 > 1$, the mode is either growing or attenuating in direction of propagation [41, 47, 67].

Second approach: Now let us derive the same dispersion relations using our own approach [106]. In this approach, we momentarily assume that graphene has a very small thickness Δ, which later we will let $\Delta \to 0$. We then define a volume conductivity for this Δ-thick mono-layer

$$\sigma_{g,v} \equiv \frac{\sigma_g}{\Delta}. \tag{2.15}$$

Thus we can obtain volume current density in the graphene layer

$$\mathbf{J}_{\mathrm{v}} = \sigma_{\mathrm{g,v}}\mathbf{E}. \tag{2.16}$$

If we recast the Maxwell equation $\nabla \times \mathbf{H} = \mathbf{J}_{\mathrm{v}} - i\omega\epsilon_0\mathbf{E}$ as $\nabla \times \mathbf{H} = \left(\sigma_{\mathrm{g,v}} - i\omega\epsilon_0\right)\mathbf{E}$, we can obtain an equivalent complex permittivity for the Δ-thick graphene layer as

$$\epsilon_{\mathrm{g,eq}} \equiv \left(-\frac{\sigma_{\mathrm{g,i}}}{\omega\Delta} + \epsilon_0\right) + i\left(\frac{\sigma_{\mathrm{g,r}}}{\omega\Delta}\right). \tag{2.17}$$

For a one-atom-thick layer, bulk permittivity cannot be defined since permittivity only finds meaning when dealing with bulk materials. However, by temporarily assuming a small thickness Δ, we can associate an equivalent permittivity with the graphene layer. This assumption allows us to treat the graphene sheet as a thin layer of material with $\epsilon_{\mathrm{g,eq}}$. Once we derive the dispersion relation for this thin layer, we let Δ go to zero and recover the one-atom-thick layer geometry.

Using Eq. (2.17), we can identify real and imaginary parts of this equivalent permittivity as follows

$$\Re\{\epsilon_{\mathrm{g,eq}}\} = -\frac{\sigma_{\mathrm{g,i}}}{\omega\Delta} + \epsilon_0 \approx -\frac{\sigma_{\mathrm{g,i}}}{\omega\Delta}, \tag{2.18a}$$

$$\Im\{\epsilon_{\mathrm{g,eq}}\} = \frac{\sigma_{\mathrm{g,r}}}{\omega\Delta}. \tag{2.18b}$$

Equation (2.18a) suggests that the real part of equivalent permittivity of graphene layer can attain positive or negative values depending on the sign of the imaginary part of conductivity.

When $\sigma_{\mathrm{g,i}} > 0$, and in turn $\Re\{\epsilon_{\mathrm{g,eq}}\} < 0$, the free-standing graphene layer effectively behaves like a thin “metal” layer that can support a TM SPP surface wave, consistent with previous works [41, 45, 47, 67].

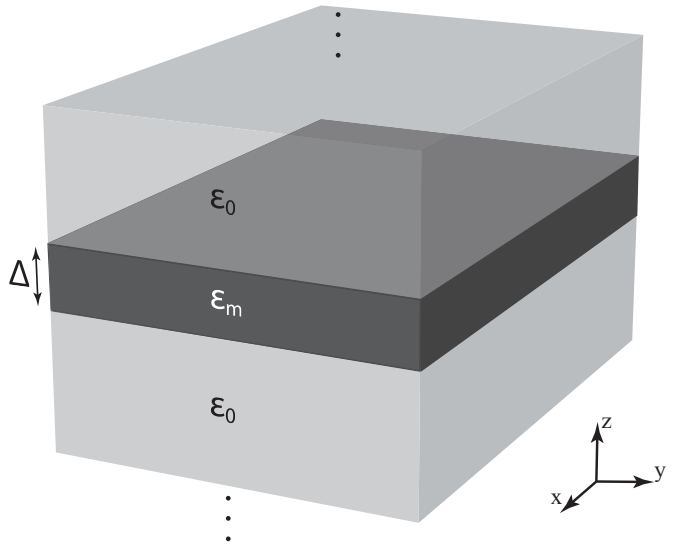

Figure 2.5: Free-standing slab of material with thickness Δ and complex permittivity ϵ_{m} surrounded by air.

Knowing TM and TE dispersion relation for a slab of material with complex permittivity that is surrounded by free space, we can retrieve dispersion relations (2.13) and (2.14). This problem has been solved previously [2] and we use the result here.

Consider the geometry depicted in Fig. 2.5. Denoting complex permittivity of a Δ-thick slab of material by ϵ_{m}, for $\Re\{\epsilon_{\mathrm{m}}\} < 0$ (e.g. for Ag or Au), the slab can support an odd TM electromagnetic guided mode with dispersion relation governing wave number β as

$$\coth\left(\sqrt{\beta^2-\omega^2\mu_0\epsilon_{\mathrm{m}}}\frac{\Delta}{2}\right) = -\frac{\epsilon_{\mathrm{m}}}{\epsilon_0}\frac{\sqrt{\beta^2-\omega^2\mu_0\epsilon_0}}{\sqrt{\beta^2-\omega^2\mu_0\epsilon_{\mathrm{m}}}}. \tag{2.19}$$

Using identity $\coth(ix) = -i\cot(x)$, we can rewrite Eq. (2.19) as

$$\cot\left(\sqrt{\omega^2\mu_0\epsilon_{\mathrm{m}}-\beta^2}\frac{\Delta}{2}\right) = -\frac{\epsilon_{\mathrm{m}}}{\epsilon_0}\frac{\sqrt{\beta^2-\omega^2\mu_0\epsilon_0}}{\sqrt{\omega^2\mu_0\epsilon_{\mathrm{m}}\beta^2}}. \tag{2.20}$$

By substituting ϵ_{m} with the equivalent permittivity $-\sigma_{\mathrm{g}}/i\omega\Delta + \epsilon_0$, we can recast Eq. (2.20) as

$$\frac{\frac{1}{2}\sqrt{i\omega\mu_0\sigma_{\mathrm{g}}\Delta + \left(k_0^2-\beta^2\right)\Delta^2}}{\tan\left(\frac{1}{2}\sqrt{i\omega\mu_0\sigma_{\mathrm{g}}\Delta + \left(k_0^2-\beta^2\right)\Delta^2}\right)} = \left(\frac{\Delta}{2} - \frac{i\sigma_{\mathrm{g}}}{2\omega\epsilon_0}\right)\sqrt{\beta^2-k_0^2}. \tag{2.21}$$

Taking limits of both sides when $\Delta \to 0$ (since $\lim_{\Delta\to 0}\{\text{RHS}\} = 1$ and $\lim_{\Delta\to 0}\frac{\Delta}{2} = 0$), we arrive at

$$1 = -\frac{i\sigma_g}{2\omega\epsilon_0}\sqrt{\beta^2 - k_0^2}, \tag{2.22}$$

which is equivalent to Eq. (2.12). So our approach yields the dispersion relation as offered by others. This approach is in particular very useful in conducting numerical simulations. The recipe for our numerical simulations can be found in Appendix B.

Now suppose we have a slab of material for which $\Re\{\epsilon_m\} > 0$ (again same geometry as in Fig. 2.5). It has been shown [7] that such slab can support odd TE electromagnetic guided mode with wave number β expressed as

$$\sqrt{\omega^2\mu_0\epsilon_m - \beta^2}\tan\left(\sqrt{\omega^2\mu_0\epsilon_m - \beta^2}\frac{\Delta}{2}\right) = \sqrt{\beta^2 - k_0^2}. \tag{2.23}$$

Again by substituting ϵ_m with the equivalent permittivity $-\sigma_g/i\omega\Delta + \epsilon_0$, we can rewrite Eq. (2.23) as

$$\sqrt{\frac{i\omega\mu_0\sigma_g}{\Delta} + k_0^2 - \beta^2}\tan\left(\frac{1}{2}\sqrt{i\omega\mu_0\sigma_g\Delta + \left(k_0^2 - \beta^2\right)\Delta^2}\right) = \sqrt{\beta^2 - k_0^2}. \tag{2.24}$$

When $\Delta \to 0$, the Eq. (2.24) simplifies to

$$\frac{1}{2}\sqrt{\frac{i\omega\mu_0\sigma_g}{\Delta}}\sqrt{i\omega\mu_0\sigma_g\Delta} = \sqrt{\beta^2 - k_0^2}, \tag{2.25}$$

leading to

$$\frac{i\omega\mu_0\sigma_g}{2} = \sqrt{\beta^2 - k_0^2}, \tag{2.26}$$

which can be recast to dispersion relation expressed in in Eq. (2.14).

So to summarize our discussion, we showed that when $\sigma_{g,i} > 0$, a graphene layer supports a TM electromagnetic SPP surface wave and when $\sigma_{g,i} < 0$, TM SPP guided surface waves are no longer supported by the graphene and instead, a weakly guided TE electromagnetic SSP surface wave is present. Since the wavenumbers for the TE guided mode are very close to that of free space, those modes are not confined and may not be of

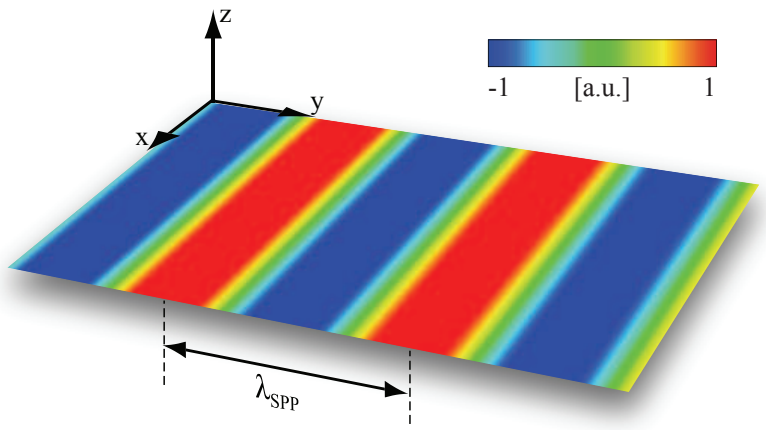

Figure 2.6: Snapshot in time of the transverse component of the electric field of TM surface plasmon-polariton surface wave along a graphene layer free standing in air (f = 30 THz, T = 3° K, Γ = 0.43 meV and μ_c = 150 meV across whole layer). The graphene layer dimensions are L = 350 nm, w = 235 nm. This chemical potential can be achieved, for example, by a bias voltage of 22.84 V across a 300-nm SiO_2 spacer between the graphene and the Si substrate (but Si substrate and SiO_2 spacer are not present here in our simulation). The SPP wavelength along the graphene, λ_{SPP} is much smaller than free-space wavelength λ_0, i.e., $\lambda_{SPP} = 0.0144\lambda_0$ [107].

interest. However due to their high confinement, TM SPP surface waves are favorable for design of compact electromagnetic systems. Figure 2.6 displays the numerical simulation of a TM SPP mode at 30 THz guided by a uniformly biased graphene layer.

It is worth mentioning that recently the existence of surface plasmon polaritons on graphene has been verified experimentally by several research groups [14, 30, 31]. Of particular interest are experiments reported in Refs. 14 and 31, which show tunability of surface plasmon by means of gate voltage. Both experiments are carried out by use of near-field scattering microscopy with infrared excitation light and verify that the surface plasmons on graphene are highly confined as theory predicts.

In section 2.2.1, we make a comparison between graphene and silver (as a representative of noble metals), to see which one might be a “better” platform for carrying SPP surface waves.

2.2.1 A comparison between graphene and silver as host for surface plasmon polaritons

As in graphene, surface plasmon-polaritons electromagnetic waves also exist along metal-dielectric interfaces due to collective oscillations of surface charges (see Fig. 2.7). These waves decay exponentially in the transverse direction. It is well known that SPP modes at a metal-dielectric interface follow the dispersion relation [63]

$$\beta_{\mathrm{SPP}} = k_0 \sqrt{\frac{\epsilon_r \epsilon_m(\omega)}{\epsilon_r + \epsilon_m(\omega)}}, \tag{2.27}$$

where ϵ_r is the relative permittivity of the dielectric material and $\epsilon_m(\omega)$ is the complex permittivity of the noble metal, e.g. silver. For a wide range of frequency permittivity of noble metals can be described using *Drude model*, in which a gas of free electrons moves against fixed positive ion cores [63]

$$\epsilon_m(\omega) = 1 - \frac{\omega_p^2}{\omega\,(\omega + i\gamma)}, \tag{2.28}$$

in which ω_p is the plasma frequency and γ is the collision frequency representing loss.

A necessary condition for SPP modes to form at the interface is $\epsilon_m(\omega) < -\epsilon_r$. To have negative $\epsilon_m(\omega)$, the operating frequency should be below plasma frequency ω_p. The noble metals, e.g., silver and gold, have long been popular materials for constructing optical metamaterials [12]. However material losses have always been the bottleneck of these metals since these losses degrade the quality of surface plasmon resonances and put constraints on design of metamaterial structures constructed from these materials—i.e., due to loss the propagation length of SPP waves is limited.

Our goal here is to provide a comparison between graphene and silver to investigate characteristics of SPP surface waves for these two mediums. To this end, we consider real and imaginary parts of wave number and the Figure-of-Merit (FoM) of SPP surface waves, defined as $\frac{\Re\{\beta\}}{\Im\{\beta\}}$ (this quantity is a measure of how many wavelengths SPP survives before

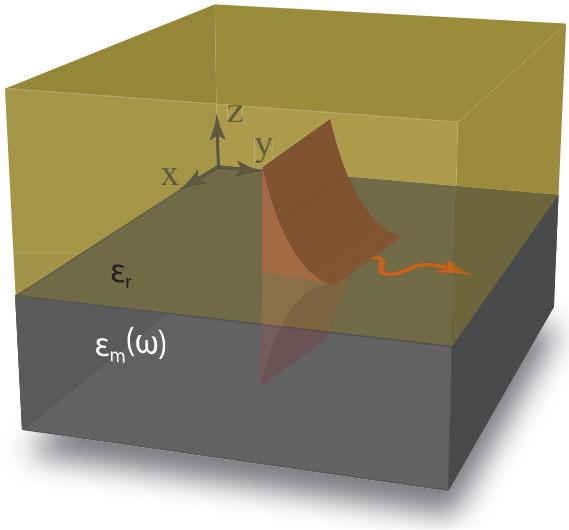

Figure 2.7: Surface plasmon-polartions along metal-dielectric interface due to collective oscillations of surface charges.

it loses most of its energy). As an example for a graphene layer free-standing in air, at $T = 3^\circ$ K and for $\Gamma = 0.43$ meV and $\mu_c = 150$ meV at frequency 30 THz, based on Kubo formula and the dispersion relation expressed in Eq. (2.13), we obtain $\Re\{\beta\} = 69.34k_0$ and $\Im\{\beta\} = 0.71k_0$, resulting in FoM of approximately 97.7. The corresponding numbers for the SPP at the air-silver interface, using Eq. (2.27), and based on material parameters $\omega_p = 2\pi \times 2.175 \times 10^{15} \frac{\text{rad}}{\text{s}}$ and $\gamma = 2\pi \times 4.35 \times 10^{12} \frac{\text{rad}}{\text{s}}$ for silver in the mid-IR wavelengths [79], are approximately $\Re\{\beta\} = k_0$ and $\Im\{\beta\} = 10^{-4}k_0$, resulting in a loosely confined SPP. Here the FoM for silver in the mid-IR is artificially high, however we need to take extra care in interpreting this high value. This high value occurs since $\Im\{\beta\}$ is very small and $\Re\{\beta\}$ takes moderate values (almost equal to k_0), suggesting that the mode is very weakly guided.

Graphene has two major advantages over the noble metals as platform for metamaterial structures and transformation optical devices:

(i) As discussed above, with regards to the SPP characteristics, at least for mid infrared (IR) wavelengths, graphene can be a better host for surface plasmon resonances

compared with silver or gold. The two quality measures for SPP—the propagation length, defined as $1/\Im\{\beta\}$ and the mode lateral extent, proportional to approximately $1/\Re\{\beta\}$—are more favorable for graphene than for silver; as can be seen in Fig. 2.8, **A**, the real part of wave number β for TM SPP waves along graphene is much larger than that of free space. As a result, such an SPP surface wave is tightly confined to the graphene layer with guided wavelength λ_{SPP} much smaller than free space wavelength λ_0 ($\lambda_{\text{SPP}} \ll \lambda_0$), whereas its imaginary part of wavenumber is relatively small.

(ii) Probably the most important advantage of graphene over noble metals is the degree of freedom that we have in dynamically tuning the conductivity of graphene [107]. We can tune the conductivity locally and inhomogeneously by means of chemical doping or gate voltage (i.e., bias electric field (E_{bias}) in real time). By applying different values of E_{bias} at different locations across the graphene layer, one can create desired conductivity patterns across the layer. By proper design of such spatial patterns, we can tame IR SPP wave signals across the graphene, and manipulate and route them at our will. In chapter 3 we present numerous scenarios based on metamaterial functions and concepts following form this degree of freedom—possibility of tuning the graphene conductivity.

One possibility to achieve desired conductivity patterns across graphene is to use gate voltage and split gates locally to alter the conductivity at different locations across graphene. In addition to this technique, we have proposed two other methods in Ref. 106.

First proposed approach is to design and fabricate a nonuniform height profile for the ground plane underneath the dielectric spacer holding the graphene sheet (The ground plane is commonly made up of highly-doped Silicon). Applying a fixed voltage between the sheet of graphene and ground plane results in a nonuniform dc electric field distribution across the graphene layer (see Fig. 2.9).

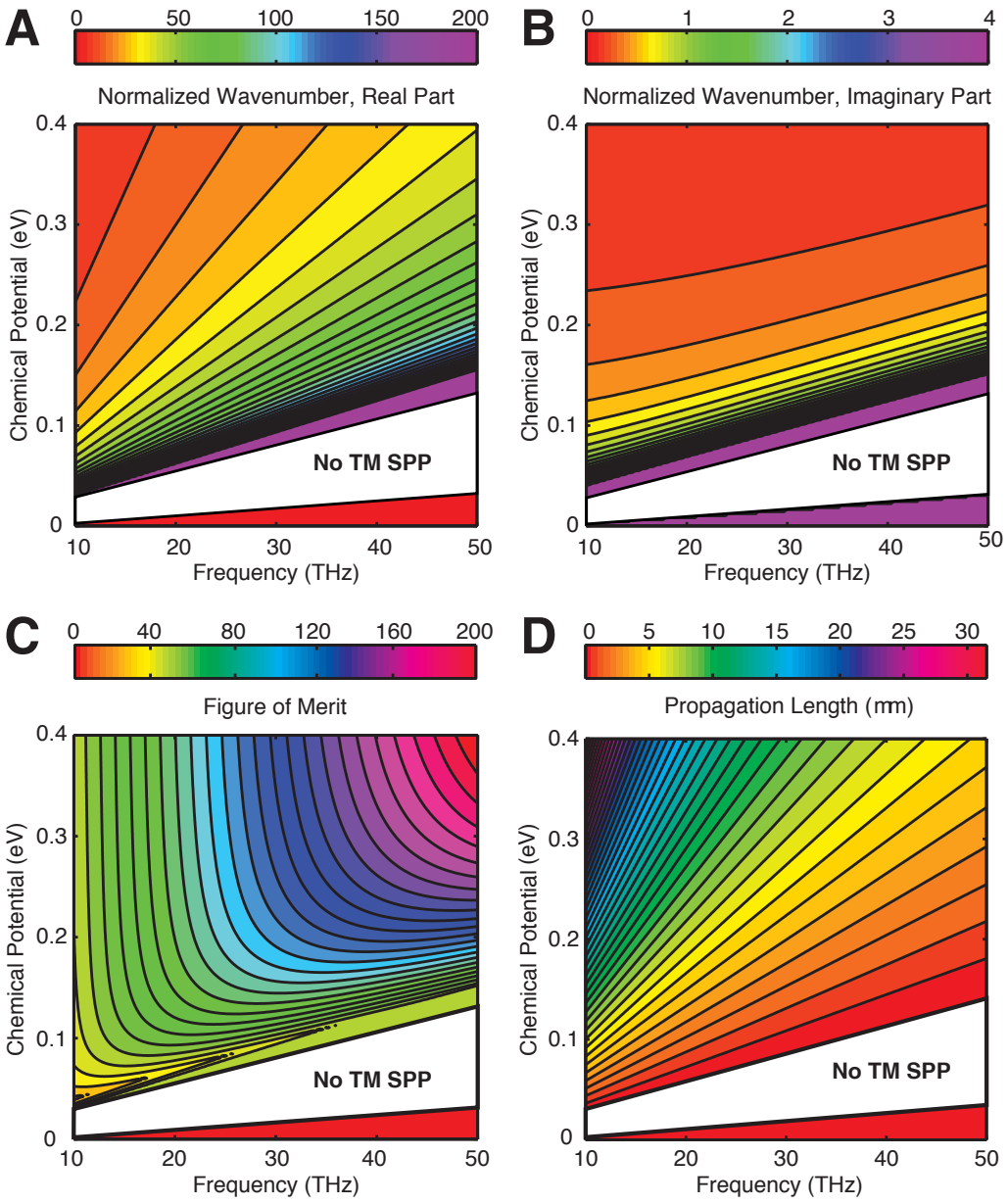

Figure 2.8: Characteristics of TM SPP surface waves along graphene. Panel **A** and **B** display the real and Imaginary parts of the normalized wave number (β/k_0) for TM SPP surface waves supported by the single sheet of graphene free-standing in air, as a function of chemical potential μ_c and frequency f, according to Kubo formula ($T = 3°$ K, $\Gamma = 0.43$ meV). Panel **C** illustrates Figure-of-Merit (FOM) for the SPP mode as a function of μ_c and frequency f. Panel **D** shows the propagation length of the SPP mode. Reprinted from Ref. 107 (by permission of the AAAS). [http://www.sciencemag.org/content/suppl/2011/06/08/332.6035.1291.DC1/Vakil-SOM.pdf].

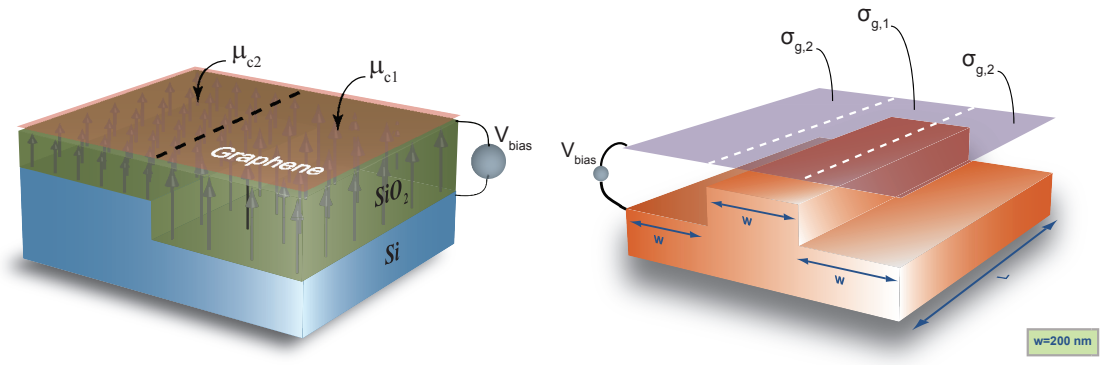

Figure 2.9: Different ideas for creating nonuniform conductivity using uneven ground plane are illustrated on left and right panel (schematic). Uneven ground plane underneath the graphene layer to construct inhomogeneous conductivity pattern across the layer. By biasing the graphene with a single static voltage, the static electric field is distributed according to the height of the spacer between the graphene and the uneven ground plane, leading to the unequal static electric field. This results in unequal carrier densities and chemical potentials $\mu_{c,1}$ and $\mu_{c,2}$ on the surface of the single graphene and thus different conductivity distributions across the graphene. Here in this schematic and in our numerical simulations, for the sake of simplicity in the simulation and to keep the concepts easily and intuitively understandable, we have assumed the "sharp" inhomogeneity in conductivity distributions of the two neighboring sections of a single flake of graphene. However, since the static biasing electric field in the space underneath of graphene is expected to be gradually varied in going from one region to another, the chemical potential and the conductivity distribution will have a smooth transition. But we emphasize that our ideas of transformation optics on graphene will still remain valid and applicable even when the transition region around the conductivity mismatch is smooth. Reproduced from Ref. 107 (by permission of the AAAS). [http://www.sciencemag.org/content/suppl/2011/06/08/332.6035.1291.DC1/Vakil-SOM.pdf].

Since the separation between the graphene and the ground plane varies depending on the location, the dc electric field, due to the bias voltage between the graphene and ground plane, is nonuniform. Therefore the distribution of local carrier densities—and hence the spatial distribution of chemical potential—will be nonuniform, resulting in different conductivity values in different segments; the nonuniform profile of the ground plane Silicon might be realized through wet etching of the surface of the Silicon [89] or by the standard techniques of nano-lithography, e.g., e-beam lithography [118]. The proposed idea is experimentally feasible and within the realm of current fabrication technology.

Second proposed approach is based on creating inhomogeneous SiO_2 spacer (see Fig. 2.10).

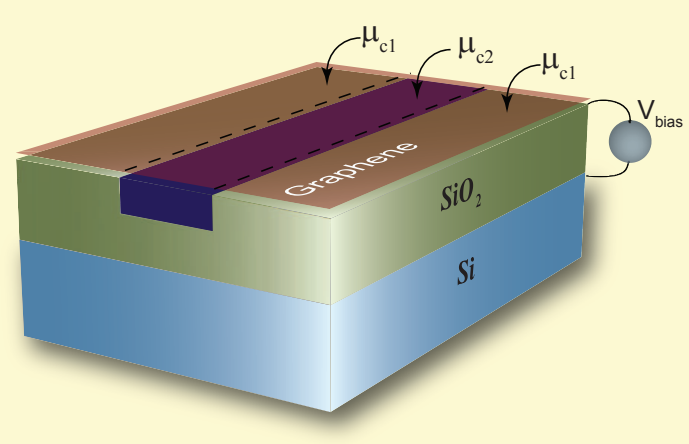

Figure 2.10: (Schematic) Second idea to create inhomogeneous conductivity patterns across graphene. Here several dielectric spacers with unequal permittivity functions can be used underneath of the graphene to create unequal bias electric field distributions, resulting in inhomogeneous carrier densities and conductivity patterns across layer of graphene. Reprinted from Ref. 107 (by permission of the AAAS). [http://www.sciencemag.org/content/suppl/2011/06/08/332.6035.1291.DC1/Vakil-SOM.pdf].

Again applying a fixed dc voltage between the graphene and the ground plane results in a static electric field in this narrow region that is different from the static field elsewhere in the spacer. This will alter the carrier density distribution and the segment of graphene on top of this dielectric strip will have a different conductivity from other segments. If the width of this strip on top of the spacer is small (but not too small to become comparable with the nanostructured dimensions within a graphene, in which case the quantum nature of the structure should be considered [104, 105]), the width of the graphene with the different conductivity can be as small. It is worth mentioning that the dimensions we have chosen for our examples are larger than the nanostructured dimensions within graphene, so the Kubo conductivity model is still valid. Also, in our numerical simulations, for simplicity and to keep the concepts easy to absorb, we have assumed a “sharp” inhomogeneity in conductivity distributions of the two neighboring sections of a single flake of graphene. Our ideas of transformation optics will still be valid and applicable even when the inhomogeneity

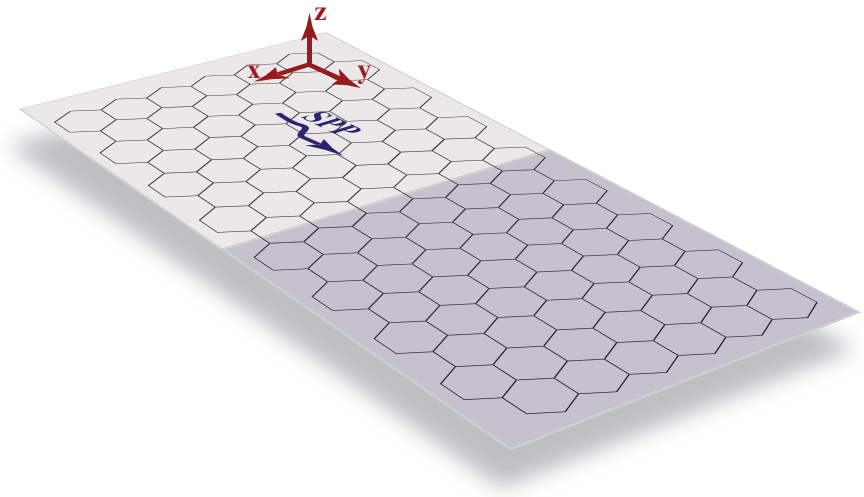

Figure 2.11: Fresnel reflection for an SPP surface wave hitting a boundary line due to conductivity mismatch in the plane of graphene. The darker region has different conductivity from the region highlighted with light gray. We investigate the reflection of the SPP surface wave that is launched toward the boundary created as result of conductivity mismatch.

between the two sections is not very sharp [107].

Now that we qualified graphene as a better platform for mid-IR metamaterial structures and transformation optics devices, let us address the essential problems that form the foundations for engineering such structures and devices.

2.2.2 Foundations for design of metamaterial structures and transformation optics devices

As pointed out earlier our goal is to put forth graphene as a platform for metamaterials and transformation optics. However to be able to design metamaterials and transformation optical devices, it is most important to tackle four essential problems

(i) *Propagation of SPP surface waves along graphene:* This problem is basically what we addressed above. We quantified the propagation parameters of a TM SPP surface wave propagating along graphene, based on the surface conductivity model intro-

duced in section 2.1. We characterized the modes based on the sign of imaginary part of conductivity and expressed dispersion relations for each mode in Eqs. (2.13) and (2.14).

(ii) *Green's functions for an electric current source in the presence of graphene layer:* It is important to study the interaction of an electromagnetic dipolar source (e.g., atoms and molecules) with graphene. The fields can be derived in terms of dyadic Green's functions represented using Sommerfeld integrals. This problem is a variant of famous classic Sommerfeld half-plane and has been addressed in the literature by several authors [41, 42, 72]. In the following sections we briefly discuss this problem, review some of the relevant works and present the dyadic Green's functions for TM SPP surface waves.

(iii) *Fresnel reflection:* Another essential problem to address is the reflection of surface plasmon-polariton (SPP) surface waves from boundaries in the plane of graphene. In other words, we would like to ask the following question: if somehow a conductivity mismatch is created within the graphene layer, how would an SPP surface wave reflect from that boundary (see Fig. 2.11, in which two regions with differing conductivities are shown in light and dark colors. The SPP surface wave is propagating in y-direction toward the boundary of these two regions).

Due to 2-dimensional (2D) structure of graphene, derivation of an exact solution to this problem proves to be complicated. The problem has been addressed in the context of diffraction by surface impedance discontinuities and impedance half-planes [90]. However, in the following, we present a much simpler approximate semi-analytical approach to quantify the reflection of SPP surface waves from discontinuities in plane of graphene.

(iv) *Polarizability of a small patch that has different conductivity from the surrounding:* We are interested in the problem of scattering of SPP surface waves by a small patch (for example a small disk) with a different conductivity from its surrounding host. Once this problem is solved, in first-order approximation, we may regard any small patch of graphene as a dipole moment with a known polarizability (which is related to its geometrical and optical properties). Knowing the polarizability of the patch, since we have also developed the Green's functions for a current source in the proximity of graphene, we are then able to obtain the fields scattered from the patch in the plane of graphene layer. These patches will be building blocks of metamaterial structures constructed based on graphene.

The problem of SPP propagation has already been addressed so we devote next sections to other three problems that form foundations for design and engineering metamaterials and transformation optical devices.

2.2.3 Dydic Green's functions for graphene

Efficient excitation of surface plasmon-polaritons on graphene is the precondition to any optical metamaterial functionality we may envision based on this layer of carbon atoms. One efficient way proposed to excite the SPP modes is to use quantum dots or molecules or any other variant of quantum emitters [43, 54]. Describing such quantum emitters as dipole moments, we can describe their bound modes due to presence of a graphene layer using Green's tensor. This problem is variant of classic Sommerfeld half-plane problem with modified boundary conditions. Several researchers have addressed this problem [41, 42, 72]. Here we follow similar steps as Sommerfeld devised [46, 98] for the case of horizontal dipole. The derivation for the vertical dipole is similar and we do not show the

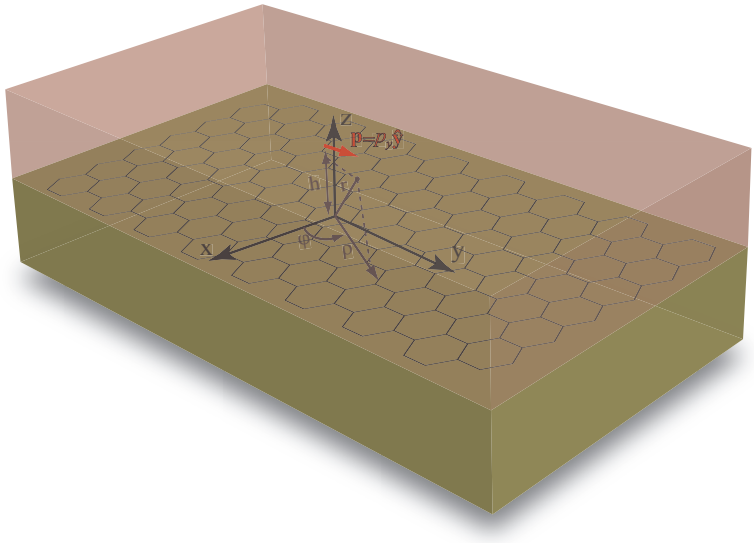

Figure 2.12: Horizontal electric dipole along y axis at distance h above a graphene layer. The graphene layer is placed at the interface of two dielectric media, characterized by permittivities ϵ_1 and ϵ_2, which in general can be lossy and dispersive.

steps, however we provide the results for an arbitrarily oriented dipole in terms of dyadic Green's functions [72].

Consider a horizontal electric dipole $\mathbf{p} = p_y\hat{\mathbf{y}}$ (depicted in Fig. 2.12) in medium 1 (with permittivity ϵ_1 and permeability μ_0). The graphene layer lies at the interface of the medium 1 and medium 2 (for $z < 0$ we have permittivity ϵ_2 and permeability μ_0).

The fields can be described by Hertz vector potential $\mathbf{\Pi}$, which satisfies Helmholtz equation. At the first glance, it may appear reasonable to assume Hertz vector, $\mathbf{\Pi}$, has only y-component for a dipole aligned in y-direction. However to satisfy the boundary conditions at $z = 0$, we need to have two components for Hertz vector. This can be resolved by assuming Hertz vector also has a component along z-direction

$$\mathbf{\Pi} = \left(0, \Pi_y, \Pi_z\right). \tag{2.29}$$

The electric and magnetic fields are related to Hertz vector as following (for n = 1, 2)

$$\mathbf{E}^{(\mathrm{n})}(\mathbf{r}) = \left(k_{\mathrm{n}}^2 + \nabla\nabla\right)\mathbf{\Pi}^{(\mathrm{n})}(\mathbf{r}), \tag{2.30a}$$

$$\mathbf{H}^{(\mathrm{n})}(\mathbf{r}) = -i\omega\epsilon_{\mathrm{n}}\nabla\times\mathbf{\Pi}^{(\mathrm{n})}(\mathbf{r}), \tag{2.30b}$$

in which $k_{\mathrm{n}} = \omega\sqrt{\mu_0\epsilon_{\mathrm{n}}}$. Here we conduct the derivation for electric fields. Magnetic fields can be obtained accordingly using Maxwell's equations. In our case since $\Pi_x = 0$, Eq. (2.30a) can be simplified as (for n = 1, 2)

$$E_x^{(\mathrm{n})} = \frac{\partial}{\partial x}\nabla\cdot\mathbf{\Pi}^{(\mathrm{n})}, \tag{2.31a}$$

$$E_y^{(\mathrm{n})} = k_{\mathrm{n}}^2\Pi_y^{(\mathrm{n})} + \frac{\partial}{\partial y}\nabla\cdot\mathbf{\Pi}^{(\mathrm{n})}, \tag{2.31b}$$

$$E_z^{(\mathrm{n})} = k_{\mathrm{n}}^2\Pi_z^{(\mathrm{n})} + \frac{\partial}{\partial z}\nabla\cdot\mathbf{\Pi}^{(\mathrm{n})}. \tag{2.31c}$$

The Hertz potential vector can be written as

$$\mathbf{\Pi}^{(1)} = \mathbf{\Pi}_{\mathrm{p}} + \mathbf{\Pi}_{\mathrm{s}}^{(1)}, \tag{2.32}$$

for the first medium and

$$\mathbf{\Pi}^{(2)} = \mathbf{\Pi}_{\mathrm{s}}^{(2)}, \tag{2.33}$$

for the second medium, where $\mathbf{\Pi}_{\mathrm{p}}$ is the primary potential due to the dipole and $\mathbf{\Pi}_{\mathrm{s}}^{(1)}$ and $\mathbf{\Pi}_{\mathrm{s}}^{(2)}$ are the secondary potentials due to the presence of the graphene layer.

For $z > 0$, Π_y has to satisfy

$$\left(\nabla^2 + k_1^2\right)\Pi_y^{(1)} = -\frac{p_y}{\epsilon_1}\delta\left(r - r'\right), \tag{2.34}$$

and for $z < 0$

$$\left(\nabla^2 + k_2^2\right)\Pi_y^{(2)} = 0, \tag{2.35}$$

Suppressing the multiplicative term $\frac{p_y}{\epsilon_1}$ and assuming $p_{\{1,2\}} = \sqrt{k_\rho^2 - k_{\{1,2\}}^2}$, the primary field $\Pi_{\mathrm{p},y}$ is then given by

$$\Pi_{\mathrm{p},y} = \frac{1}{8\pi}\int_{-\infty}^{\infty} H_0^{(1)}(k_\rho\rho)e^{-p_1|z-h|}\frac{k_\rho dk_\rho}{p_1} = \frac{e^{ik_1 r}}{4\pi r}, \tag{2.36}$$

where $H_0^{(1)}(.)$ denotes the first kind Hankel function of zeroth order, and $r = \sqrt{\rho^2 + z^2}$. The secondary fields can be written as following

$$\Pi_{\mathrm{s},y}^{(1)} = \frac{1}{8\pi}\int_{-\infty}^{\infty} R(k_\rho)H_0^{(1)}(k_\rho\rho)e^{-p_1|z+h|}\frac{k_\rho dk_\rho}{p_1}, \tag{2.37}$$

$$\Pi_{\mathrm{s},y}^{(2)} = \frac{1}{8\pi}\int_{-\infty}^{\infty} T(k_\rho)H_0^{(1)}(k_\rho\rho)e^{p_2 z - p_1 h}\frac{k_\rho dk_\rho}{p_1}, \tag{2.38}$$

where $R(k_\rho)$ and $T(k_\rho)$ are yet to be determined by satisfying the boundary conditions at $z = 0$. Following an approach similar to Sommerfeld [98], using continuity of electric field and boundary condition for tangential components of magnetic field (which include the surface conductivity of graphene) at $z = 0$, we arrive at following relations

$$\epsilon_1\Pi_y^{(1)} = \epsilon_2\Pi_y^{(2)}, \tag{2.39a}$$

$$\frac{\partial\Pi_y^{(1)}}{\partial y} + \frac{\partial\Pi_z^{(1)}}{\partial z} = \frac{\partial\Pi_y^{(2)}}{\partial y} + \frac{\partial\Pi_z^{(2)}}{\partial z}, \tag{2.39b}$$

$$\epsilon_1\Pi_z^{(1)} - \epsilon_2\Pi_z^{(2)} = -\frac{\sigma_{\mathrm{g}}}{i\omega}\nabla\cdot\mathbf{\Pi}^{(1)} = -\frac{\sigma_{\mathrm{g}}}{i\omega}\nabla\cdot\mathbf{\Pi}^{(2)}, \tag{2.39c}$$

$$\epsilon_2\frac{\partial\Pi_y^{(2)}}{\partial z} - \epsilon_1\frac{\partial\Pi_y^{(1)}}{\partial z} = -\frac{\sigma_{\mathrm{g}}}{i\omega}k_1^2\Pi_y^{(1)}, \tag{2.39d}$$

which are respectively obtained from continuity of E_y and E_x, and boundary conditions for H_y and H_x. Denoting ϵ_2/ϵ_1 by n, Eqs. (2.39a) and (2.39d) yield

$$1 + R(k_\rho) = nT(k_\rho), \tag{2.40a}$$

$$np_2T(k_\rho) - p_1\left(1 - R(k_\rho)\right) = i\sigma_g\omega\mu_0\left(1 + R(k_\rho)\right). \tag{2.40b}$$

Form Eqs. (2.40a) and (2.40b), one can obtain

$$R(k_\rho) = \frac{p_1 - p_2 + i\omega\sigma_g\mu_0}{p_1 + p_2 - i\omega\sigma_g\mu_0}, \tag{2.41}$$

$$T(k_\rho) = \frac{2p_1}{n\left(p_1 + p_2 - i\omega\sigma_g\mu_0\right)}. \tag{2.42}$$

Equation (2.39b) can be recast as following

$$\frac{\partial}{\partial y}\left(\Pi_y^{(2)} - \Pi_y^{(1)}\right) = \frac{\partial}{\partial z}\left(\Pi_z^{(1)} - \Pi_z^{(2)}\right) \tag{2.43}$$

But $\frac{\partial\Pi_y}{\partial y}$ can be written as $\sin\phi\frac{\partial\Pi_y}{\partial\rho}$, where $\rho = \sqrt{x^2 + y^2}$ and $\phi = \cos^{-1}(\hat{\rho}\cdot\hat{\mathbf{x}})$. As such and from Eq. (2.43) it follows that Π_z must also have a $\sin\phi$ factor, implying that Π_z must be constructed from higher order Hankel functions ($n = 1$):

$$\Pi_z^{(1)} = \sin\phi\frac{1}{8\pi}\int_{-\infty}^{\infty} H_1^{(1)}(k_\rho\rho)e^{-p_1(z+h)}\Phi_1(k_\rho)dk_\rho, \tag{2.44}$$

$$\Pi_z^{(2)} = \sin\phi\frac{1}{8\pi}\int_{-\infty}^{\infty} H_1^{(1)}(k_\rho\rho)e^{p_2z-p_1h}\Phi_2(k_\rho)dk_\rho, \tag{2.45}$$

Substituting Eqs. (2.36), (2.37), (2.38), (2.44) and (2.45) in Eq. (2.43), and considering Eqs. (2.41) and (2.42), we obtain a system of linear equations which can be written in following matrix form

$$\begin{pmatrix} p_1 & p_2 \\ -\frac{i\omega\epsilon_1}{\sigma_g} & p_2 - \frac{i\omega\epsilon_2}{\sigma_g} \end{pmatrix}\begin{pmatrix} \Phi_1(k_\rho) \\ \Phi_2(k_\rho) \end{pmatrix} = \frac{2k_\rho^2}{p_1 + p_2 - i\omega\sigma_g\mu_0}\begin{pmatrix} \frac{1}{n} - 1 \\ \frac{1}{n} \end{pmatrix}. \tag{2.46}$$

Solving for $\Phi_1(k_\rho)$ and $\Phi_2(k_\rho)$ yields

$$\Phi_1(k_\rho) = -\frac{2k_\rho^2\left[\sigma_g p_2 - i\omega\epsilon_2\left(1 - \frac{1}{n}\right)\right]}{\left[\sigma_g p_1 p_2 - i\omega\left(p_2\epsilon_1 + p_1\epsilon_2\right)\right]\left(p_1 + p_2 - i\omega\sigma_g\mu_0\right)}, \tag{2.47a}$$

$$\Phi_2(k_\rho) = -\frac{2k_\rho^2\left[-\frac{1}{n}\sigma_g p_1 - i\omega\epsilon_1\left(1-\frac{1}{n}\right)\right]}{\left[\sigma_g p_1 p_2 - i\omega\left(p_2\epsilon_1 + p_1\epsilon_2\right)\right]\left(p_1 + p_2 - i\omega\sigma_g\mu_0\right)} \tag{2.47b}$$

Let us simplify the problem by assuming that graphene is free standing in air (the case we studied in previous sections) and we are looking at the case where the horizontal dipole is rested on the graphene. This implies that $p_1 = p_2 = p = \sqrt{k_\rho^2 - k_0^2}$, $\epsilon_1 = \epsilon_2 = \epsilon_0$ and in turn $n = \frac{\epsilon_2}{\epsilon_1} = 1$, and $h = 0$. So we can simplify $R(k_\rho)$ and $\Phi_1(k_\rho)$ as following

$$R(k_\rho) = \frac{i\omega\sigma_g\mu_0}{2p - i\omega\sigma_g\mu_0}, \tag{2.48}$$

$$\begin{aligned}\Phi_1(k_\rho) &= -\frac{2\sigma_g k_\rho^2}{\left(\sigma_g p - 2i\omega\epsilon_0\right)\left(2p - i\omega\sigma_g\mu_0\right)} \\ &= -\frac{\sigma_g p}{\sigma_g p - 2i\omega\epsilon_0} - \frac{i\omega\sigma_g\mu_0}{2p - i\omega\sigma_g\mu_0} \\ &= -\frac{\sigma_g p}{\sigma_g p - 2i\omega\epsilon_0} - R(k_\rho),\end{aligned} \tag{2.49}$$

The total fields can be calculated using numerical evaluation of integrals on the original Sommerfeld integral path (SIP) on the real axis, however the surface waves field can be evaluated analytically from the residue contribution of Sommerfeld integral; the pole singularities of $R(k_\rho)$ and $\Phi_1(k_\rho)$ (Sommerfeld poles) represent discrete surface modes. The pole of $R(k_\rho)$ ($2p - i\omega\sigma_g\mu_0 = 0$) yields the TE dispersion relation consistent with Eq. (2.14) and the second pole singularity of $\Phi_1(k_\rho)$ ($\sigma_g p - 2i\omega\epsilon_0 = 0$) gives TM dispersion relation in agreement with Eq. (2.13). These calculation are done by deforming the contour integral and closing it in the upper half-plane of complex k_ρ. The poles then will be enclosed in the contour and according to Cauchy's principal value theorem we can compute the contribution due to the poles. As we are interested in TM modes due to the horizontal dipole, we calculate the contribution due to the associated pole. Also Π_y corresponds to TE surface mode and does not contribute to the TM surface waves, but interestingly gives rise to Π_z,

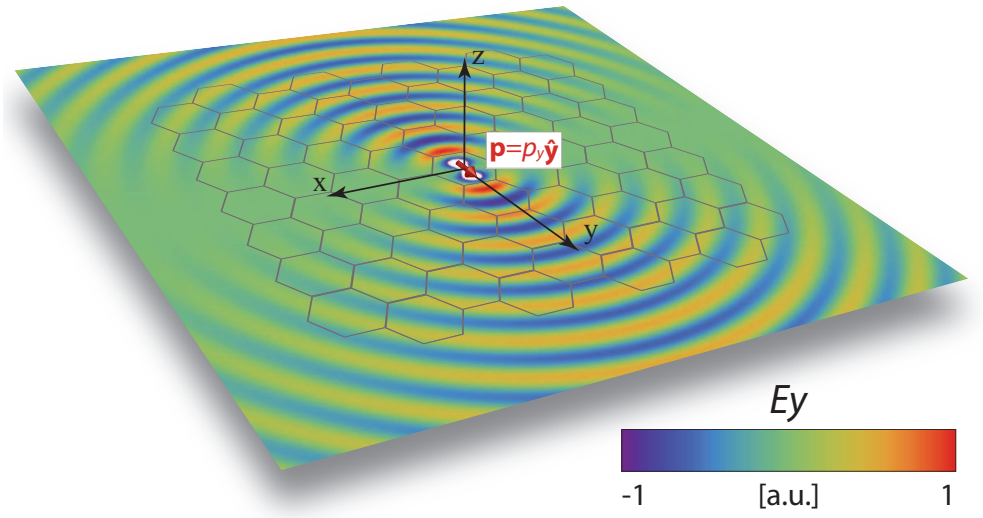

Figure 2.13: Distribution of E_y on the plane of a free-standing graphene due to a horizontal electric dipole on the graphene layer and aligned with y-axis.

which propagates mostly in the direction parallel to the dipole ($\phi = 90°$). As such in our calculations we find the residue of the integral due to Π_z. Conducting the calculations and assuming $\frac{p_y}{\epsilon_0} = 1$ (the term we dropped earlier) we obtain

$$E_x^{\mathrm{TM,SPP}}(\rho, z) = \frac{i \sin\phi \cos\phi}{8} p^3 \left[H_0^{(1)}(k_\rho \rho) - H_2^{(1)}(k_\rho \rho)\right] e^{-p|z|}, \tag{2.50a}$$

$$E_y^{\mathrm{TM,SPP}}(\rho, z) = \frac{i \sin^2\phi}{8} p^3 \left[H_0^{(1)}(k_\rho \rho) - H_2^{(1)}(k_\rho \rho)\right] e^{-p|z|}, \tag{2.50b}$$

$$E_z^{\mathrm{TM,SPP}}(\rho, z) = \frac{i \sin\phi}{8} p^2 k_\rho H_1^{(1)}(k_\rho \rho) e^{-p|z|}, \tag{2.50c}$$

The snapshot in time of distribution of real part of different components of electric field is presented in Fig. 2.13 (E_y) and Fig. 2.14, **A** and **B** (E_x and E_z). We can observe that the mode is maximum in the direction of the dipole. The presence of graphene has substantially changed the radiation pattern of the dipole. Similar derivation can be carried through to obtain the TM SPP fields due to a vertical electric dipole (VED). Nikitn et. al [72] have

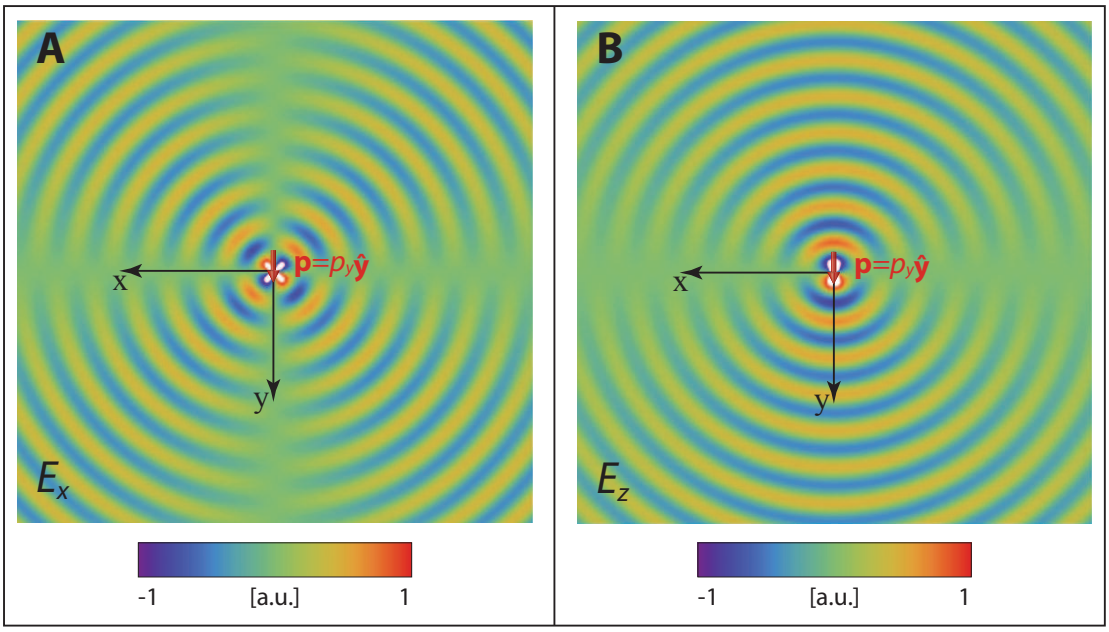

Figure 2.14: The snapshot in time of distribution of E_x and E_z on the plane of graphene due to a horizontal electric dipole on the graphene layer and aligned with y-axis.

derived the closed form Green's tensor for the TM SPP waves following methodology developed in Ref. 77. They show that the Green tensor has the following form

$$\overleftrightarrow{\mathbf{G}}(\rho,z) \propto e^{-p|z|}\begin{pmatrix} H_{-}^{(1)}(k_\rho\rho) & 0 & -\frac{i\sigma_g k_\rho}{\omega\epsilon_0}H_1^{(1)}(k_\rho\rho) \\ 0 & H_{+}^{(1)}(k_\rho\rho) & 0 \\ -\frac{i\sigma_g k_\rho}{\omega\epsilon_0}H_1^{(1)}(k_\rho\rho) & 0 & \frac{1}{2}\left(\frac{\sigma_g k_\rho}{\omega\epsilon_0}\right)^2 H_0^{(1)}(k_\rho\rho) \end{pmatrix}, \tag{2.51}$$

where $H_{\pm}^{(1)}(.) = H_0^{(1)}(.) \pm H_2^{(1)}(.)$. Additionally authors offer an extensive analysis of the dependence of the electric field strength (compared to free space radiation of the dipole) on frequency and distance of the observation point from the surface [72]. Their study suggests that for the frequency range and for the typical distances from the surface and away from the dipole that are used in our studies in this thesis, it is safe to assume that the total electric field, close to and on the surface, is dominated by the SPP surface wave electric field.

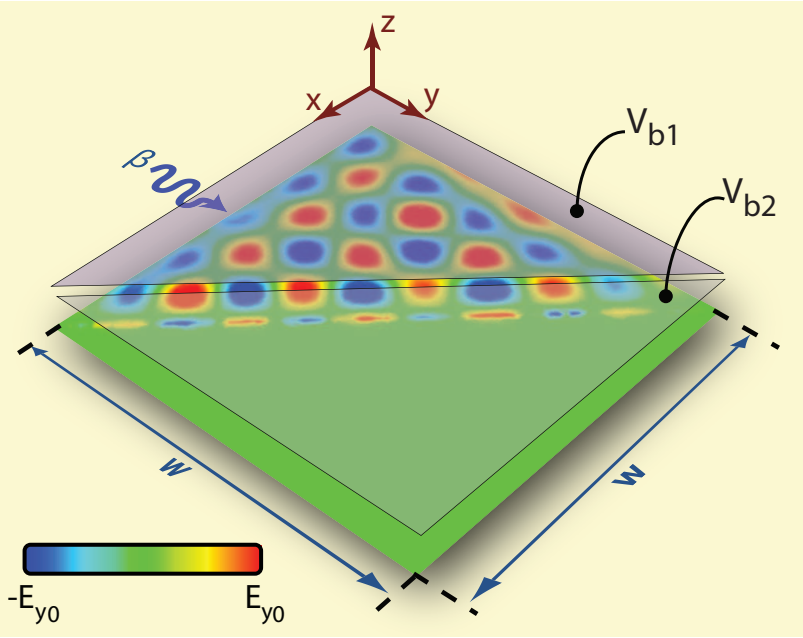

Figure 2.15: Fresnel reflection of SPP surface waves due to conductivity mismatch in plane of graphene. Our numerical simulation illustrates snap shot in time of y-component of the electric field, E_y for the near total reflection of a TM electromagnetic SPP wave on a free-standing graphene (w = 800 nm, T = 3° K, Γ = 0.43 meV, μ_c = 150 meV). $V_{b,1}$ and $V_{b,2}$ are chosen so that the two halves of graphene acquire complex conductivity values $\sigma_{g,1}$ = 0.0009 + i0.0765 mS and $\sigma_{g,2}$ = 0.0039 − i0.0324 mS. Reprinted from Ref. 106 (by permission of the AAAS). [http://www.sciencemag.org/content/332/6035/1291].

2.2.4 In-plane Fresnel reflection for SPP surface waves

Having the advantage of controlling and routing waves by reflecting them from boundaries is key to several functionalities such as bounding and guiding waves, and in turn in design of cavity resonators (see chapter 3). With that in mind, it is useful to investigate whether we can have concept of Fresnel reflection for surface plasmon-polaritons—similar to plane waves in classic optics—on a sheet of graphene, which is only one atom thick. If SPP waves can be reflected within the layer of graphene (without considerable amount of leakage), we can exploit such feature to design the spatial distribution of graphene conductivity to reflect and refract the SPP surface waves in desired patterns. To begin our discussion, we first analyze the geometry in Fig. 2.15. The conductivity values of two segments calculated

from the Kubo formula for $T = 3^\circ$ K and $\Gamma = 0.43$ meV are, respectively, $\sigma_{g,1} = 0.0009 + i0.0765$ mS and $\sigma_{g,2} = 0.0039 - i0.0324$ mS. The "farther" half section with $\sigma_{g,1} > 0$ supports a TM SPP, whereas the "closer" half with $\sigma_{g,2} < 0$ does not. Once a TM SPP is launched in the farther-half section toward the discontinuity resulted from mismatch in conductivities, it reflects back at that boundary line. Then, the incident and reflected waves add up and form an oblique standing wave.

The reflection of SPP from this boundary line is analogous to the Fresnel reflection of a plane wave from a planar interface between two mediums. Here, however, such reflection occurs across a one-atom-thick platform, with a considerably little radiation loss owing to high confinement of SPP to the graphene. This case might also be analogous to the Fresnel reflection from a planar interface between a medium that supports propagating waves (for example, a medium with a real refractive index, such as a dielectric) and another medium that does not support propagating waves (for example, a medium with no real index, such as a noble metal). Accordingly, on the graphene the Fresnel reflection of SPP results in a near complete reflection [106]. The simulation results demonstrate an effective reflection at the boundary line between the two segments.

In addition in Fig. 2.15 the simulation reveals a guided IR edge wave along the boundary line between the two segments. This phenomenon might be related to the separation of electrons and holes at the boundary region [13, 19, 20, 69]. Using an electron-holes liquid model, Mishchenko et. al [69] show that for plasmon wavelengths smaller than the size of charged domains, plasmon dispersion follows relation $\omega \propto \beta^{1/4}|\rho_0|^{1/4}$, where ρ_0 is the gradient of equilibrium charge density at the junction. In a geometrical optics framework, Cserti et. al [19] interpret this p-n junction as a negative refractive index. We may conclude that the second analogy described above is more laudable in explaining the physics behind the observed edge mode. Figure 2.16 demonstrate numerical simulation of this edge wave, which was excited using a horizontal dipole on the graphene and near the boundary of two

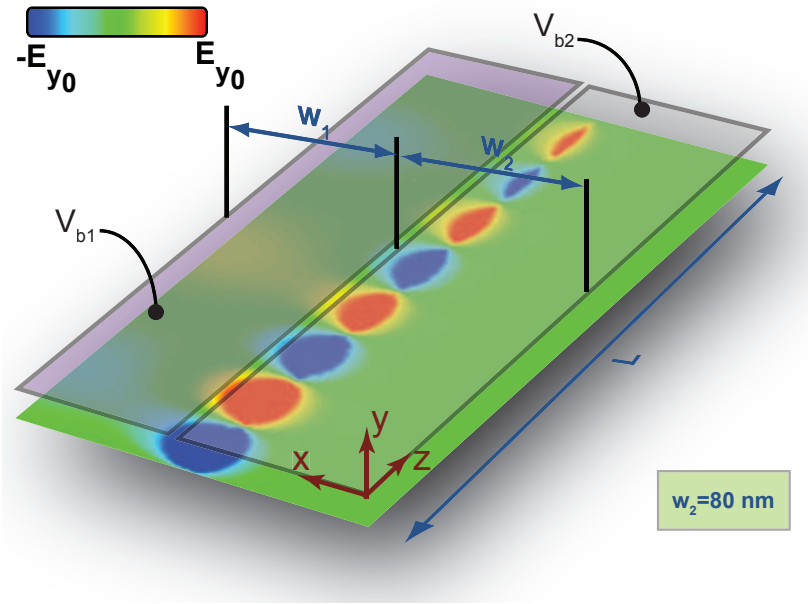

Figure 2.16: Distribution of E_y (snap shot in time) for a guided IR edge wave at $f = 30$ THz, supported along the boundary line between the two sections of the same sheet of graphene, which has two different conductivity regions ($\sigma_{g,1} = 0.0009 + i0.0765$ mS, $\sigma_{g,2} = 0.0039 - i0.0324$ mS, $L = 250$ nm, $w = 80$ nm). Reprinted from Ref. 107 (by permission of the AAAS). [http://www.sciencemag.org/content/suppl/2011/06/08/332.6035.1291.DC1/Vakil-SOM.pdf].

regions. This special guided wave propagates along a "one-atom-radius" boundary line. By post processing the simulation results, we estimate the wavelength of the guided edge wave to be around $\lambda_{SPP} = 61.5$ nm.

Sounas & Caloz [99] show that such edge surface mode that propagates along the edge of a graphene strip can be shorted using a PEC plate that is in the plane of the graphene strip. They also find the dispersion curve for the edge mode with and without magnetic bias.

A critical issue to address is how to quantify the reflection from the boundaries. Due to special geometry of graphene (very small thickness), finding an exact solution to this problem proves to be difficult. To study this problem, it might be possible to apply Wiener-Hopf analysis, which solves problem of diffraction by surface impedance discontinuities and impedance half-planes [90] but this analysis is cumbersome and may not provide much

insight into the problem. For practical purposes it might suffice to find an approximate solution, as by employing powerful computational resources available these days, one can always optimize any design based on first-order approximations. We have developed a simple semi-analytical approach based on a transmission-line (TL) analogy to quantify the reflection of SPP surface waves from discontinuities in plane of graphene.

We address normal incidence here. The case of oblique incidence can follow from the same analogy by proper modifications. Consider a graphene layer that has two segments with two different conductivity values (one may utilize any of the methods we proposed earlier to realize such nonuniformity in conductivity pattern). The reflection from edge of the second segment within the graphene layer might be analog of reflection from a "lumped" impedance terminating a transmission line. Figure 2.17 illustrates the analogy. Based on this analogy we can decompose the transverse component of the electric field (E_z) into two components: a forward traveling wave and a backward traveling wave which is reflected from the edge of graphene (or in our transmission line analogy from the terminating impedance). Suppose that the forward wave (traveling along y-direction) has the form $E_{z,0}e^{i\beta y}$, where β is the propagation constant (or complex wavenumber along y). The backward electric field will be of form $RE_{z,0}e^{-i\beta y}$, where R is the reflection coefficient due to the second region (or equivalently from the load at the end of the impedance). Writing the complex reflection coefficient as $R = \rho e^{i\theta}$, we can obtain the total transverse electric field just above the plane of graphene (say small distance δ) as follows

$$E_z = E_{z,0}e^{-p\delta}\left(e^{i\beta y} + \rho e^{i\theta}e^{i\beta y}\right), \tag{2.52}$$

where as before $p = \sqrt{\beta^2 - k_0^2}$. Noting that $\beta = \beta_r + i\beta_i$, Eq. (2.52) can be recast as

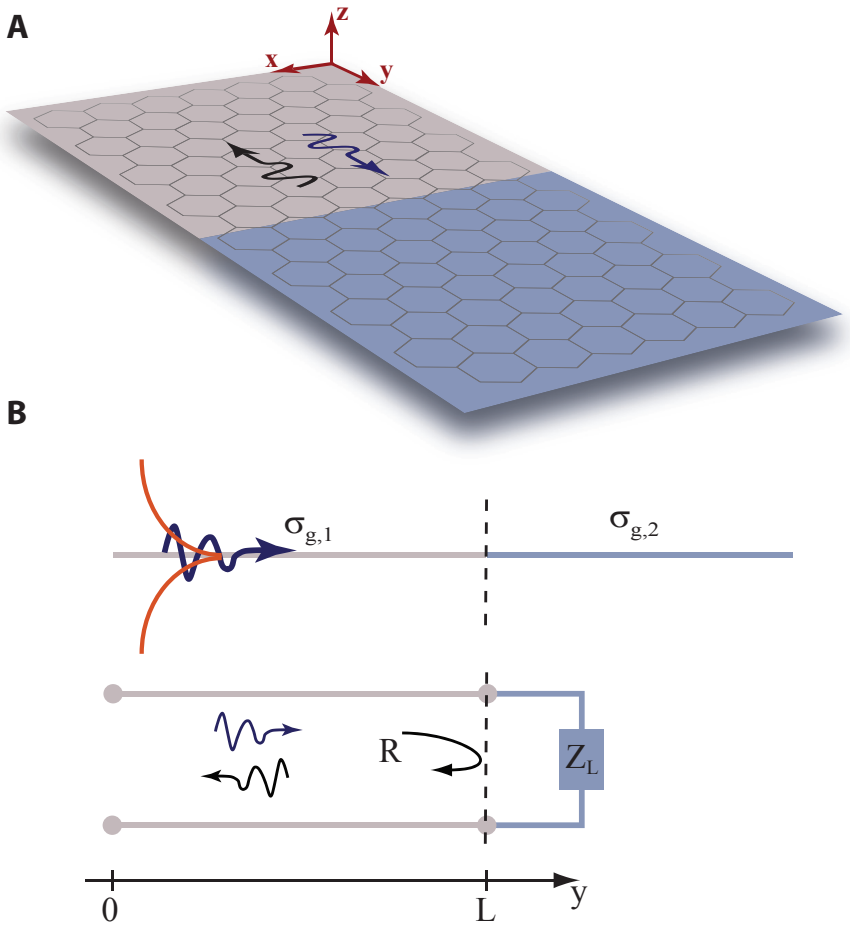

Figure 2.17: Reflection of surface plasmon polariton surface waves from edges: Transmission line analogy is used to find an approximate value for the reflection coefficient from the edge of second medium.

following

$$E_z = E_{z,0}e^{-p\delta}\left[\left(e^{-\beta_i y}\cos\beta_r y + \rho e^{\beta_i y}\cos\left(\theta-\beta_r y\right)\right)\right.$$
$$\left.+i\left(e^{-\beta_i y}\sin\beta_r y + \rho e^{\beta_i y}\sin\left(\theta-\beta_r y\right)\right)\right]. \quad (2.53)$$

We can obtain total field by solving Maxwell's equations using full-wave numerical simulations. Separating the transverse (y-component) of the electric field, we then find a set of parameters $(E_{z,0}, \beta_r, \beta_i, \rho, \theta)$ in Eq. (2.53) such that the curve described by this equation is fitted to the real and imaginary parts of numerical data points obtained from simulation. We find the optimal set of parameters by simultaneously minimizing the sum of square errors (SSE) between real and imaginary parts of data points from the equation and numerical simulations. Finally having values of ρ and θ, we can determine the complex reflection coefficient.

As a simple scenario, to illustrate how we can find the reflection coefficient from the edges, consider a graphene layer that is infinite in x-direction—meaning that there is no variation of the field in x-direction—and has finite length L in y-direction (Fig. 2.18). In the transmission line analog the graphene is described as a transmission line, whose end is left open to air. Simulation parameters are as usual ($\mu_c = 150$ meV and $\Gamma = 0.43$ meV) and frequency of operation is 30 THz. The layer is long enough to support multiple wavelengths of SPP surface waves. We consider a long structure to ensure that at the locations along the graphene layer where we fit our data points, the possible higher order electromagnetic modes due to edges have died out and do not affect our calculations. The distribution of the transverse electric field from numerical simulations is shown in Fig. 2.18.

Since the geometry and the fields are uniform in x-direction, we only need to fit the data points (real and imaginary parts) along an arbitrary line parallel to y axis (we have chosen y axis). Also in this process since δ (distance from plane of graphene) is very small, $e^{-p\delta}$ term is suppressed and its effect is absorbed in $E_{z,0}$. As explained earlier we solve for a

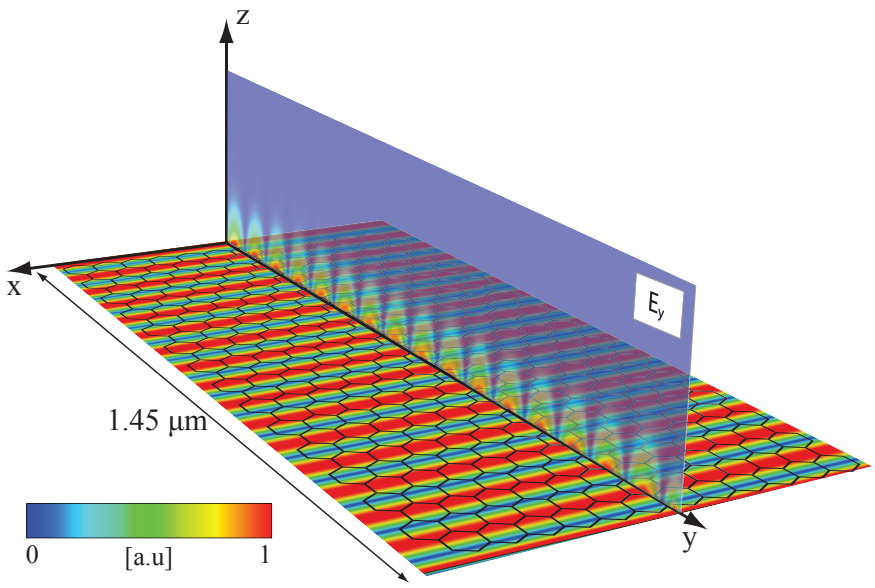

Figure 2.18: Study of reflection of SPP surface waves from edges. Based on our TL analogy we can regard the reflection from the edge of graphene as reflection from an open-ended transmission line. In the similar manner we can define impedance for such radiation we can do so for the radiation from the edge. The graphene layer has conductivity $\sigma_{g,1} = 0.0009 + i0.0765$ mS. The magnitude of the transverse component of the electric field (E_z) is shown on x-y and y-z planes.

set of parameters $(E_{z,0}, \beta_r, \beta_i, \rho, \theta)$ in Eq. (2.53) such that the SSE [difference between data points obtained using simulations and using corresponding data points based on Eq. (2.53)] is minimized. Implementing this procedure, we arrive at the results displayed in the second row of table 2.1 (in implementing the procedure, without loss of generality, we assume $E_{z,0} = 1$ and as such here we did not report this value).

Table 2.1: The set of parameters obtained from fitting numerical data to Eq. (2.53) for first two scenarios (see text).

Scenario	ρ	θ	β_r/k_0	β_i
$\mu_{c,1} = 150$ meV – air	0.8243	2.1027	69.77	1.05×10^{-4}
$\mu_{c,1} = 150$ meV – $\mu_{c,2} = 65$ meV	0.6825	1.4074	70.06	9.05×10^{-5}

Second scenario is similar to panel **A** from Fig. 2.17. Here the distribution of chemical potential of graphene layer is assumed to be non-uniform and two regions with two different

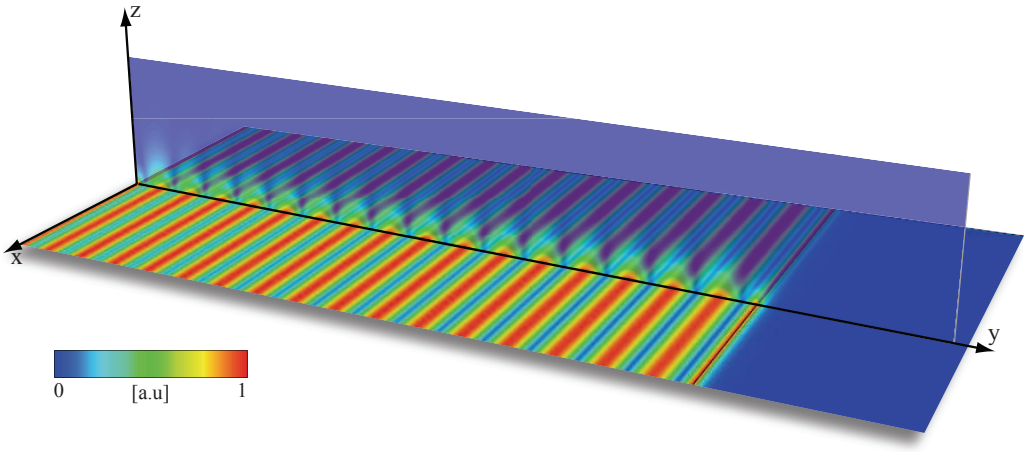

Figure 2.19: Study of reflection of SPP surface waves for the case where the first region (left) supports TM SPP surface waves ($\sigma_{g,1} = 0.0009 + i0.0765$ mS), while the second region (right) does not ($\sigma_{g,2} = 0.0039 - i0.0324$ mS). Magnitude of E_z is shown on x-y and y-z planes.

conductivities are formed. In this case we assume that at $f = 30$ THz region 1 (where the wave is launched; farther half in Fig. 2.17) has conductivity $\sigma_{g,1} = 0.0009 + i0.0765$ mS ($T = 3^\circ$ K) and region 2 (closer region) has $\sigma_{g,2} = 0.0039 - i0.0324$ mS. Thus this region does not support TM SPP surface waves and it is interesting to investigate how surface waves reflect upon hitting this region. This study could be useful for a "one-atom-thick" variant of a metal-insulator-metal (MIM) waveguide in classic optics. Also note that the structure is infinite in width and $k_x = 0$ ($\partial/\partial x = 0$). Since there is a mismatch between conductivity of these two regions, an SPP surface wave launched in region 1, reflects back from the boundary line of region 2 (similar to the case we studied earlier). These two forward and backward waves add up to form a total field, which its transverse component is displayed in Fig. 2.19. Again using similar steps pointed out for previous case, we can obtain the set of parameters $(\beta_r, \beta_i, \rho, \theta)$. The results are displayed in the third row of table 2.1.

As a third scenario, consider the same geometry as in Fig. 2.17, **A**, however now suppose that the second region (closer segment) has a conductivity value that does support

TM SPP waves. Addressing this type of reflection (where two media do support propagating modes) could form foundations for design of waveguides based on total internal reflection—similar to a optical fiber waveguide where core and cladding both support light modes, but due to total internal reflection of light-waves, the mode remains bounded in the core region. One subtle issue here is that the reflection coefficient obtained based on the forward and backward wave in the first region is not simply due to reflection from second region conductivity mismatch, but also due to the effect of the mismatch and reflection from the edge of the second region; there is a propagating forward mode in the second region, reflecting from the edge of this region. The reason we cannot suppress this reflection from edge is that design of perfect absorbing wall is a challenging task in our geometry (as we will discuss in appendix B we have attempted to resolve this issue by redesigning concept of Salisbury sheet for a TM SPP mode on graphene, but this absorbing boundary condition does not work perfectly, so we do have some reflection, albeit small, from the edges if we use this absorbing boundary conditions).

Consequently we decided to add a third region at the end of the second region, whose imaginary part of conductivity is negative, so it does not support SPP surface waves. As such there will not be any propagating modes in the third region and we do not need to be concerned about reflection in this region, as modes die out before reaching the edge of the graphene layer (this as well is the case for the second scenario discussed above). By finding reflection from region 2 in region 1 and from region 3 in region 2, we can back out the reflection in region 1 due to only region 2 (as if the second region was extended to infinity in *y*-direction, so there was no backward wave). In order to retrieve this reflection coefficient, we again exploit a transmission line analogy as depicted in bottom panel of Fig. 2.20. If we respectively denote the individual reflection from region 2 in region 1 – due to *only mismatch* – and reflection from region 3 in region 2 as Γ_{12} and Γ_{23}, then the total reflection (due to both mismatch and reflection from edge of third medium), Γ_{in} can

be obtained from following equation [7, 17]

$$\Gamma_{\text{in}} = \frac{\Gamma_{12} + \Gamma_{23} e^{i2\beta_2 d}}{1 + \Gamma_{12}\Gamma_{23} e^{i2\beta_2 d}}, \tag{2.54}$$

where d is length of the second region (in this example $d = 1.8\ \mu$m and $\beta_2 \approx 30k_0$). Γ_{12}, which is only due to mismatch of conductivities (as if we had two semi-infinite sheet of graphene with conductivities $\sigma_{\text{g},1}$ and $\sigma_{\text{g},2}$), can be computed from Eq. (2.54) in terms of Γ_{in} and Γ_{23}, which could be obtained from our numerical simulations

$$\Gamma_{12} = \frac{\Gamma_{23} e^{i2\beta_2 d} - \Gamma_{\text{in}}}{\Gamma_{\text{in}}\Gamma_{23} e^{i2\beta_2 d} - 1}. \tag{2.55}$$

To compute Γ_{in} and Γ_{23} using numerical simulations, we repeat the same steps as before in fitting data points to find the optimal set of parameters for Eq. (2.53). The results are reported in second and third rows of table 2.2. Using these values from table 2.2 and Eq. (2.55), we find individual reflection coefficient due to region 2 to be $\approx 0.47 e^{i\pi/2}$.

Table 2.2: The set of parameters obtained from fitting numerical data to Eq. (2.53) for third scenario scenarios (see text).

Scenario	ρ	θ	β_{r}/k_0	β_{i}
$\mu_{c,1} = 150$ meV $-\ \mu_{c,2} = 300$ meV	0.6070	0.4417	72.30	4.31×10^{-4}
$\mu_{c,1} = 300$ meV $-\ \mu_{c,2} = 65$ meV	1.00	0.4561	30.47	1.59×10^{-4}

As one last point in this part we would like to distinguish between reflection from the plane of graphene and in-plane reflection of SPP surface waves propagating along a graphene layer with nonuniform conductivity (for example Fig. 2.17). These are two completely different problems. In this section we addressed the latter as it is what we need in our paradigm of "one-atom-thick" optical metamaterials and transformation optics. The former problem has been addressed by others [27, 41][‖]. We would like to also note that

[‖]It can be shown that for normal incidence the reflection from a graphene layer with complex surface conductivity σ_{g} is $R = \frac{\sigma_{\text{g}}\eta_0/2}{1+\sigma_{\text{g}}\eta_0/2}$ and transmission coefficient is $T = 1 + R$.

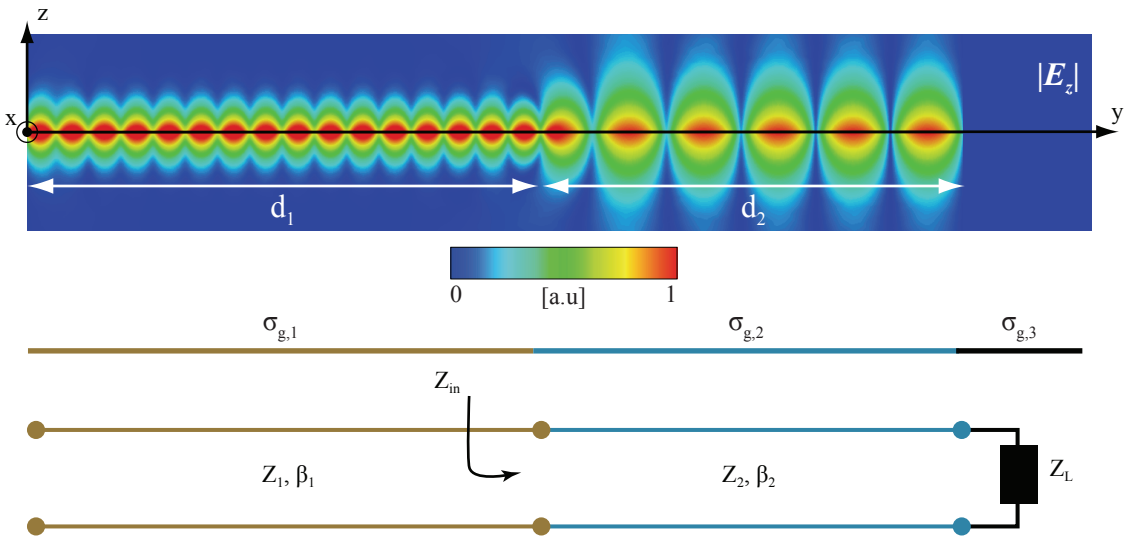

Figure 2.20: Study of reflection of SPP surface waves for the case where both regions support TM SPP surface waves ($\sigma_{g1,i}, \sigma_{g2,i} > 0$). Magnitude of E_z is shown on the y-z plane. Bottom panel depicts the transmission line analog of the geometry ($d_1 \approx 2.2\,\mu$m, $d_2 \approx 1.8\,\mu$m).

the problem of reflection from plane of graphene is a rich and interesting area by itself and several ideas may follow from that study. For example Sounas & Caloz [100], theoretically, and Crassee et. al [18], experimentally, have studied reflection from a graphene layer under magnetic bias and observed that the geometry under study can exhibit a broadband electromagnetic nonreciprocity and gyrotropic behavior (Faraday rotation), which can serve as basis for design of magneto-optical devices such as nonreciprocal phase shifters.

2.2.5 Scattering from subwavelength graphene patches

As mentioned in chapter 1, metamaterials are artificial structures that mimic physically realizable response functions and they are usually constructed by embedding subwavelength inclusions or inhomogeneities in a host medium. Thus it is of particular significance to describe behavior of such inclusions or inhomogeneities, as their collective behavior forms the total optical response function of the medium. Addressing this problem is essentially

reduced to study of the problem of scattering from subwavelength inhomogeneities. As it is known for a bulk metamaterial structure, we have classic Clausius-Mossotti formalism that relates the effective permittivity of a bulk material to the polarizability of inclusions or inhomogeneities. In effect such treatment assumes that any inclusion or inhomogeneity, small engough compared to the wavelength, can be regarded as a dipole moment with a strength that is captured by its polarizability.

Accordingly, it is important to study the same problem in the one-atom-thick world of graphene as quantifying response of subwavelength inhomogeneities (e.g., subwavelength disks or patches that have different conductivity than that of their surrounding region) is key to design of graphene-based metamaterials. Let us consider the case of a subwavelength circular patch (nanodisk) as an inhomogeneity in a host graphene layer. Figure 2.21, **A**, illustrates the geometry. The side of the graphene layer is about $10\lambda_{\mathrm{SPP}}$ and the diameter of the disk is 20 nm. The chemical potential for the background graphene is 150 meV (at 30 THz, for $\Gamma = 0.43$ meV, we have $\sigma_{\mathrm{g,bg}} = 0.0009 + i0.0765$ mS), while the the chemical potential for the small nanodisk is 65 meV ($\sigma_{\mathrm{g,disk}} = 0.0039 - i0.0324$ mS). The question is whether such a nanodisk can be described as a dipole. To answer this question we studied the structure using numerical simulations.

The structure is illuminated with a plane wave with polarization shown in panel **A**. We then consider the scattered (or secondary) field, which is total field from full-wave numerical simulations minus the incident field. Figure 2.21, **B** through **C**, display the three components of this scattered field. As clearly can be seen the nanodisk indeed acts as small dipole oriented in *y*-direction (similar to the field profile of a horizontal dipole from section 2.2.3 and Figs 2.13 and 2.14). The question remained to be answered is how to quantify the strength of this dipole moment. To address this question, we need to quantify the nanodisk's polarizability, which in general is a function of dimensions and optical properties of the disk and its surrounding medium. As was the case with the reflection

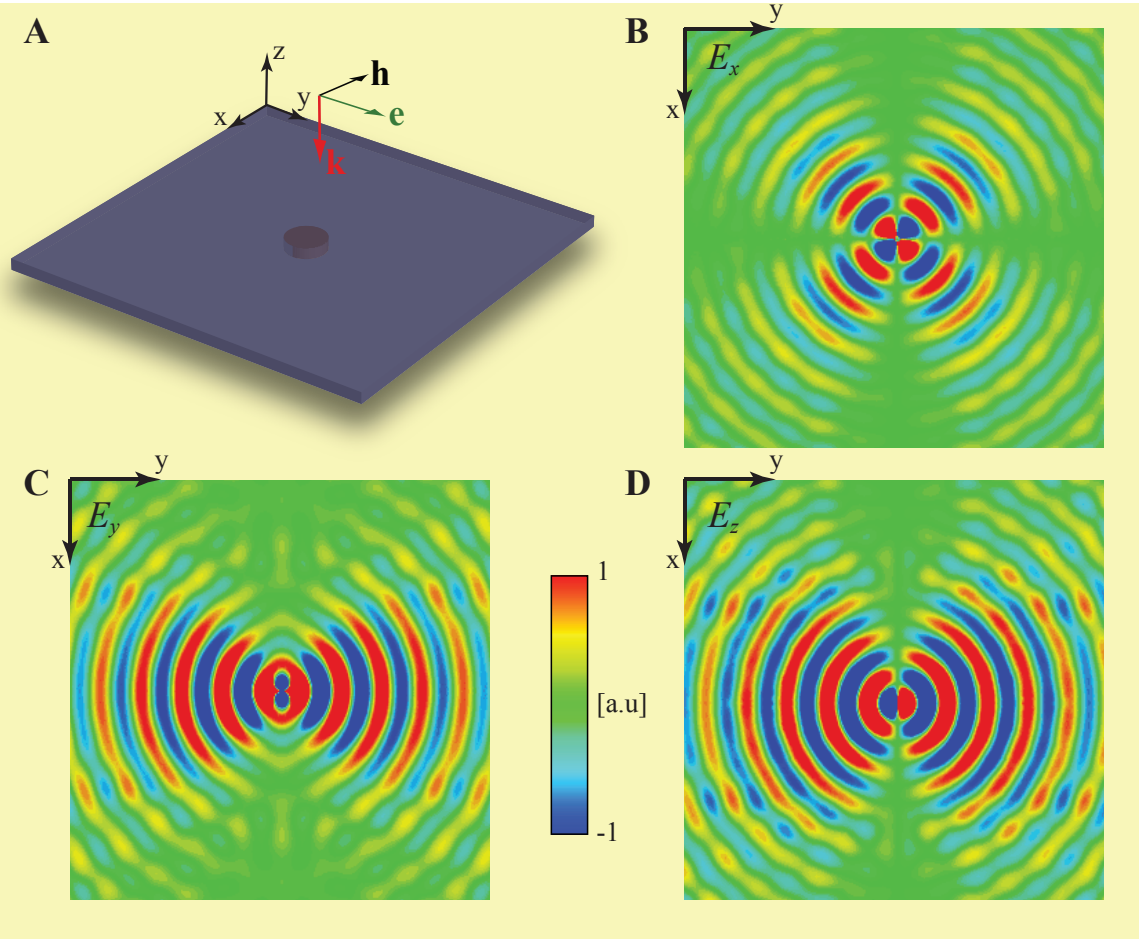

Figure 2.21: Scattering of SPPs by a nanondisk. **A** Geometry of problem: a subwavelength disk with a different conductivity from conductivity of the host graphene. The structure is illuminated with a plane-wave from top. The nanodisk (r = 10 nm), acts as dipole. **B** through **D** show the snapshot in time of different components of the secondary (i.e., scattered) electric field due to the patch; the incident field has been removed from the total field calculated from numerical simulations. The fields due to the nanodisk mimics the fields of a dipole. The issue is how to find the polarizability of such nanodisk as function of its dimensions and optical properties.

problem (see section 2.2.4), full-analytical treatment of the problem might not be straightforward if not impossible. There have been some studies on how light scatters from a small hole in a thick metal film [91] such as gold, however again very thin structure of graphene makes such studies almost obsolete in this case. Thongrattanasiri et. al [103] have suggested that polarizability of a small subwavelength graphene disk follows a resonance that has a Lorentzian line shape

$$\alpha(\omega) = \frac{3c^3\kappa_r}{2\omega_p^2}\frac{1}{\omega_p^2 - \omega^2 - i\kappa\omega^3/\omega_p^2}, \tag{2.56}$$

where ω_p is the plasmon frequency, κ is the decay rate, and κ_r is the radiative component of κ. Then using full-wave numerical simulations the fitting parameters κ, κ_r and ω_p can be determined. These parameters implicitly bear the dependence on the dimensions and optical properties of the nanodisk.

In addition, using full-wave simulations, we obtain the polarizability of a circular patch as a function of its radius. The simulations are performed for $f = 30$ THz, at which the circular patch has conductivity $\sigma_{\text{g,disk}} = 0.0039 - i0.0324$ mS ($\mu_c = 65$ meV) and the background conductivity is $\sigma_{\text{g,bg}} = 0.0014 - i0.1787$ ($\mu_c = 300$ meV). To find the dipole polarizability of the disks, the radius of the circular patch is varied from 2 nm to 20 nm and the magnitude and phase of the scattered electric field ($|E_{\text{inc}}| = 1$) due to the disk is compared with a deeply subwavelength dipole source with dipole moment $p = 1$ (in our simulation we assumed the length of the dipole source is 2 nm). We do realize that these length scales are not realistic, however we wanted to make sure that the diameter of the disks are indeed subwavelength (with respect to λ_{SPP}, which in this scenario is ≈ 336 nm). The results are shown in Fig. 2.22. As expected, the magnitude of the polarizability increases with the size of the disk (roughly $\propto a^3$). In addition, the higher the conductivity contrast between the disk and the background, the larger the polarizability of the disk.

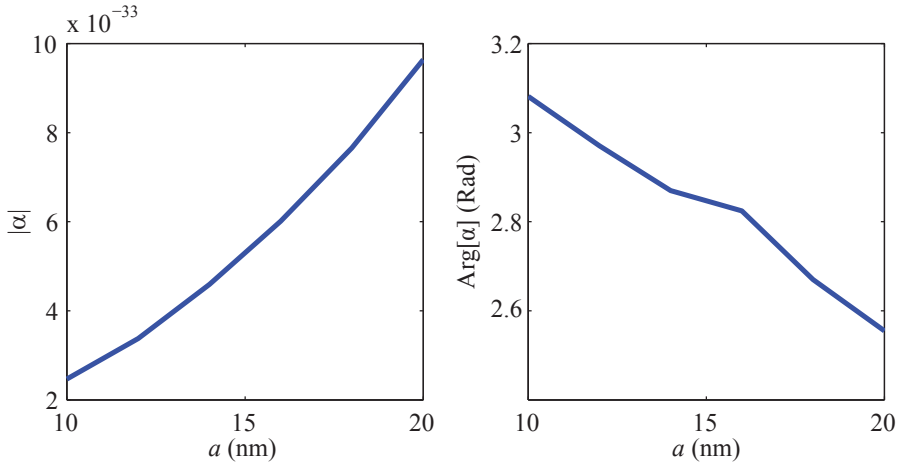

Figure 2.22: Polarizability of graphene nanondisk as a function of its radius (right panel: magnitude, left panel: phase angle).

Graphene antennas

The problem of scattering from subwavelength patches is the critical to study of several other problems. For example we just showed a single patch of graphene can effectively act as an emitter within graphene, suggesting such entity could be employed as an antenna to receive and transmit signals in and out of the graphene layer. To show coupling efficiency of the SPP using the graphene patch, we use a quantity called coupling cross section σ_c defined as $\frac{P_{rec}}{S_{inc}}$, where P_{rec} is the power received by the patch and S_{inc} is the incident power per unit area. Our calculation indicate that this subwavelength patch has a coupling cross section more than 4 times its geometrical area (we obtained almost the same value for a hole of the same size instead of the patch). This quantity depends on the shape, dimensions and conductivity of the patch and conductivity of the surrounding medium, so creating high contrast between the conductivity of the patch and that of the background graphene should result in larger coupling cross sections. This could be subject of further study.

The possibility of inclusions as antennas has been examined experimentally by Zhou et. al [120]; they show that surface plasmons can be enhanced even locally and at the atomic

scale using point defects. Their study indicates that a single point defect (which is created by using dopant atoms such as boron, nitrogen, iron, silver of gold) can act as an "atomic antenna" in the petahertz region. There has been some numerical studies similar to what presented here (see Ref. 62)**.

2.2.6 Coupling between an emitter and graphene SPPs: Enhanced light-matter interaction

In section 2.2.3 we studied the solutions to Maxwell's equations in the presence of graphene and also how graphene can change radiation pattern of an emitter in free-space. We observed that presence of graphene can give rise to surface plasmon polariton waves at the surface, which are much stronger than the fields due to an emitter in free-space.

Before Purcell's study in 1946, spontaneous emission of an atom or molecule was deemed as an intrinsic property of such entity. But his work suggested that the environment surrounding an atom or molecule can alter radiative characteristic of the atom or molecule. There have been some studies on the strength of coupling of quantum emitters and graphene surface plasmon-polaritons. These studies predict high decay rates for such quantum emitters in the proximity of the homogeneous and inhomogeneous graphene layer [43, 54]. Koppens et. al [54] propose that due to this high decay rate (spontaneous emission rate), graphene can be a new platform for enhanced light-matter interaction. They study the problem in a quantum optical context. We briefly discuss some of the theoretical concepts underlying their study as they closely relate to our work on graphene-based cavities in chapter 3. In chapter 3, we treat the problem of cavity classically and try to analyze the cavity response using circuit models for resonance. In our framework, there is

** Another interesting scenario in which scattering problem find importance is the inverse scattering from objects within graphene layer. As we point out very briefly in chapter 5, inverse scattering problem is of immense significance in tomography applications using graphene—e.g., in imaging of a rough surface.

an analogy between the quantum and the classical view of the problem. We will see how, in such framework, decay rate of a quantum emitter can be regarded as a resistive part of impedance of an antenna [35].

The spontaneous emission rate γ of a the dipole can generally be obtained using Fermi's golden rule [77] by considering the combined "field + system" states in terms of *partial local density of states*[††] of the dipole $\rho_p(\mathbf{r}_0, \omega_0)$,

$$\gamma = \frac{2\omega_0}{3\hbar\epsilon_0}|\mathbf{p}|^2\rho_p(\mathbf{r}_0, \omega_0), \tag{2.57}$$

in which $\mathbf{r}_0$ is the location of dipole, ω_0 is the transition frequency and $\mathbf{p}$ is the dipole moment of the atom or molecule (this discussion is based on the assumption that our dipole can be described as a two-level quantum system). The density of states is related to Green's tensor of the dipole at the location of dipole:

$$\rho_p(\mathbf{r}_0, \omega_0) = \frac{6\epsilon_0}{\pi\omega_0}\left[\hat{\mathbf{p}} \cdot \Im\{\overleftrightarrow{\mathbf{G}}(\mathbf{r}_0, \mathbf{r}_0; \omega_0)\} \cdot \hat{\mathbf{p}}\right], \tag{2.58}$$

where $\hat{\mathbf{p}}$ is $\frac{\mathbf{p}}{|\mathbf{p}|}$ and $\overleftrightarrow{\mathbf{G}}(\mathbf{r}_0, \mathbf{r}; \omega_0)$ is the Green's tensor at the location of dipole $\mathbf{r_0}$ due to the dipole itself—the electric field at location $\mathbf{r}$ due to the dipole is $\mathbf{E}(\mathbf{r}) = \overleftrightarrow{\mathbf{G}}(\mathbf{r}_0, \mathbf{r}) \cdot \mathbf{p}$. For free-space the decay rate γ_0 of the dipole will take the simple following form

$$\gamma_0 = \frac{\omega_0^3|\mathbf{p}|^2}{3\pi\epsilon_0\hbar c^3}. \tag{2.59}$$

An important quantity that captures the effect of environment on the rate of spontaneous emission of an emitter is *Purcell factor*, defined as the total decay rate of the emitter normalized to the free-space decay rate. It can be shown that this quantity only depends on the scattered field due to the inhomogeneous environment [77]

$$\boxed{\mathrm{F_p} = \frac{\gamma}{\gamma_0} = 1 + \frac{6\pi\epsilon_0}{|\mathbf{p}|^2}\frac{1}{k_0^3}\Im\{\mathbf{p} \cdot \mathbf{E}_\mathrm{s}(\mathbf{r}_0)\}}, \tag{2.60}$$

[††]Partial local density of states is defined as number of modes per unit volume and frequency at the origin of the quantum system

where $\mathbf{E}_s(\mathbf{r}_0)$ is the scattered field at the location of the dipole. In Eq. (2.60) interaction between $\mathbf{E}_s$ and $\mathbf{p}$ is assumed to be weak. Also it has been assumed that the decay rate is purely radiative.

Now let us briefly discuss the connection between classic and quantum picture of the problem. As we know from classical point of view, according to Poynting's theorem, for any *source* or *sink* current distribution $\mathbf{j}$ in a linear medium, the rate of energy dissipation dW/dt should be equal to power radiated by that source [77]

$$\frac{dW}{dt} = -\frac{1}{2}\int_{\mathrm{V}} \Re\{\mathbf{j}^* \cdot \mathbf{E}\} dV. \tag{2.61}$$

Thus for a dipole $\mathbf{j}(\mathbf{r}) = -i\omega_0 \mathbf{p}\delta(\mathbf{r} - \mathbf{r}_0)$, we can write

$$\frac{dW}{dt} = \frac{\omega_0}{2}\Im\{\mathbf{p}^* \cdot \mathbf{E}(\mathbf{r}_0)\}, \tag{2.62}$$

where $\mathbf{E}(\mathbf{r}_0)$ is electric field due to the dipole at its own location. This equation can be written in terms of Green's tensor as

$$\frac{dW}{dt} = \frac{\omega_0^2 |\mathbf{p}|^2}{2}\left[\hat{\mathbf{p}} \cdot \Im\{\overleftrightarrow{\mathbf{G}}(\mathbf{r}_0, \mathbf{r}_0; \omega_0)\} \cdot \hat{\mathbf{p}}\right]. \tag{2.63}$$

The connection between two point of views becomes clear by comparing combination of Eqs. (2.57) and (2.58) with Eq. (2.63). We will come back to this analogy later in chapter 3, where we talk about one-atom-thick cavity resonators using graphene. There we use classic electrodynamics to analyze the problem of cavity resonator (i.e., by considering quantities such as Q-factor, mode-volume) and try to present a circuit equivalent for the cavity resonator. The decay rate of the system will be closely related to the resistive part of impedance introduced for the two-level system [35].

2.2.7 Excitation of graphene surface plasmon-polaritons

As discussed in sections 2.2.3 and 2.2.6, one efficient way of exciting surface plasmon-polaritons in graphene is to use a quantum emitters such as an atom or molecule resonat-

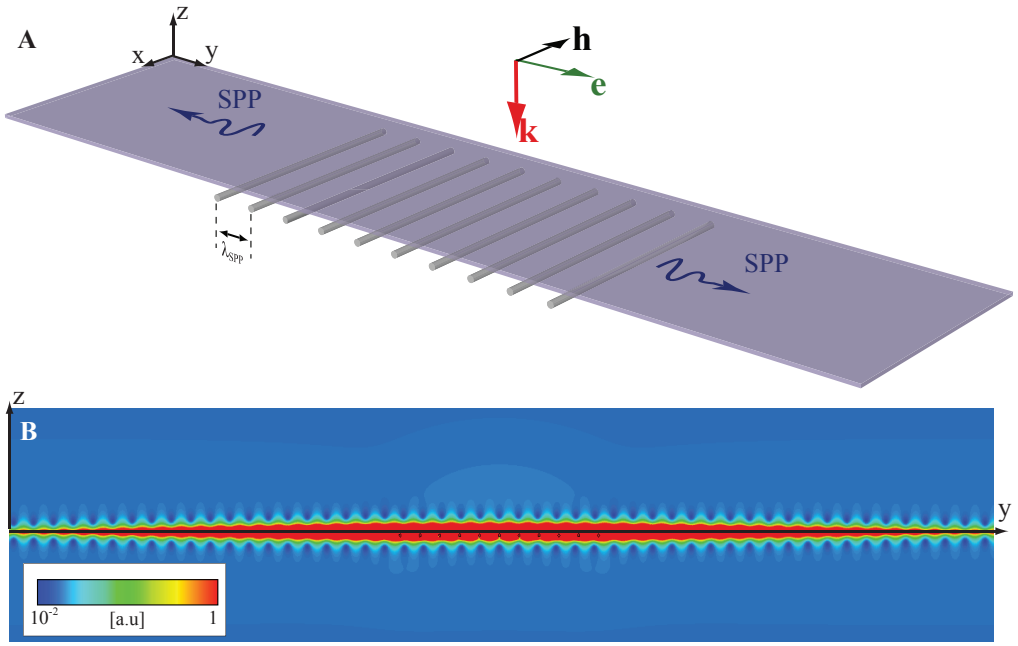

Figure 2.23: Excitation of SPPs using diffraction grating. All fields shown here are the scattered component; the incident component is removed. Panel **A** shows the geometry of the graphene layer, the diffraction grating and polarization of incident field. Panel **B** illustrates the magnitude of the scattered field on *y*-*z* plane.

ing at the desired wavelength. In this section, we investigate other possibilities to excite graphene SPP modes. The central notion here is to excite these modes using a plane wave. Due to high confinement of the SPP surface waves, coupling in and out of graphene is very challenging. In addition, as we will see here, with conventional techniques of coupling light with SPP surface waves, the efficiency is undesirably low.

Excitation of surface plasmon-polaritons using diffraction grating

One method for excitation of SPPs is similar to diffraction grating structure in conventional optics (see Fig. 2.23, **A**). Suppose that a graphene layer with $\mu_c = 150$ meV ($T = 3°$ K, $\Gamma = 0.43$ meV) is standing in free space, while ten silver nanorods ($r \approx 8$ nm), distanced $\lambda_{SPP} \approx 144$ nm from each other, are placed underneath and very close to the graphene (in

a real setup the nanorods can be embedded in the spacer, upon which graphene is rested; the physical mechanism underlying the problem will remain unaffected). A plane wave launched from the top toward the graphene layer (which, in our simulations, is $50\lambda_{\mathrm{SPP}}$ long in y-direction and infinite in x-direction, i.e. $\partial/\partial x = 0$), will induce dipole moment in the nanorods and the since the these nanorods are separated by λ_{SPP}, the fields due the dipole moments add up in phase, giving rise to SPP surface waves in the graphene layer. We studied this structure numerically by full-wave simulation of total field (which is sum of incident plane wave field and secondary field formed by scattering from graphene + grating system) and removing the incident component to obtain the scattered (secondary) field. Figure 2.23, **B**, illustrates the magnitude of scattered field on the y-z plane. From this simulation we can clearly observe the SPP mode and how it is confined to the graphene layer. Unfortunately, with this geometry the coupling efficiency is as low as $\sim 0.1\%$. Since radius of the wires is very small, the dipole moment induced in the nanorods is extremely small, resulting in this weak coupling. As expexted efficient coupling to graphene's extremely confined SPP surface waves is a challenging task; for example merely increasing the diameter of the nanorods does not result in considerably more effective coupling; for example increasing the radius from 8 nm to 35 nm, leads to a coupling efficiency of $\sim 0.55\%$, which is still very small. As we will point out in the follwoing section (see Remark in subsection 2.2.7), to achieve larger coupling, one needs to exploit techniques that are based on mechanisms different from those employed conventionally.

Excitations of surface plasmon-polaritons using array of patches

Based on the discussion in section 2.2.5, here we propose another way of coupling to graphene SPPs. Using arrays of circular patches, we might be able to achieve higher coupling efficiency. For example consider the geometry in Fig. 2.24, **A**, where the background

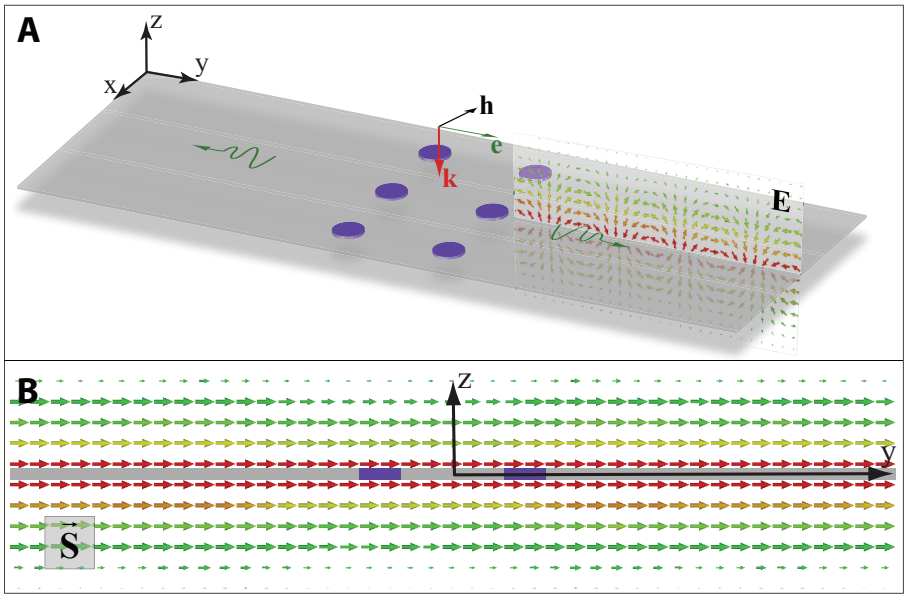

Figure 2.24: Excitation of SPPs using array of subwavelength disks. Panel **A** shows the geometry and distribution of the vectorial scattered electric field on the *y*-*z* plane (snap shot in time). Panel **B** illustrates the Poynting's vector of the SPP surface wave on *y*-*z* plane.

graphene has conductivity with positive imaginary and patches conductivity has negative-valued imaginary parts (conductivity values are the same as what used throughout this thesis). In our simulation the radius of each patch is 10 nm and we assumed that the two arrays are separated by λ_{SPP} in the longitudinal direction while they are $\lambda_{\mathrm{SPP}}/5$ apart from each other in lateral direction. The patches act as antennas and when the structure is illuminated with a plane wave, one can couple photons to the SPP modes of graphene through these patches. With this geometry and only two rows of these arrays, we achieved coupling efficiency of $\sim 0.6\%$, which is still small but larger than the grating structure proposed earlier. By changing shape and dimension, and by increasing number of arrays, we might be able to achieve larger coupling. Figure 2.24, **A**, illustrates the electric field of SPP surface wave coupled using this technique on the *y*-*z* plane (the structure is uniform in *x*-direction). Figure 2.24, **B**, shows the Poynting vector of the SPP wave. It is clear that the power is confined around the graphene layer.

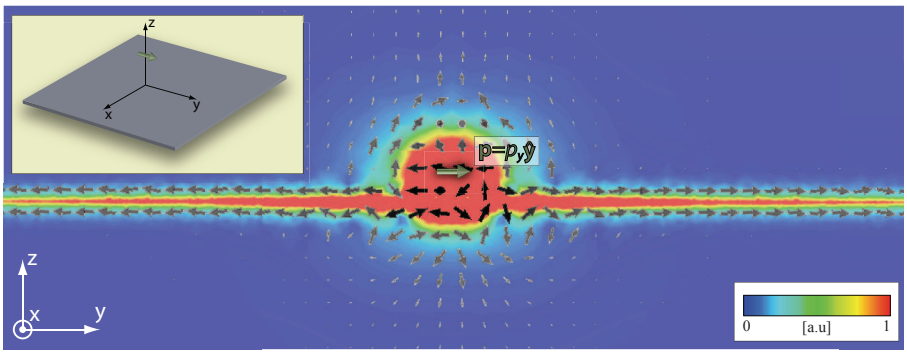

Figure 2.25: A horizontal dipole on top of a uniform graphene layer with $\mu_c = 300$ meV. The distance of dipole from graphene is 200 nm. The inset shows the geometry under study. The Poynting vector (strength shown in gray scale) is superimposed on top of the density plot of the electric field intensity.

Remark: As we just observed both techniques described above result in very low coupling efficiencies, but studies have shown that an emitter in close proximity of a graphene layer can couple efficiently to plasmon modes of graphene (see Ref. 43 for example). Figure 2.25 shows numerical simulation of electric field and Poynting vector due to a horizontal dipole near surface of graphene layer with uniform chemical potential $\mu_c = 300$ meV.

As can be seen from Fig. 2.25, the total field is combination of two main components: dipole radiation field and SPP field. Based on the numerical simulation of our geometry, roughly 80% of the dipole power couples to dipole radiation fields, while the rest radiates into SPP waves (i.e., assuming all the energy loss of the source is associated with radiation, $\frac{P_{\text{SPP}}}{P_{\text{rad}}} = \frac{\gamma_{\text{SPP}}}{\gamma_{\text{rad}}} = \frac{1}{4}$). However Huidobro et. al have shown that, under certain conditions, in principle the total decay rate γ can become almost equal to the surface plasmons decay rate γ_{SPP} [43], implying that most of the emitter's power can radiate into SPP. So why do we observe such a small coupling in the techniques proposed above? The reason can be attributed to inefficient coupling between the plane wave and the scatterers, i.e., the nanorods in the first proposal and patches in the second proposal. In other words, as we mentioned

earlier the dipole moments induced by the plane wave in the scatterers are extremely small, resulting in small amount of power radiating from the scatterers into the dipole radiation and SPP fields, so no matter how large is the coupling efficiency between the scatterers and graphene plasmons, the amount of power radiated into plasmons is small compared with incident power (i.e., power of the incident plane wave). To tackle this issue somehow the Poynting vector has to, as much as possible, be directed toward the scatterers, enabling larger interaction between particle and the plane wave.

Suppose for example that the emitter is a spherical subwavelength nanoparticle. It is well known that if the particle becomes resonant the scattering cross section of the particle can exceed several multiples of the particle's actual cross section (for a spherical nanoparticle for example typical values for scattering cross section is multiples of $\frac{\lambda_0^2}{2\pi}$). It has been shown that by proper design of a plasmonic-dielectric-plasmonic layered structure, in principle, an arbitrarily large total cross section can be achieved [92][‡‡]. Such possibility can find significance in efficient coupling of power of a plane wave to graphene SPPs. This problem is subject of future studies.

[‡‡]By engineering a layered nanostructure, resonances can occur in several angular momentum channels that have almost the same resonance frequencies (degeneracy), leading to relatively larger than usual scattering cross sections for subwavelength particles, which are coined as 'superscatterers' [92].

Chapter 3

Metamaterials and Transformation Optics using Graphene

In chapter 2, we saw that conductivity of graphene can be controlled by tuning its chemical potential. Changing chemical potential can be achieved by chemical doping or using static electric bias. We also proposed some methods to vary chemical potential based on static electric biasing. By devising one of those methods, one can tailor the conductivity locally to create inhomogeneous nonuniform patterns across the layer of graphene. As we mentioned, a graphene layer with positive imaginary part of conductivity supports TM surface plasmon-polariton surface waves, while for negative imaginary parts, these modes are not sustained and a weakly guided TE mode is present. Of course in case of positive imaginary part, depending on the value of this quantity, the modes can possess different propagation characteristics. The ability to manipulate conductivity of graphene can lead to rebirth of fields of “metamaterials” and “transformation optics” on a flatland platform for terahertz and infrared frequencies. Metamaterials are designed upon notion of embedding inclusions and inhomogeneities and transformation optics is based on the idea of creating gradient in refractive index of materials to redirect the electromagnetic waves at will. Both of these

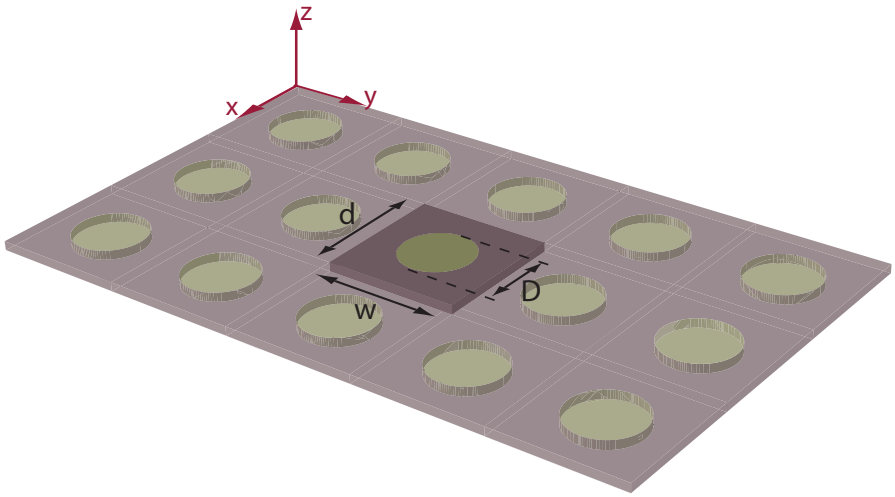

Figure 3.1: Schematic of a free-standing graphene layer, with an array of circular "patches" as inhomogeneities. The layer might act as a 2D variant of a metamaterial structure.

can be realized using graphene.

To begin our discussion, we present a general example of a metamaterial structure. In subsequent sections we study more specific examples*.

Figure 3.1 is sketch of a free-standing layer of graphene, within which an array of 2D circular "patches" is assumed. The conductivity of these patches is $\sigma_{g,2} = 0.0039 - i0.0324$ mS ($\sigma_{g2,i} < 0$), whereas the rest of graphene has conductivity $\sigma_{g,1} = 0.0009 + i0.0765$ mS ($\sigma_{g1,i} > 0$). Each circular patch acts as a scatterer for the SPP surface wave, behaving as a "flatland inclusion". The collective behavior of these "inclusions" can result in a 2D bulk flat metamaterial.

Our numerical simulations (shown in Fig. 3.2) suggest that such geometry, if designed properly, can act as a 2D version of metamaterials formed by collection of subwavelength metallic nanoparticles that may, under certain conditions, exhibit backward wave prop-

*In our examples we have tried to avoid length scales less than 20 nm, which has been shown to be the limit for quantum finite-size effects to emerge; below 20 nm it is predicted that the plasmon resonances will split and we may observe broadening of the resonances [104]

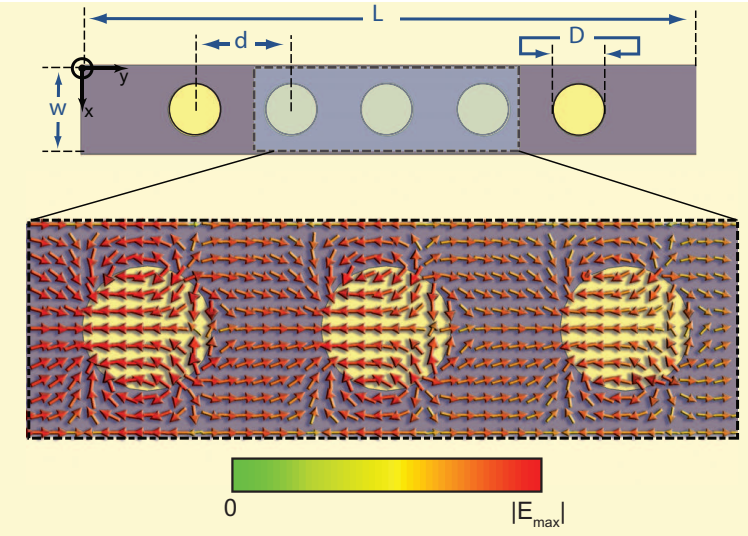

Figure 3.2: The snapshot in time of the electric field vector for the TM SPP along a single sheet of graphene at $f = 30$ THz, shown on the graphene plane. Only one row of the 2D periodic array is shown ($D = 30$ nm, $d = w = 55$ nm, $L = 370$ nm). Reprinted from Ref. 106 (by permission of the AAAS). [http://www.sciencemag.org/content/332/6035/1291].

agation effect [4]. Considering this example, now the importance of our discussion in section 2.2.5 becomes apparent. There we mentioned that these small graphene nanodisks can be described as dipole moments with certain polarizability values. By changing the polarizability for these subwavelength (and by subwavelength we mean $\ll \lambda_{\mathrm{SPP}}$) elements, one can control the collective optical response of the structure—One caveat is that the condition $a \ll \lambda_{\mathrm{SPP}}, a = \frac{D}{2}$ must be maintained for validity of dipole moment approximation, otherwise higher multi-poles become significant and must be included in our calculations. By varying size, periodicity and conductivity value of these small patches, we can obtain the desired optical response.

In the following we introduce several scenarios illustrating functions and concepts that might be realized by deliberately engineering graphene conductivity and by following the theoretical framework we developed in chapter 2. We will discuss prospects of having optical elements such as one-atom-thick waveguides, cavities and lenses (chapter 4).

3.1 One-atom-thick waveguide elements

In chapter 2 as an important concept forming one of the foundations for design of flatland metamaterials, we discussed the Fresnel reflection on graphene. We observed that creating a mismatch in the conductivity profile across graphene can result in reflection (near total) of surface plasmon-polaritons in the plane of graphene. We now investigate whether it is possible to devise this feature to design waveguide elements that are only one-atom thick (e.g. different types of waveguides, beam splitters and combiners). Since the guided SPP waves are tightly confined to the graphene surface, such elements can carry wave signals in an ultra-compact volume, showing prospect for design of miniaturized optical devices. Our goal here is to show that it is not out of reach to recreate one-atom-thick variant of almost any element or device available in classic optics on graphene. Our theoretical findings may herald the possibility of contriving a new class of miniaturized photonic circuitry for information processing at the nanoscale [23].

3.1.1 One-atom-thick waveguide

To exploit the reflection mechanism to guiding SPP surface waves, we propose a setting that is one-atom-thick analog of a conventional three-dimensional (3D) metal-insulator-metal (MIM) waveguide (Fig. 3.3).

This 2D waveguide variant consists of three distinct regions within the graphene: two side regions with chemical potential $\mu_{c_2} = 65$ meV ($\sigma_{\mathrm{g},2} = 0.0039 - i0.0324$ mS, where $\sigma_{\mathrm{g2,i}} < 0$), and a middle "ribbon-like" section, with chemical potential $\mu_{c,1} = 150$ meV ($\sigma_{\mathrm{g},1} = 0.0009 + i0.0765$ mS, where $\sigma_{\mathrm{g1,i}} > 0$). To achieve these two different chemical potentials, one may follow any of the approaches discussed earlier in the present work, e.g., designing an uneven profile for the ground plane. We note that since the SPP is highly confined to the graphene, in all our numerical simulations the graphene is assumed to be

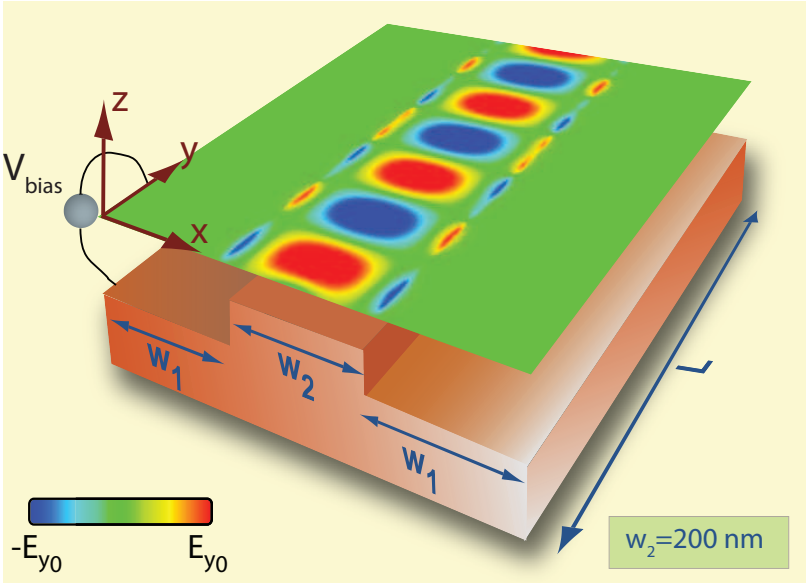

Figure 3.3: Simulation results for E_z (snap shot in time) for an IR-guided wave at $f = 30$ THz along the ribbon-like section of graphene with the chemical potential $\mu_{c,1} = 150$ meV ($L = 560$ nm, $w = w_1 + w_2 + w_3 = 200 + 200 + 200$ nm). Reprinted from Ref. 106 (by permission of the AAAS). [http://www.sciencemag.org/content/332/6035/1291].

free standing in vacuum. We emphasize that the existence of ground plane does not have any role in formation of such highly confined SPP modes as formation of those modes is not due to direct interaction of light with the ground plane; the confined SPP would still exist for a free-standing graphene. The fields of the SPP waves do not even "touch" the ground plane underneath. Therefore, without loss of generality, all the numerical studies are performed for the free-standing graphene with no ground plane present in the simulations. As Fig. 3.3 demonstrates, a guided SPP wave is bounded by the two boundary lines between the graphene segments on the side that have conductivity values different from the middle segment conductivity value.

The mode observed in Fig. 3.3 is the fundamental mode of the waveguide (this mode is symmetric with respect to x), which can be related to the mode of an infinite sheet of graphene(see Fig. 3.4, **A**). Higher-order modes, such as a mode that is anti-symmetric with respect to x, can also be excited in the waveguide (for the antisymmetric mode see Fig. 3.4,

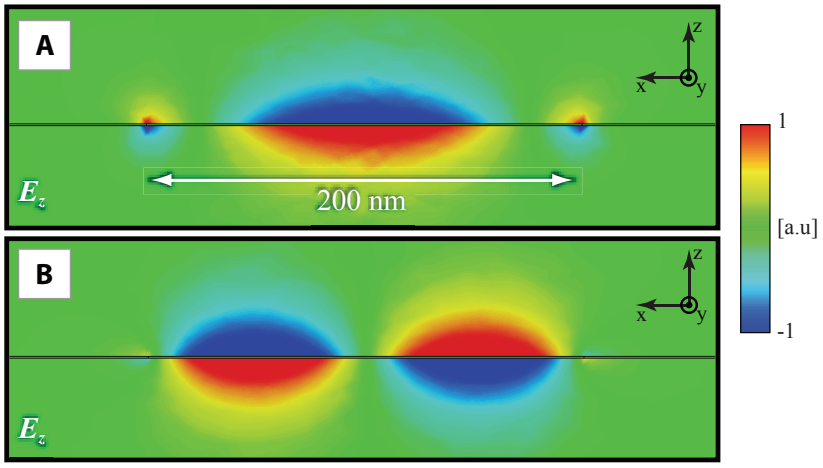

Figure 3.4: **A** Symmetric and **B** antisymmetric modes of graphene nanoribbon waveguide. The snap shot in time of E_z on x-z plane for a graphene nanoribbon waveguide of width $w = 200$ nm.

panel **B**).

For the modes in the middle region the width of the waveguide affects the propagation characteristics (i.e., dispersion relation) and these modes become evanescent below a certain frequency. The lowest-order mode in the middle region might be interpreted as superposition of two infinite sheet mode that propagate at an angle $\theta = \cos^{-1}\left(\frac{\beta_{\text{wg}}}{\beta_\infty}\right)$ with respect to y axis, where β_{wg} and β_∞ respectively denote the propagation constants of transverse magnetic SPP for the ribbon and infinite sheet of graphene. An exact closed form solution for the dispersion relation of the modes in the middle may not be possible[†], however using full-wave numerical simulations, we have obtained the dispersion curve for the fundamental mode, displayed in Fig. 3.5 (in black). As can be seen, and expectedly, the slow-wave factor, defined as $\frac{\Re\{\beta\}}{k_0}$, for this modes is smaller than that of an infinite sheet mode (which is shown in solid blue). This waveguide can also support edge modes around the boundary lines of the ribbon (see discussion in the following).

As a variation to this waveguide, we can consider the same geometry as in Fig. 3.3,

[†]see appendix C for an "electrostatic" formulation of dispersion relation of the plasmon modes

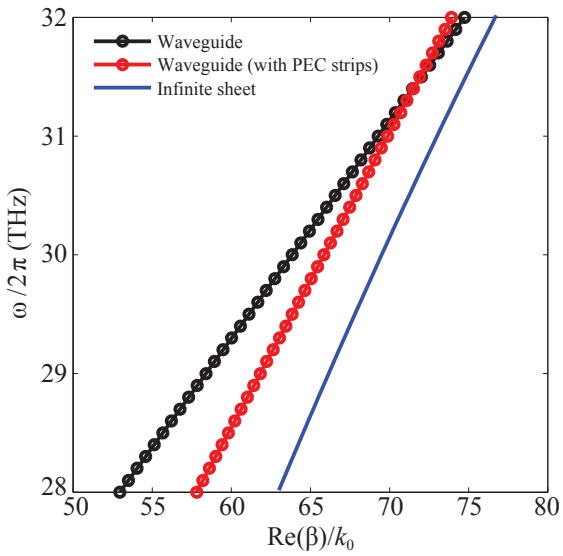

Figure 3.5: Dispersion relation for a graphene nanoribbon waveguide of width w = 200 nm.

however now graphene side regions are replaced with PEC strips. The general form of the modes in the middle remains the same, however the propagation parameters change due to different magnitude and phase of the reflection from the boundaries with PEC strips. Again using numerical simulations we can obtain the dispersion curve of the mode in the middle region (Fig. 3.5, red line). Additionally the PEC strips short the edge modes (discussed in section 2.2.4) around the boundary lines [99].

Finally we note that the waveguide modes in the middle region experience higher losses compared with the infinite sheet mode [71, 99]. The losses can be attributed to the longer propagation path compared with the infinite sheet mode propagation path; for high frequencies for which the propagation angle is smaller, these modes are almost parallel to direction of propagation (y axis) and thus experience lesser amount of loss, whereas for frequencies near cutoff amount of loss is higher, simply because the propagation angle takes its largest values and the propagation path is longer than that of infinite sheet mode [99].

3.1.2 One-atom-thick waveguide using edge modes

As briefly pointed out, in addition to the modes in the middle of the graphene nanoribbon, edge modes could be excited near the boundaries of the ribbon. These modes are related to the edge modes we discussed in section 2.2.4 (see Fig. 2.16 on page 49, where we observed that the boundary line between two semi-infinite sheets of graphene, one with imaginary part of conductivity positive and the other negative[‡], may support edge modes). The edge mode shown in Fig. 2.16 has larger slow-wave factor $\frac{\Re\{\beta\}}{k_0}$ compared with the infinite graphene layer (the guided wavelength associated with this mode is around 61.5 nm) and as pointed earlier, it might be interpreted based on separation of electrons and holes at the boundary region forming a p-n junction [69]. Based on this interpretation, the characteristics of the edge mode depends only on the gradient of the charge density and frequency of operation, thus this mode does not have a cut-off frequency; as we decrease the width of the nanoribbon, the middle region mode becomes evanescent, however the edge modes survive around both boundaries of the ribbon regardless of the the nanoribbon width. Decreasing the width even further results in the two identical edge modes coupling together, hybridizing into two modes. These two new modes have slow-wave factors that are larger and smaller than the original edge modes, i.e., as a result of coupling, the two original edge modes with identical slow-wave factors split into two new edge modes with lower and higher slow-wave factors [16, 71]. However only one of these two modes is cutoff-free, while the other becomes evanescent as the width decreases—in practice there is a narrow range of frequencies (for a fixed width) and a narrow range of widths (for a fixed frequency), for which the mode with lower slow-wave factor is present or distinguishable from the other mode. For high enough frequencies the two modes fall back on to the

[‡]We note that when we refer to two sheets of graphene, we mean two different conductivities, which can be realized within one graphene layer using one of the techniques proposed in chapter 2. So the boundary line is not necessarily formed due two individual strips that are juxtaposed; the boundary line might be a "virtual" line

original edge waves and for low frequencies one becomes evanescent.

We may think of another waveguiding scenario based on coupling of two edge modes by decreasing the width of the nanoribbon. Figure 3.6 depicts such geometry, in which the width of the waveguide is 30 nm (much smaller than cutoff width for middle region modes at 30 THz; based on our simulations the cutoff width for the fundamental mode happens to be around 150 nm). Interestingly for this case the mode is so tightly confined, in both transverse directions (x and z), that even with having the waveguide bent, it remains bounded inside the ribbon and does not leak out. As with the fundamental mode of nanoribbon waveguide, the edge mode experiences higher losses than the original edge mode. However in contrast with the fundamental mode, the attenuation might be due to higher local concentration and hence higher power density in some regions of the ribbon compared with the edge mode of two semi-infinite sheets—the attenuation of the modes in the middle region was attributed to propagation path [99].

3.1.3 One-atom-thick splitter/combiner

Based on the waveguide presented in Fig. 3.3 we can envision an IR splitter (power divider). Figure 3.7 demonstrates such element. The design of this element can be realized by proper choice of conductivity patterns across the single sheet of graphene, generated, for example, by use of uneven ground plane or other techniques. Once an SPP wave is coupled to the closer end (port), the wave propagates along the input waveguide until it reaches the waveguide branches, where it splits into two different paths, and bring considerable portion of the input power to other two ports. Obviously due to reciprocity of the structure, this geometry can also be used as combiner. So if two modes are launched from the farther two ends, the combination can be received in the closer end (port).

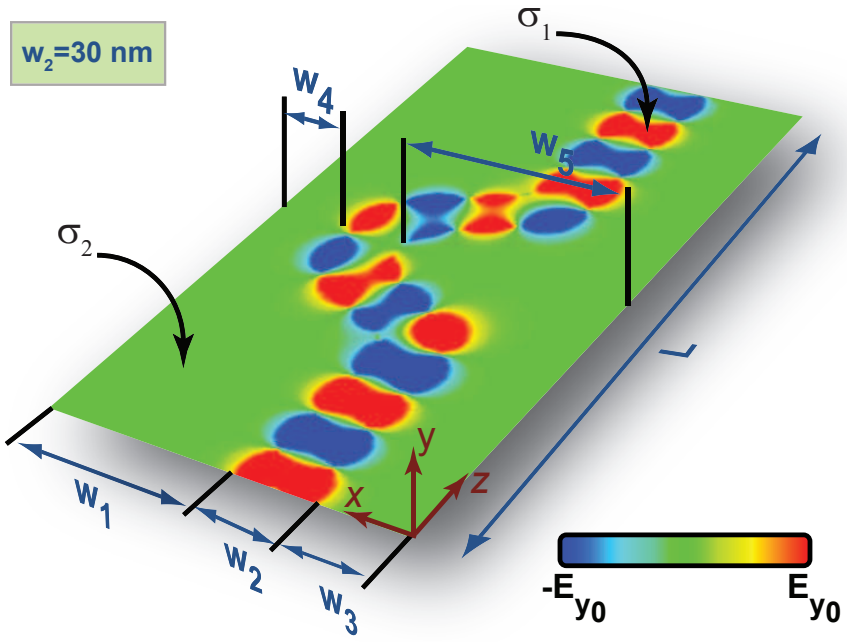

Figure 3.6: Simulation results of E_z (snap shot in time) for an IR guided wave at $f = 30$ THz along a bent ribbon-like section of graphene with the chemical potential μ_{c1}. This ribbon-like path is surrounded by the two other sections of the same sheet of graphene but with a different chemical potential μ_{c2}. The IR signal is clearly guided along this "one-atom-thick ribbon". The computational region has the length $L = 370$ nm and total width $w_1 + w_2 + w_3 = 120 + 30 + 60$ nm while for the bent region $w_4 + w_2 + w_5 = 30 + 30 + 120$ nm. Reprinted from Ref. 107 (by permission of the AAAS). [http://www.sciencemag.org/content/suppl/2011/06/08/332.6035.1291.DC1/Vakil-SOM.pdf].

3.1.4 One-atom-thick optical fiber

As mentioend earlier the waveguide introduced above is analogous to a 3D MIM waveguide. But as is the case with the classic optics, 3D MIM waveguide is not the only geometry that can guide the waves. For example optical fibers are another category of waveguides. So it is natural to ask whether we can have a 2D variant of an optical fiber.

A typical optical fiber is composed of two main dielectric parts: core and cladding[§]. In essence they both can support propagating waves but due to total internal reflection, the light remains bounded inside the "core" (inner region) and does not leak out to the

[§] And of course in practice a jacket to protect the core and cladding.

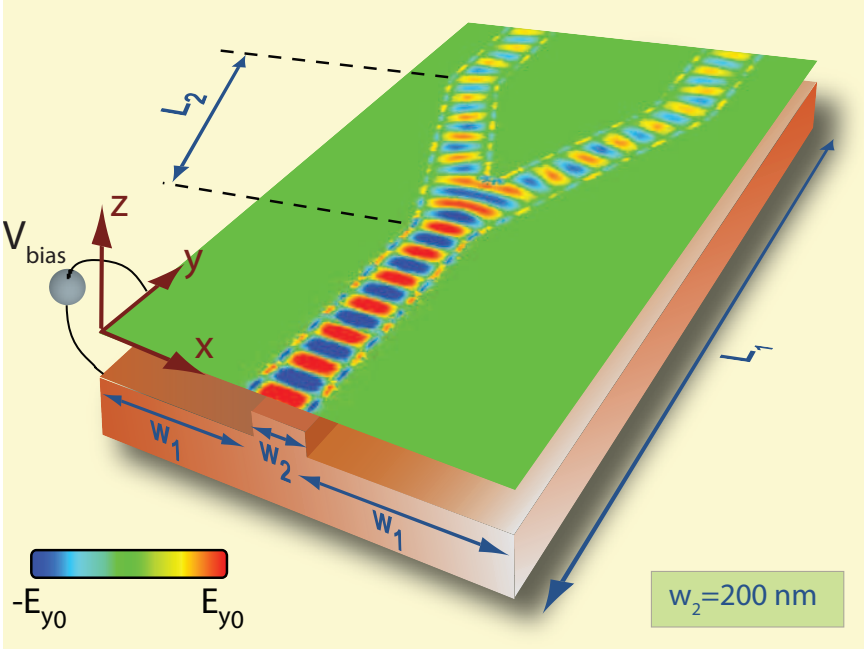

Figure 3.7: Simulation results of E_z (snap shot in time) for an IR splitter. This scenario is Similar to the waveguide case in Fig. 3.3 but the ribbon-like section splits into two paths ($L_1 = 1077$ nm, $L_2 = 560$ nm, $w = w_1 + w_2 + w_3 = 600 + 200 + 600$ nm). The graphene conductivity parameters are similar to those in Fig. 3.3. Reprinted from Ref. 106 (by permission of the AAAS). [http://www.sciencemag.org/content/332/6035/1291].

"cladding" (outer region). We propose a 2D analog of optical fiber in Fig. 3.8.

Figure 3.8 shows full-wave simulation of 2D variant of optical fiber based on graphene. Similar to an optical fiber, which has a high-index medium as THE core and a lower-index medium as the cladding, one can create regions of conductivities such that the middle segment has index larger than the side regions (by index we mean $\frac{\beta_{SPP}}{k_0}$; we will come back to this definition in chapter 4. The simulation results indeed indicate that this geometry guides the SPP mode through the middle region with minimal leakage of the energy to the side regions. One caveat is that similar to an optical fiber the waveguide is not robust to bends and too much bending can result in leakage of the signal to the side regions. But on the positive side, since here the edge mode waves do not exist the amount of loss is limited to that of the mode in the middle, resulting in possibly lower losses for the signal

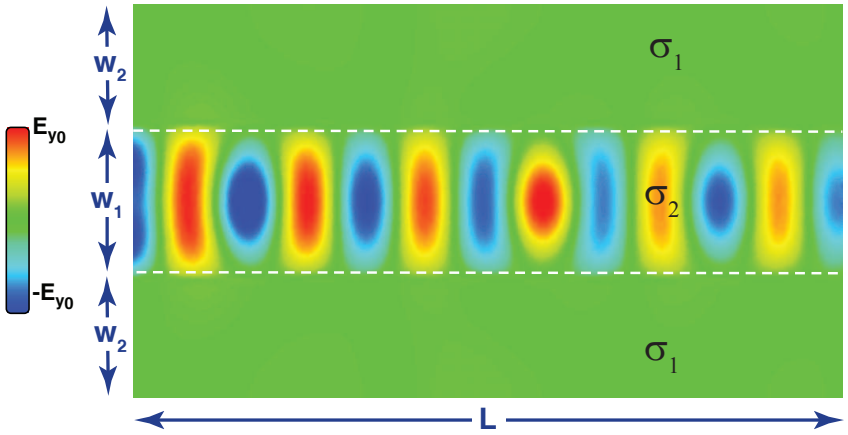

Figure 3.8: Simulation results of E_z (snap shot in time) for an IR guided wave at $f = 30$ THz along a ribbon-like section of graphene with the chemical potential $\mu_{c2} = 150$ meV. This ribbon-like path is surrounded by the two other sections of the same sheet of graphene, but with a different chemical potential $\mu_{c,1} = 300$ meV. Both of these chemical potentials result in positive imaginary part of conductivity, but different values for effective SPP index $\mu_{c2} = 150$ meV results in higher effective index for the "core" region (similar to a 3D fiber for which core has higher SPP index for light). In this simulation, the IR signal is clearly seen to be guided along this "one-atom-thick ribbon". The computational region has the length $L = 1\ \mu m$ and total width $w_2 + w_1 + w_2 = 150 + 200 + 150$ nm. Reprinted from Ref. 107 (by permission of the AAAS). [http://www.sciencemag.org/content/suppl/2011/06/08/332.6035.1291.DC1/Vakil-SOM.pdf].

transmission.

It is worth mentioning that these examples and scenarios are only a few of myriad possibilities that may follow from tailorability and tunability of graphene conductivity. For instance Sounas & Caloz [99] have studied the surface plasmon polartions along a magnetically biased graphene strip. They find that placing a PEC strip along one edge of the graphene strip results in a non-reciprocity in the system, suggesting that wavenumbers are not the same in opposite directions. A non-reciprocal phase shifter is suggested based on this phenomenon. Another interesting prospect for this non-reciprocity in the system is to have a category of waveguides known as one-way-waveguides. In nanophotonics it is always a challenge to suppress back-reflection[¶], which is result of superposition of forward

[¶]Interestingly this problem dates back to the days when engineers were searching for solutions to suppress reflection from an antenna back into a transmission lines.

waves and reflected backward waves. In particular back-reflection could be parasitic for optical signal processing applications that are based on slow-light systems [119]. Having non-reciprocity in the system can be a solution to this problem. As we just mentioned the characteristics of waves are different in opposite direction for the setup proposed by Sounas & Caloz. But what if we operate in a range of frequency, where the forward mode is propagating and the backward is below cutoff? This will result in suppression of the backward wave, preveting formation of back-reflection. This will be a subject of future study on graphene.

As another scenario of waveguiding Christensen et. al [16] propose a linear chain of graphene nanodisks (with $\Im\{\sigma_g\} > 0$) as a waveguide for SPP surface waves. This is indeed 2D analog of a waveguide made up of a linear chain of metallic nanoparticles [3, 11, 87]. The authors also investigate hybridization of plasmon modes in a pair of neighboring aligned nanoribbon waveguides and the propagation characteristics as function of distance of two ribbons. Tuning the distance of two waveguides could be a mechanism for controlling the dispersion of the mode (in some instances this distance can change the dispersion relation of the modes dramatically). Authors' suggest that their proposal can be a platform for low-power optical signal detection.

Having the capability to guide SPPs across graphene, we may think of designing resonant cavities based on graphene waveguides. In the next section we will look at these category of optical elements.

3.2 One-atom-thick cavities

Electrical engineers tend to describe any resonance phenomena using parallel or series circuits of lumped elements (resistor, inductor and capacitor). But why?

This tendency exist because the concept of circuit and associating different behaviors to circuit elements (i.e., dissipative behavior to resistors and reactive behavior to capacitors and inductors) offers a more insightful way of analyzing physical phenomena. As just mentioned to exploit the analogy, the resonance may not necessarily be originating from interaction of actual lumped circuit elements. For instance in microwave engineering, ordinary lumped elements connected through wires do not function as efficient resonators, and to build resonators, engineers resort to structural elements such as waveguides; by enclosing waveguide ends and creating a closed structure that does not radiate, with proper design of geometry, a resonator can be constructed. However circuit theory concepts are still employed in analysis of resonant structures.

Here, as well, we take a similar approach. We design resonant cavities following theoretical concepts developed in chapter 2, section 2.2.4 and then analyze them using circuit theory (especially using the concept of impedance).

Let us start with a simple scenario as depicted in Fig. 3.9. We know that a graphene layer whose imaginary part of conductivity is positive supports TM SPP surface waves. However if the imaginary part is negative these TM waves do not exist. So terminating a graphene layer with $\sigma_{g,i} > 0$, on both ends, with two layers with $\sigma_{g,i} < 0$, would bound the mode to be inside the region sandwiched between two other regions (with negative imaginary parts). But to make the structure resonant at a certain frequency, the cavity dimensions must be designed properly—for example in the 1D geometry of Fig. 3.9 the length of the cavity ℓ should be chosen such that the cavity becomes resonant. In the following section some rules-of-thumbs are proposed for design of resonant cavities.

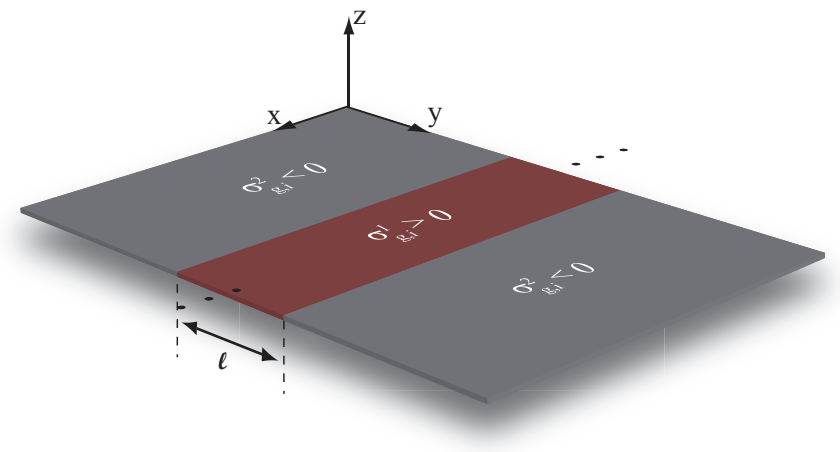

Figure 3.9: (Schematic) 1D one-atom-thick resonant cavity using graphene. The two outer regions have a conductivity whose imaginary part is negative while the region sandwiched between the two has positive imaginary part of conductivity, thus supporting the TM SPP waves. The structure is uniform in x direction ($\partial/\partial x = 0$). The question is "Given that the mode does not leak out to two outer regions, can we choose length ℓ such that the cavity becomes resonant?"

3.2.1 Design of one-atom-thick cavities

1D One-atom-thick resonant cavity

The geometry in Fig. 3.9 may remind us of familiar Fabry-Pérot interferometer in classic optics, which is typically made of two parallel mirrors with high reflectivity. This geometry, as well, is formed of two parallel one-atom-thick regions that can reflect the TM SPP waves considerably as their imaginary parts of conductivity is negative. Since the wave does not enter into these side regions, it has to reflect back. Of course some part of its energy radiates away at the edges, resulting in less than 100% reflection from the boundaries. However as we will see, we can still achieve resonance with imperfect walls (as is the case with an imperfect Fabry-Pérot interferometer).

As we know for a cavity with PEC walls ($\Gamma = -1$, where Γ is reflection from the walls), the resonance condition is simply $\ell = n\frac{\lambda}{2}$ for $n = 1, 2, ...$, where ℓ is length of cavity and λ is the wavelength of the guided mode in the medium between two mirrors. But what if

reflection from the walls of cavity is not -1? For example what if magnitude of reflection coefficient is 1 while the phase angle is not equal to π? It can easily be shown that as long as magnitude of reflection is 1, a resonance condition exists. That condition is

$$\boxed{\ell = \left(n + \frac{\phi}{\pi}\right)\frac{\lambda}{2}}, \tag{3.1}$$

where ϕ is phase angle of the reflection coefficient.

Additionally for reflection coefficients with magnitude less than 1, the resonance condition expressed in Eq. (3.1) holds *approximately* true, if the magnitude of the reflection is close to 1.

We might be able to use the same argument for the 2D version of this cavity. Although the one-atom-thick version is an open structure, as we extensively discussed in previous sections, the SPP waves are very tightly confined to the surface of graphene as if, neglecting radiation losses, all the electromagnetic interaction occurs within and around the sheet of graphene (of course this not exactly true, as we have tails of surface waves decaying in the transverse direction). Assuming validity of this argument, all we need is the reflection coefficient at the boundary lines, where the two outer regions touch the region in between. In section 2.2.4, we developed an approximate technique based on transmission line (TL) analogy to obtain reflection from the edges. Let us choose conductivity of the middle and two side regions, respectively, as $\sigma_{g,2} = 0.0039 - i0.0324$ mS and $\sigma_{g,1} = 0.0009 + i0.0765$ mS. For these values we can use the results reported in third row of table 2.1 on page 53. This is also a good test for accuracy of our TL-based technique. To have resonance at $f = 30$ THz, assuming that the magnitude of the reflection coefficient is close to one, the condition expressed in Eq. (3.1) has to be satisfied for the guided SPP surface wave in the middle segment: $\ell = \left(n + \frac{\phi}{\pi}\right)\frac{\lambda_{SPP}}{2}$ $(n = 1, 2, ...)$. For $n = 1$, we obtain $\ell \approx 0.72\lambda_{SPP}$, which is the minimum length of cavity that leads to resonance. Numerical simulations are used to find maximum value of the electric field in the cavity versus length

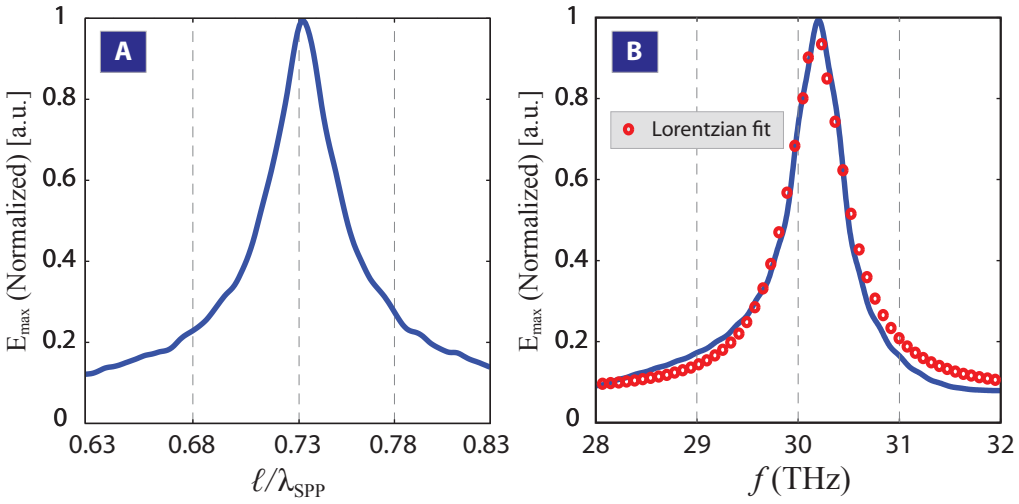

Figure 3.10: A Maximum of magnitude of the electric field at $f = 30$ THz versus length of cavity (normalized to λ_{SPP} of 30 THz SPP). **B** Maximum of magnitude of the electric field versus frequency of operation for $\ell = 0.72\lambda_{SPP}$, where λ_{SPP} is the wavelength of guided SPP at $f = 30$ THz. Also a Lorentzian lineshape is fitted to data–based on the fit the resonance frequency is 30.18 THz while the Lorentzian half-width is ~ 0.37 THz.

of cavity (see Fig. 3.10, **A**). The maximum peak is plotted against length, while keeping frequency and the magnitude of the source fixed to examine our proposed rule-of-thumb $\ell = \left(n + \frac{\phi}{\pi}\right)\frac{\lambda_{SPP}}{2}$. Ideally we would like to see the largest maximum peak of the electric field for $\ell = 0.72\lambda_{SPP}$, where λ_{SPP} is the wavelength of guided SPP at $f = 30$ THz. There is a relatively small discrepancy (less than 2% relative error) between the length predicted by the Eq. (3.1) and the length for which resonance occurs at 30 THz. Although it is subtle, this discrepency might be due to the fact that the magnitude of the reflection coefficient is not exactly 1. Obviously the final goal is to design the cavity so that it resonates at a desired frequency. Figure 3.10, **B** shows the absolute value of the maximum electric field in the cavity versus frequency (the frequency dependence of conductivity of graphene is accounted for by using Kubo formula). As can be seen for length $\ell = 0.72\lambda_{SPP}$, the resonance occurs at around $f = 30.2$ THz, resulting in less than 1% relative error. A Lorentzian curve $\frac{\delta/\pi}{(f-f_0)^2+\delta^2}$ has been fitted to the numerical data. The fitting parameter are

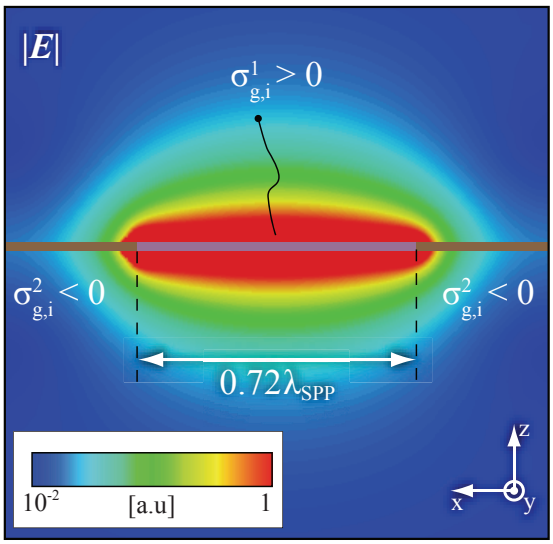

Figure 3.11: Density plot of the magnitude of electric field vector on x-z plane for $\ell = 0.72\lambda_{\text{SPP}}$ at $f = 30.2$ THz (where λ_{SPP} is the wavelength of guided SPP at $f = 30$ THz).

Lorentzian half-width $\delta \approx 0.37$ THz and the resonance frequency $f_0 \approx 30.18$ THz.

Additionally density plot of the magnitude of electric field vector on x-z plane is presented in Fig. 3.11 (we note that the structure is uniform in y-direction). As can be seen the field is enhanced considerably and is tightly confined to the surface of graphene, while bounded in the middle segment.

In summary, it appears that the simple rule-of-thumb proposed for 1D cavities works reasonably well in predicting location of resonance and can be used to find the approximate resonance length for a desired frequency.

2D One-atom-thick resonant cavity

Now let us consider another scenario, where the region of graphene supporting SPP waves ($\sigma_{\text{g,i}} > 0$) is completely surrounded by a region that does not support SPP waves ($\sigma_{\text{g,i}} < 0$)—a 2D scenario. For example consider the circular cavity depicted in Fig. 3.12 (desired resonance frequency is 30 THz and values of conductivity are as in the case of 1D cavity).

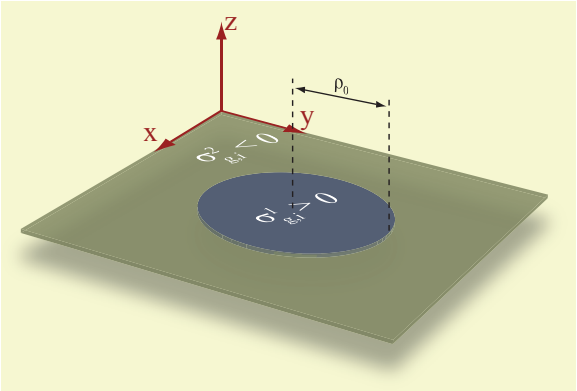

Figure 3.12: (Schematic) 2D one-atom-thick resonant cavity using graphene. The outer region has a conductivity whose imaginary part is negative while the central region has positive imaginary part of conductivity, thus supporting TM SPP waves. Again the question is whether we can find the optimal radius for which this 2D cavity becomes resonant at a desired frequency?

Again the goal is to choose the radius of the cavity so it becomes resonant at a certain frequency. Due to high confinement of the modes, as was the case for the 1D cavity case, we may assume all the electromagnetic interaction occurs within and in the immediate vicinity of the graphene layer, so we might be able to follow the same steps as in the problem of an infinitely long cylindrical cavity. Let us start by writing the transverse component of the electric field in the cavity as

$$E_z = A(k_\rho)\left[E^+_{z,0}H^{(1)}_0(k_\rho\rho) + E^-_{z,0}H^{(2)}_0(k_\rho\rho)\right], \tag{3.2}$$

where term e^{-pz} is dropped since we are very close to the plane of graphene[‖]. In Eq. (3.2) $E^+_{z,0}$ and $E^-_{z,0}$ are electric field amplitudes of the outgoing and incoming radial waves, and $A(k_\rho)$ is a function of k_ρ (determined by boundary condition – see details in section 2.2.3; here for our purpose knowledge of this term is not of concern. The boundary condition at $\rho = \rho_0$ can be written as

$$\frac{E^-_{z,0}H^{(2)}_0(k_\rho\rho)}{E^+_{z,0}H^{(1)}_0(k_\rho\rho)} = \Gamma(\rho = \rho_0), \tag{3.3}$$

[‖] $p = \sqrt{k_\rho^2 - k_0^2}$, as defined in section 2.2, where k_ρ is the radial wavenumber; due to the geometry of the problem, cylindrical coordinate system is chosen.

where $\Gamma(\rho = \rho_0)$ is the reflection coefficient at $\rho = \rho_0$ boundary. Substituting Eq. (3.3) in Eq. (3.2) and removing singularity at origin (which is due to singularity of Hankel functions at origin), the radius ρ_0 has to satisfy following condition

$$\frac{H_0^{(2)}(k_\rho \rho_0)}{H_0^{(1)}(k_\rho \rho_0)} = \Gamma(\rho = \rho_0), \tag{3.4}$$

which can be rewritten as

$$\frac{J_0(k_\rho \rho_0) - iY_0(k_\rho \rho_0)}{J_0(k_\rho \rho_0) + iY_0(k_\rho \rho_0)} = \Gamma(\rho = \rho_0). \tag{3.5}$$

For $\Gamma(\rho = \rho_0) = -1$, Eq. (3.5) simplifies to the faimilar form $J_0(k_\rho \rho_0) = 0$ (this is a well known resonance condition for an infinitely long dielectric cylinder with PEC wall). Let us for a moment assume that k_ρ is real-valued. If so, the right-hand-side (RHS) of Eq. (3.5) has magnitude 1, implying that that as long as the magnitude of reflection from the outer region is 1, the condition expressed in Eqs. (3.4) and (3.5) can be simplified as

$$\boxed{\phi = -2 \tan^{-1} \frac{Y_0(k_\rho \rho_0)}{J_0(k_\rho \rho_0)}}, \tag{3.6}$$

where ϕ is the phase angle of reflection coefficient $\Gamma(\rho = \rho_0)$. This condition still holds *approximately* true for reflection coefficients, whose magnitude is close to 1 (imperfect PEC walls). We again use the value obtained from transmission line technique for $\Gamma(\rho = \rho_0)$ [table 2.1, page 53]. Using the phase angle calculated in table 2.1 in Eq. (3.6) yields $\rho_0 = 0.52\lambda_{\text{SPP}}$ as one condition for resonance (this is of course only one solution of many possible ones). Numerical simulations are used to find maximum value of the electric field (magnitude) in the cavity versus length of the cavity (see Fig. 3.13, **A**).

We examine whether at 30 THz the largest maximum peak of electric field occurs for $\rho_0 = 0.52\lambda_{\text{SPP}}$ (λ_{SPP} is the wavelength of guided SPP at $f = 30$ THz). Again there is a relatively small discrepancy (less than 2% relative error) between the length predicted by the Eq. (3.6) and the length for which actual resonance occurs at 30 THz. Figure 3.10,

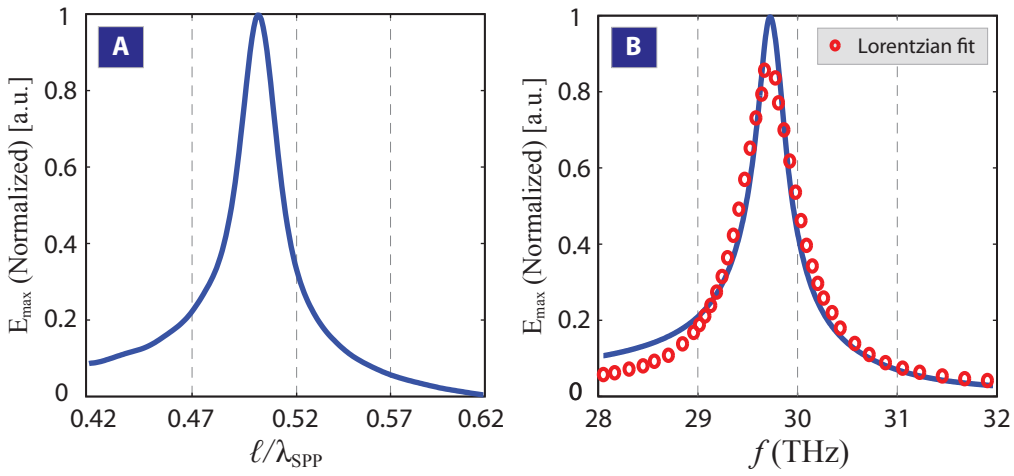

Figure 3.13: **A** Maximum of magnitude of the electric field at $f = 30$ THz versus length of cavity—normalized to λ_{SPP} of 30 THz SPP. **B** Maximum of magnitude of the electric field versus frequency of operation for $\rho_0 = 0.52\lambda_{SPP}$, where λ_{SPP} is the wavelenght of guided SPP at $f = 30$ THz. Also a Lotentzian lineshape is fitted to data–based on the fit the resonance frequency is 29.70 THz while the Lorentzian half-width is ~ 0.30 THz.

B shows the absolute value of the maximum electric field in the cavity versus frequency. As can be seen for length $\rho_0 = 0.52\lambda_{SPP}$, the resonance occurs at around $f = 29.7$ THz, resulting in roughly 1% relative error. Fitting Lorentzian form $\frac{\delta/\pi}{(f-f_0)^2+\delta^2}$ to numerical data yields fitting parameters as $\delta \approx 0.30$ THz (Lorentzian half-width) and $f_0 \approx 29.70$ THz (resonance frequency).

Figure 3.14, **A**, illustrates the magnitude of the *y*-component of electric field on *x*-*z* and *x*-*y* planes, while Fig. 3.14, **B**, shows the magnitude of total electric field on the same planes, suggesting that the electric field is substantially enhanced.

3.2.2 Analysis of one-atom-thick cavities

Of particular interest is to investigate how the resonant cavities introduced in previous sections, enhance the radiation characteristics of an emitter, e.g. atoms, molecules and nanoparticles. Since 2D circular cavity introduced, provides more field confinement com-

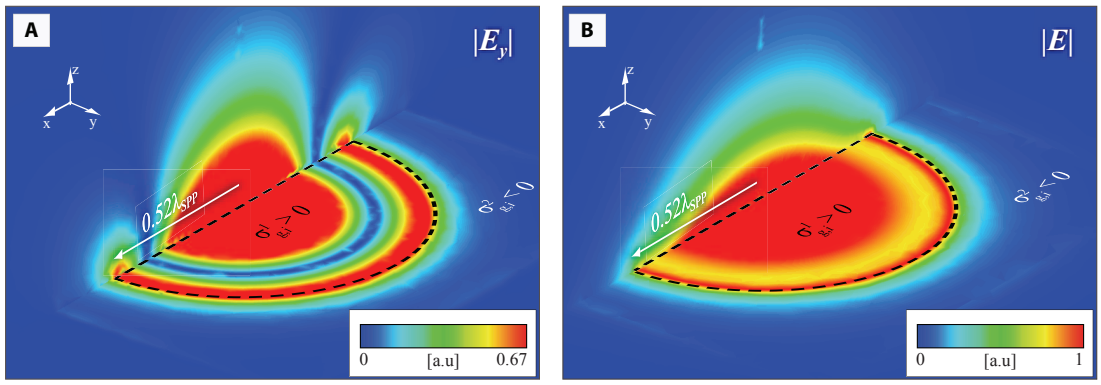

Figure 3.14: A and **B** Density plot of the magnitude of electric field vector and its y-component on x-z and and x-y planes for $\rho = 0.52\lambda_{\mathrm{SPP}}$ at $f = 29.7$ THz (where λ_{SPP} is the wavelength of guided SPP at $f = 30$ THz).

pared with the 1D geometry, here we focus our attention to the former (2D case).

As mentioned in section 2.2.6, *Purcell factor* captures impact of the surrounding environment on spontaneous emission of an emitter (see discussion of Purcell factor on page 63). In this study the emitter is described as a dipole of length L oriented along z-direction. The dipole carries current $I = 1$ A and is located at distance $h \sim 70$ nm above the cavity. To begin our analysis, we simplify Eq. (2.60) as following

$$\mathrm{F_p} = 1 + \frac{6\pi\epsilon_0\omega}{Lk_0^3}\Re\{E_{\mathrm{s,z}}(\mathbf{r}_0)\}, \tag{3.7}$$

in which $E_{\mathrm{s,z}}$ is the z component of the scattered field due to the presence of the cavity. $E_{\mathrm{s,z}}$ can easily be obtained from numerical simulations by subtracting the incident field due to the dipole from total field (we assumed a dipole of length 1 nm in our simulations to mimic an infinitesimal dipole—deeply subwavelength). By evaluating the scattered field at the location of the dipole, we obtain a Purcell factor of as large as approximately 8.2×10^4 for the dipole above the 2D cavity. We note that in this scenario the dipole is located at approximately 70 nm above the cavity. Moving the dipole closer to the graphene sheet can substantially enhance the Purcell effect**. Our findings indicate that for a dipole sitting on

**The effect of distance from graphene is studied extensively in Ref. 43

the graphene layer, in principle, one might achieve Purcell factors as high as 10^7, consistent with Ref. 54. These values are compared with the lower values for Purcell factors of order 10^5 for the 1D cavity.

As we mentioned in section 3.2, to better understand the characteristics of the graphene cavity, we can exploit a circuit analogy. However, the challenge is to describe the cavity using combination of circuit elements such as resistor, inductor and capacitor. Greffet et. al provide such a framework in Ref. 35. Let us briefly discuss their framework and then apply it to our problem.

As we know the time averaged power radiated by a dipole (located at $\mathbf{r}_0$) into the electromagnetic field is [see Eq. (2.61)]

$$P_0 = \frac{1}{2}\Re\{i\omega\mathbf{p}\cdot\mathbf{E}^*(\mathbf{r}_0)\} \tag{3.8}$$

Interestingly the structure of this equation is similar to the familiar form of electrical power $P = \frac{1}{2}\Re\{IV^*\}$ dissipated in a load Z_L with resistance R. Moreover, the electric field is given by $\mathbf{E}(\mathbf{r}_0) = \overleftrightarrow{\mathbf{G}}(\mathbf{r}_0, \mathbf{r}_0; \omega)\cdot\mathbf{p}(\mathbf{r}_0)$, which can be recast as follows [35]

$$\mathbf{E}(\mathbf{r}_0) = \frac{\overleftrightarrow{\mathbf{G}}(\mathbf{r}_0, \mathbf{r}_0; \omega)}{-i\omega}\cdot\left[-i\omega\mathbf{p}(\mathbf{r}_0)\right]. \tag{3.9}$$

This equation also has a familiar structure and is similar to the linear relation between voltage and current $V = ZI$ in the circuit theory. Comparing Eqs. (3.8) and (3.9) with their electrical counterparts and considering that the dipole only has z component ($\mathbf{p} = p_z\hat{\mathbf{z}}$), Greffet et. al have introduced following identifications [35]

$$\boxed{I \leftrightarrow -i\omega p_z(\mathbf{r}_0) \qquad V \leftrightarrow -E_z(\mathbf{r}_0) \qquad Z \leftrightarrow \frac{-iG_{zz}(\mathbf{r}_0, \mathbf{r}_0, \omega)}{\omega}}, \tag{3.10}$$

which enable us to establish the concept of complex impedance $Z = R + iY$ for a dipole (e.g., a quantum emitter). The real part of such impedance accounts for loss (both radiative and dissipative) and is simply expressed as $\Im\{G_{zz}\}/\omega$. Additionally according to our discussion

in section 2.2.6, the spontaneous emission rate (decay rate) is proportional to the imaginary part of Green's function. As discussed in Ref. 35, this similarity constitutes a connection between the decay rate and the resistive part of the impedance just defined ($\gamma \propto R$). Such a connection may provide an insightful way to analyze the cavity under study. For example one can easily re-derive the Purcell factor using the concept of impedance by evaluating the ratio between the resistance of the impedance of the dipole in vicinity of the cavity R to that of the dipole in free-space R_0 ($\mathrm{F_p} = \frac{R}{R_0}$).

The concept of impedance always finds significance when dealing with a collection of interconnected elements. So the question is whether it is possible to define impedance for other elements than the dipole. As introduced in Ref. 35, the same concepts introduced can also be applied to the cavity geometry, meaning that if the modes of the cavity are known, it is also possible to define an impedance for the cavity based on the Green's function of the cavity.

To obtain an expression for the impedance of the cavity, one can expand the Green's tensor in terms of orthonormal modes of the cavity $\mathbf{u}_n$ ($\int_V \mathbf{u}_n \cdot \mathbf{u}_m^* dr^3 = \delta_{nm}$, where δ_{nm} is Kronecker delta) [35]

$$\overleftrightarrow{\mathbf{G}}(\mathbf{r}, \mathbf{r}'; \omega) = \sum_n \frac{\omega^2}{\epsilon_0} \frac{\mathbf{u}_n(\mathbf{r}) \otimes \mathbf{u}_n^*(\mathbf{r}')}{\omega_n^2 \left(1 - \frac{i}{Q}\right) - \omega^2}, \tag{3.11}$$

where $\otimes$ denotes the outer product, ω_n is eigen-frequency associated with mode number n and Q is the quality factor of the cavity. In Eq. (3.11), $\omega_n^2 \left(1 - \frac{i}{Q}\right)$ is the complex frequency accounting for the loss in the cavity. The element lm of matrix representation of equation (3.11) is obtained as

$$G_{lm}(\mathbf{r}, \mathbf{r}'; \omega) = \sum_n \frac{\omega^2}{\epsilon_0} \frac{u_{n,l}(\mathbf{r}) u_{n,m}^*(\mathbf{r}')}{\omega_n^2 \left(1 - \frac{i}{Q}\right) - \omega^2}. \tag{3.12}$$

Since the dipole is oriented in z-direction, as we just saw from Eq. (3.10), we are only interested in evaluating G_{zz}. Assuming we are operating around the resonance frequency

ω_0 (eigenfrequency), contribution from other modes are small and we can write

$$G_{zz}(\mathbf{r}_M, \mathbf{r}_M; \omega) = \frac{\omega^2}{\epsilon_0} \frac{|u_z(\mathbf{r}_M; \omega_0)|^2}{\omega_0^2\left(1 - \frac{i}{Q}\right) - \omega^2}, \tag{3.13}$$

in which r_M is the point where the mode amplitude is maximum and since $u_z(\mathbf{r}_M; \omega_0)$ is a normalized mode of the cavity ($\int_V |\mathbf{u}_n|^2 dr^3 = 1$), the effective mode volume for the cavity is defined as [35]

$$V_{\text{eff}} = \frac{1}{|u_z(\mathbf{r}_M; \omega_0)|^2}, \tag{3.14}$$

which enables us to write Eq. (3.13) as following

$$G_{zz}(\mathbf{r}_M, \mathbf{r}_M; \omega) = \frac{\omega^2}{\epsilon_0} \frac{V_{\text{eff}}^{-1}}{\omega_0^2\left(1 - \frac{i}{Q}\right) - \omega^2}. \tag{3.15}$$

Eqs. (3.10) and (3.15) suggest that the cavity can be regarded as a parallel *RLC* circuit with $R = \frac{Q\omega}{\epsilon_0 V_{\text{eff}} \omega_0^2}$, $L = \frac{1}{\epsilon_0 V_{\text{eff}} \omega_0^2}$ and $C = \epsilon_0 V_{\text{eff}}$ [35]. Finding the ratio of R/R_0 yields the Purcell factor $\text{F}_\text{p} = \frac{3Q\lambda^3}{4\pi^2 V_{\text{eff}}}$ [35]. Mode volume V_{eff} and quality factor Q can be obtained from numerical simulations. Assuming losses are small, using perturbation method, one can evaluate Q from half-power fractional bandwidth $\frac{\Delta f}{f_0}$ of the resonator, where Δf is the distance between frequencies (around f_0), for which the amplitude of the mode drops to $\frac{1}{\sqrt{2}}$ of its maximum at f_0 [86]

$$Q = \frac{f_0}{\Delta f}. \tag{3.16}$$

Using the results from numerical simulations and carrying the calculations through for the 2D graphene cavity, we obtain quality factor of ~ 100 and effective mode volume of 1.6×10^{-22} m^3 ($1.6 \times 10^{-7} \cdot \lambda^3$ for $\lambda = 10\ \mu$m), suggesting that the high Purcell factor is mostly due to very small effective mode volume rather than high quality factor. In fact the quality factor for the 2D cavity is in the same range as for the 1D cavity (~ 80), so the large Purcell effect is mainly the result of the higher mode confinement in 2D case compared with the 1D geometry.

Since in this section we were mostly concerned about analyzing the cavity characteristics, we skip elaborating further on how the concept of impedance can be used to re-derive the decay rate of the dipole in close proximity of the cavity. Greffet et. al offer an elegant treatment of the problem in Ref. 35.

Lastly, on a totally different note, we would like to remark on the possibility of strong coupling between the cavity and the emitter (dipole). In this regime the emitter might enable a strong plasmon-plasmon interaction, resulting in *plasmon blockade*, meaning that for high intensity incident light, which results in strong coupling, average number of plasmons in the cavity do not follow a linear relationship with optical pump intensity (for weak-coupling this relationship is linear regardless of power of optical pump) [65].

3.3 One-atom-thick reflectors

Pursuing our goal to establish graphene as a flatland platform for transformation optics and metamaterials, here inspired by optical mirrors from classic optics, we introduce one-atom-thick reflectors for infrared (IR) SPP surface waves based on graphene. We first study the simple case of one-atom-thick straight line mirror and then show how a one-atom-thick parabolic reflector (mirror) can be envisioned for focusing guided SPP waves on the graphene [109].

3.3.1 One-atom-thick straight line mirror

Let us begin our theoretical study with a simple case: a straight line mirror which is one-atom-thick variant of a plane mirror [109]—we coin term “line mirror” as opposed to plane mirror since the thickness of graphene is extremely small compared to its other dimensions, the boundary between two adjacent sections of a graphene layer is effectively a line rather

than a plane. By studying this relatively simple scenario we can find a better understanding of physics of more complicated reflectors based on graphene. As usual, the simulations are at $f = 30$ THz for a free-standing graphene in air.

Earlier in this work we demonstrated that it is possible to tailor conductivity distribution across graphene such that SPP surface waves reflect from a "boundary line" on a sheet of graphene (section 2.2.4). And as we emphasized this phenomenon is the basic function that many optical elements are built upon. For instance, a plane mirror in classic optics creates an image of a point object behind the plane of mirror. For a plane mirror image is formed at a point where if a straight line were drawn from that point to the object, it would make a right angle with, and is bisected by, the surface of the mirror. However in a typical mirror the image is 180° out of phase with the object and that is because the reflection at the surface of mirror is -1, meaning that the phase angle of reflection is 180°. This phase angle shows up as a phase difference between the object and image.

We would like to address the question that whether we can utilize the concept of image mentioned above to describe the reflection from the boundary. Of course since the phase of reflection coefficient is not the same as the perfect plane mirror, the phase difference between image and object is not 180° anymore but the phase angle of reflection from the boundary (incidentally this is the same as what reported in table 2.1 on page 53).

Figure 3.15, **A**, shows the simulation of the mirror scenario for the SPP surface wave demonstrated on a one-atom-thick graphene layer. The conductivity values of the two segments, calculated from the Kubo formula with $T = 3°$ K and $\Gamma = 0.43$ meV, are, respectively, $\sigma_{g,1} = 0.0009 + i0.0765$ mS and $\sigma_{g,2} = 0.0039 - i0.0324$ mS. The front (closer) half section with $\sigma_{g1,i} > 0$ supports a TM SPP, while the back (farther) half with $\sigma_{g2,i} < 0$ does not. A TM SPP surface wave, with guided wavelength of about 144 nm, and with linear phase front, is generated using superposition of three point sources, located at $\lambda_{SPP}/16$ from the boundary (see Fig. 3.15, **A**). As we said in previous chapter, the reflection of SPP at

this line resembles the Fresnel reflection of a "plane" wave from a planar interface between two media. Here, analogous reflection from a boundary line happens for the SPP across a "one-atom-thick" platform. There is a little radiation loss due to high lateral confinement of SPP surface wave.

To verify that the boundary line between the two segments acts as a "line" mirror, we examine whether the modified version of image theory[††] provides results similar to this setting. We artificially add three "image" point sources (about 90° out of phase with respect to the original sources and at the location of the images; 90° phase difference is dictated by the phase angle of the reflection from the boundary line—obtained from table 2.1 on page 53). The separation between "real" point sources and their "images" is $\lambda_{\mathrm{SPP}}/8$ (twice as distance between the object and mirror).

To conclude that two settings are equivalent, the superposition of the electric fields, in the front segment, due to these two sets of sources – 3 "real" sources and 3 "image" sources – should become similar to the original case. In Fig. 3.15, **B**, the simulation results display the phase of the *y*-component of the electric field in this scenario. The results demonstrate equivalence between two cases (Fig. 3.15, **A** and **B**), suggesting that the boundary between the two segments indeed mimics behavior of a mirror. We note that this mirror is not perfect mirror as the magnitude of reflection from boundary line is not exactly 1, however as long as the magnitude is close to 1, this modified image theory offers a good framework for describing the physics of the problem.

Additionally, for the case where back region has large but positive imaginary part of conductivity, similar results can be obtained (considering the phase angle of reflection coefficient). In the following we study another example that illustrates this possibility. Following our first proposal, one can now envisage several other scenarios.

[††]By modified version, we mean that in the classic image theory for a mirror the object and image are 180° out of phase, while in our scenario this phase difference is the phase angle of the reflection from boundry line.

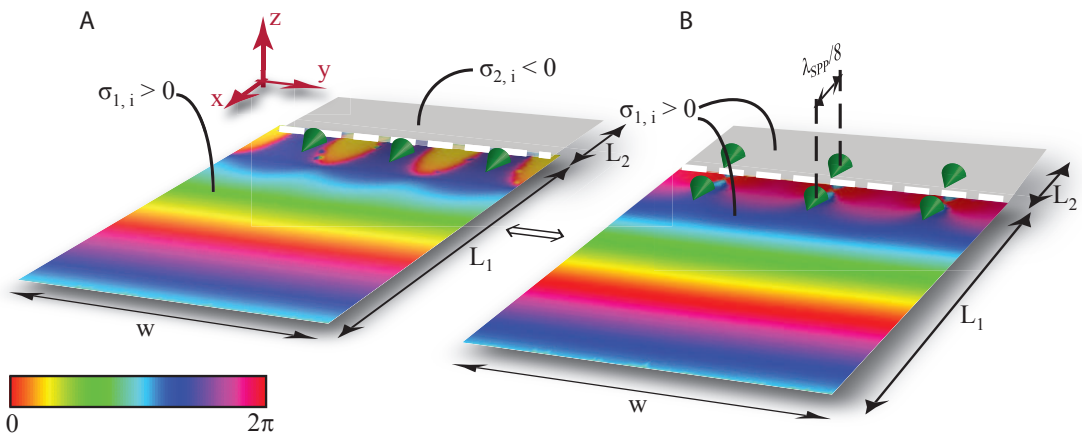

Figure 3.15: A Simulation results showing the phase of z-component of the electric field for the SPP mirror scenario; the back (farther) region imaginary part of conductivity is negative and acts as an effective one-atom-thick straight line "mirror" reflecting an IR SPP guided wave generated from the 3 point sources located at $\lambda_{\rm SPP}/16$ from the edge. The frequency of operation is assumed to be f = 30 THz. **B** the equivalent of the problem in **A** using image theory, where 6 points sources, i.e., 3 "real" point sources and 3 "image" sources have been considered with proper phase difference (L_1 = 300 nm, L_2 = 100 nm, and w = 200 nm). Distance between "real" sources and "image" sources is $\lambda_{\rm SPP}/8$. From Ref. 109. Reprinted with permission from the Elsevier. [http://www.sciencedirect.com/science/article/pii/S0030401812001630].

Consider a 2-dimensional one-atom-thick version of a parabolic mirror for the SPP on a single layer of graphene [109]. Figure 3.16 displays simulation results for such one-atom-thick parabolic mirror, which may be created by patterning the graphene conductivity nonuniformly. The conductivity values of the region in which the guided SPP surface wave is launched (analog of air) and the opaque (mirror) region, at $T = 3^\circ$ K and with Γ = 0.43 meV, are, respectively, $\sigma_{\rm g,1} = 0.0009 + i0.0765$ mS and $\sigma_{\rm g,2} = 0.00001 + i0.00174$ mS. Both sections have $\sigma_{{\rm g},i} > 0$ supporting TM SPP surface wave, however the mirror-like region has a conductivity with relatively large positive imaginary part, which results in an SPP mode that is less confined than the other section. As a result we may observe considerable amount of reflection of SPP at the parabolic mirror line. By proper design of the shape of the boundary (here for example a parabola), one can focus the incoming guided SPP surface wave to a point (for example here in the focus of the parabola). Our

numerical simulation verifies this concept as shown in Fig. 3.16.

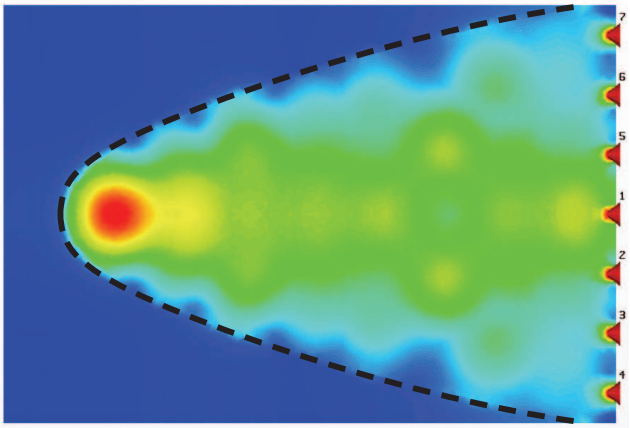

Figure 3.16: Simulation results showing the magnitude of tangential component of the electric field for a one-atom-thick parabolic "mirror" for the SPP focusing an IR SPP guided wave. The frequency of operation is assumed to be at $f = 30$ THz. The structure is 700 nm long and 500 nm wide. From Ref. 109. Reprinted with permission from the Elsevier. [http://www.sciencedirect.com/science/article/pii/S0030401812001630].

In sum, the intuitive image theory discussed here might be useful in analysis and design of graphene-based devices that function based on reflection of SPP surface waves within a sheet of graphene. Also different one-atom-thick mirrors can form building blocks of larger reflective optics systems.

3.4 Transformation optics using graphene

To tame electromagnetic waves we use materials with different optical properties to control and route the corresponding electric or magnetic fields (e.g. optical waveguides, lenses, etc.). For example a bi-convex lens has a refractive index greater than that of air, resulting in refraction of light waves, which due to curved shape of the lens will converge to a point. However, relying only on homogeneous materials as building blocks to produce optical elements is endowed with fundamental limitations in functionality of these elements. It might

be difficult to overcome such limitation by merely relying on homogeneous materials—e.g., beating diffraction limit in a conventional lens. To overcome these limitations we may exploit and design optically inhomogeneous materials. Access to metamaterials and design flexibility that they offer, enable engineering composite structures that might alleviate shortcomings inherent with conventional homogeneous refractive optics. But how can we structure materials to exhibit a desired response? Transformation optics is one solution [83].

Transformation optics (TO) offers recipes to design inhomogeneous materials to direct the electromagnetic waves at will, overcoming limitations of homogeneous optics. Transformation optics deals with design of material properties on a subwavelength scale. From fabrication point of view, although likely achievable, manufacturing materials with such miniature inhomogeneities could be burdensome.

Earlier we mentioned graphene *local* conductivity can be tuned through different methods, e.g., uneven ground plane underneath the substrate holding graphene layer, with a fixed dc voltage applied between the ground plane and the graphene sheet. This proposal can result in a less complicated manufacturing mechanism, as it facilitates the fabrication by transforming the process of creating subwavelength inhomogeneities to simply patterning the ground plane unevenly—which in turn results in the desired conductivity pattern. In this section, by studying two theoretical examples and without going through the technical details of transformation optics, we demonstrate that graphene can be utilized as a new platform for TO.

3.4.1 Luneburg lens with graphene

In our first example we study 2D variant of a Luneburg lens, i.e., one-atom-thick Luneburg lens. The Luneburg lens is a spherical lens, whose refractive index gradually decreases in

radial direction from the center toward the surface (see the left panel in Fig. 3.17, in which the darker regions indicate higher refractive index). Due to gradient refractive index, locus of focal points of this special lens lies on the surface of sphere. The Luneburg lens is aberration-free and can focus light from all directions equally well. It is well known that

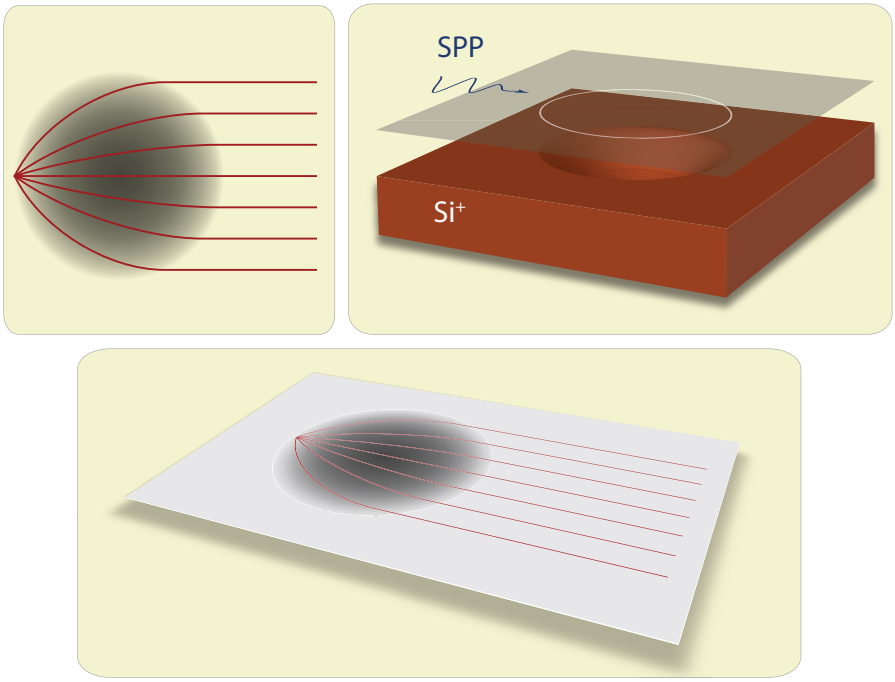

Figure 3.17: (Schematic) Top-left panel illustrates the concept of a spherical Luneburg lens, while top-right panel shows the 2D variant of this concept using graphene. Can we create a nonuniform profile for conductivity across graphene (bottom panel) that results in the same function as in 3D case?

for a spherical Lunebrug lens in a background medium with refractive index n_{bg} the graded refractive index should follow the relation

$$n(r) = n_{\text{bg}} \sqrt{2 - \left(\frac{r}{R}\right)^2}, \tag{3.17}$$

where R is th radius of the lens. As can be seen from Eq. (3.17), for $r = R$, $n = n_{\text{bg}}$ and for $r = 0$, $n = \sqrt{2} n_{\text{bg}}$.

Our goal here is to design conductivity profile of a circular region within graphene layer to function as a Luneburg lens for surface plasmons. In this context we define an effective index for TM surface plasmon-polariton surface waves and try to find an equivalent form for Eq. (3.17). Let us define $n_{\mathrm{SPP}} = \frac{\beta_{\mathrm{SPP}}}{k_0}$. Then according to Eq. (2.13) we have

$$n_{\mathrm{SPP}} = \sqrt{1 - \left(\frac{2}{\sigma_{\mathrm{g}}\eta_0}\right)^2}, \tag{3.18}$$

which can approximately be written as

$$n_{\mathrm{SPP}} \approx \frac{2}{\sigma_{\mathrm{g,i}}\eta_0}, \tag{3.19}$$

Substituting Eq. (3.19) in Eq. (3.17), we obtain a simplified form as

$$\sigma_{\mathrm{g,i}}(r) \approx \sigma_{\mathrm{g,i}}^{\mathrm{out}}\left[2 - \left(\frac{r}{R}\right)^2\right]^{-\frac{1}{2}}, \tag{3.20}$$

where $\sigma_{\mathrm{g,i}}^{\mathrm{out}}$ is the conductivity of the background graphene, within which the Luneburg lens is created. Additionally to perform our numerical simulations, we consider a discretized Luneburg lens, composed of concentric rings with graded conductivities. Discretizing Eq. (3.20) results

$$\sigma_{\mathrm{g,i}}[m] = \sigma_{\mathrm{g,i}}^{\mathrm{out}}\left[2 - \left(\frac{r_m + r_{m-1}}{D}\right)^2\right]^{-\frac{1}{2}}, \tag{3.21}$$

where m corresponds to the number of each ring, with $m = 0$ denoting the center of lens. In our numerical simulation we used 10 segments with graded SPP index following Eq. (3.21). We also define $r[m] = mr[1]$, where $r[1] = 75$ nm. The corresponding chemical potential and imaginary part of conductivity for each segment are reported in table 3.1. Numerical simulations of this free-standing flat Luneburg lens is shown in Fig. 3.18, revealing that the SPP generated from a "point-like" source is evolved into a "collimated beam" of SPP on the graphene, as a conventional 3D Luneburg lens collimates wavefronts generated from a point source into a 3D beam. The diameter of the lens is about 1.5 μm, which is $0.15\lambda_0$—a

Table 3.1: Corresponding chemical potential and imaginary part of conductivity for each segment of 2D Luneburg lens.

m	Chemical potential (μ_c in meV)	$\sigma_{g,i}[m]$ in mS
1	221.0	0.1264
2	222.0	0.1271
3	224.0	0.1284
4	226.7	0.1304
5	231.1	0.1333
6	232.7	0.1372
7	244.0	0.1423
8	255.0	0.1490
9	268.5	0.1581
10	287.0	0.1706

notably subwavelength size. This study suggests that various subwavelength IR devices (e.g., convex and concave lenses) might be possible using graphene.

Transformation optics offers an approach to control the propagation of light by *spatially* varying the optical properties of a material [57, 83, 94]. Because the effective index of the lens is changed gradually rather than abruptly, scattering losses can be reduced. In addition to their imaging functionalities, lenses of any kind are basic elements for optical signal processing (e.g., Fourier transforming). Thus, Luneburg lens based on graphene could find applications in realizing optical signal processing elements such as spatial filters, correlators, and convolvers that are only one-atom-thick [106]. Another advantage of Luneburg lens is the flexibility in control of its focal length that is vital to optical signal processing applications. Lastly, this flat Luneburg lens has prospects for integration with other photonic components.

As a second scenario for transformation optics using graphene, we look at 2D variant of Pendry's super lens proposed in 2000 [81]. The resolution offered by a conventional lens is dictated by wave optics; no conventional lens can recover object features smaller than half of wavelength of the light emanated from an object onto the surface of the lens. This lim-

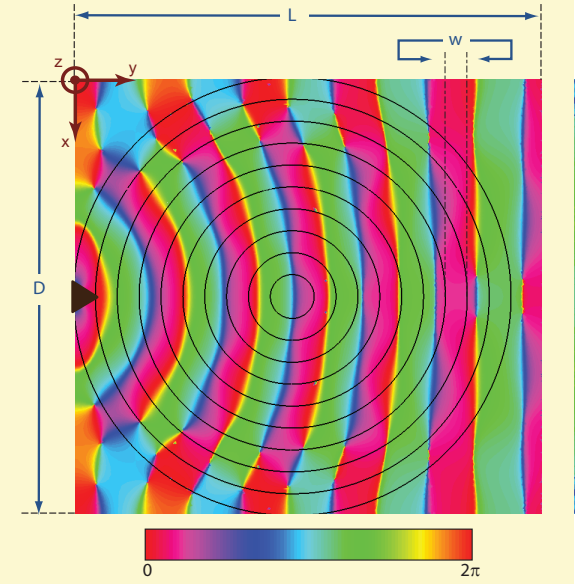

Figure 3.18: One-atom-thick Luneburg lens: Simulation results showing the phase of E_z of the SPP at $f = 30$ THz along the graphene ($D = 1.5\,\mu$m, $w = 75$ nm, $L = 1.6\,\mu$m). Reprinted from Ref. 106 (by permission of the AAAS). [http://www.sciencemag.org/content/332/6035/1291].

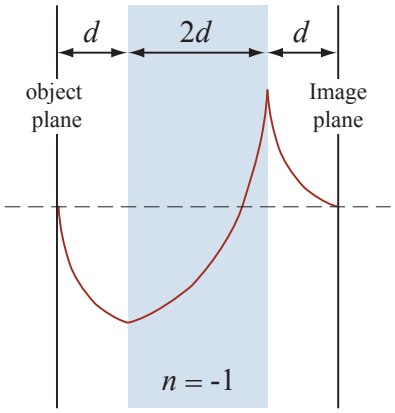

Figure 3.19: Schematic of a superlens; the red lines illustrate tails of the evanescent waves amplified by the slab.

itation of the conventional lens is associated with loss of high spatial Fourier components (choosing axis of the lens as y, these spatial frequency components are k_x and k_z) of the object as they become evanescent and die out before reaching surface of the lens (meaning that for $\left(k_x^2 + k_z^2\right)^{1/2} > \omega c^{-1}$ the wave number in z direction becomes imaginary). Consequently the resolution is limited to $\sim \pi c\omega^{-1} = \lambda/2$ [81]. Pendry's proposal foils this limit,

thanks to features of DNG media. Assuming a slab of negative refractive index material, these missing components can be recovered, if one condition is satisfied: $n = -1$. If this condition holds even the evanescent waves have total transmission through the slab. Also it can be shown in the electrostatic limit $c_0\left(k_x^2 + k_z^2\right)^{1/2} \gg \omega$ a slab of material with $\epsilon_r = -1$, can still act as a superlens for TM-polarized waves radiated from an object placed at distance d from a slab, which is $2d$-thick (the image will be recovered at distance d behind the slab) – see Fig. 3.19. Here we leverage this idea to create a 2D superlens using graphene as we can achieve negative and positive effective permittivity for graphene by changing density of local carriers (effective permittivity was introduced based on conductivity in section 2.2). Although originally superlens idea was not introduced in a transformation optical context, later, transformation optics was employed to interpret the perfect lensing mechanism [56]. As such here we study this case as an example of TO.

To begin consider a similar geometry as in Fig. 3.19 within graphene—i.e., a one-atom-thick strip of width $2d$ and a point source at distance d in front of the strip. The boundary line between the strip and background is virtual; as usual the strip is not necessarily a disintegrated segment from rest of the graphene layer. The contrast in conductivity of the strip and its background can be achieved by proper choice of biases, resulting in required conductivity values. With proper adjustment of the width of the strip and separation between the source and the strip, we can implement an approximate superlensing effect. Simulation results for E_z of SPP surface waves are presented in Fig. 3.20, **A** and **B** (for $f = 30$ THz). Panel **A** shows simulation result for only one point source (the black area in the curve on right displays normalized magnitude of transverse electric field for the point object). As can be seen the proposed superlens yields a shaper image at distance $d = 10$ nm behind the lens – compare red (with superlens) with blue (without superlens). However the real test is to check whether this lens can capture two features of the object that have separation of less than wavelength. To test this we consider a second scenario presented in Fig. 3.20, **B**.

Here two point sources are placed on the object line (which is 10 nm in front of the lens). The separation between these two objects is $s = 55$ nm – at 30 THz the wavelength of guided SPP waves is about 144 nm, so 55 nm is less than $\lambda_{\mathrm{SPP}}/2$. It is worth mentioning

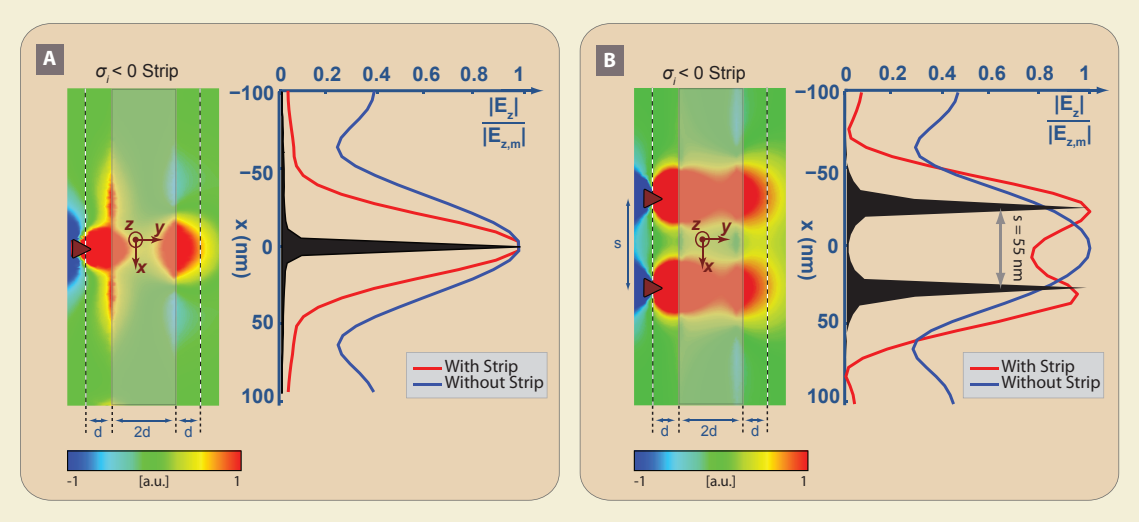

Figure 3.20: Flatland "superlens": Simulation results for E_z of SPP at $f = 30$ THz on the graphene with a subwavelength strip region with conductivity $\sigma_{\mathrm{g},2}$ whose imaginary part is negative, while the rest of graphene has the conductivity $\sigma_{\mathrm{g},1}$ with positive imaginary part. **A** The object–a point source–and image lines are assumed to be, respectively, 10 nm away from the left and right edges of the strip ($w = 2d = 20$ nm). The normalized intensity of E_z at the image line is shown for two cases with and without the strip (Normalization is with respect to their respective peak values). The subwavelength "focusing" is observable as the width of image with superlens is less than without superlens. **B** Now two sources, distanced apart by 55 nm, are placed in front of the lens. Without superlens the image is blurry and the subwavelength features cannot be distinguished, whereas using superlens high spatial frequencies associated with feature sizes less than wavelength can be recovered. Reprinted from Ref. 106 (by permission of the AAAS). [http://www.sciencemag.org/content/332/6035/1291].

that the superlensing can be linked to the existence of edge waves at the two edges of the strip (these edge waves were introduced earlier). The perfect transmission of the evanescent waves might be due to the excitation of two SPP edge waves at the edges of the strip. If two surface plasmons have similar energies, then they can couple efficiently, resulting in a resonance in the system and near perfect transmission. Of course in presence of loss, which is the case here, the transmission cannot be perfect. As such the intensity of light

received on the image line is less than that of object.

The 2D superlens could serve as the basic building block for 2D hyperlens, finding application in transforming deeply subwavelength “input’ field distributions to desired “output” field distributions. This can be of use in optical signal processing and subwavelength imaging within single layer of graphene. Following our work in Ref. 107, there have been proposals for achieving hyperlens using graphene [6, 112].

Chapter 4

Fourier Optics on Graphene

Optical signal processing systems are designed to collect, process and transmit spatial information. For example optical filters perform mathematical operations (e.g., removing some unwanted signal components or enhance others) on spatial signals, just as do electric filters on time signals [33, 34]. One of the basic, yet integral, optical elements used in optical signal processing is the conventional lens. This element provides a simple yet powerful way for obtaining Fourier transform of spatial signals. Optical signal processing based on conventional lenses is not new. However, constructing miniaturized optical systems for processing information at rates higher than the current state-of-the-art call for more than conventional optics, requiring novel ideas in this realm. Here we propose graphene as a new platform for "one-atom-thick" optical signal processing. Our theoretical findings show that by creating a specific pattern of conductivity within a sheet of graphene, one can take spatial Fourier transform of optical signals propagating as SPP waves. There are two advantages in using graphene as far as dimension is concerned: first, by using graphene, one can shrink the thickness of the optical system down to multiples of a carbon atom diameter ($\sim$ 0.34 nm); second, since the optical signals propagate along the graphene in the form

of tightly-confined SPP surface waves with guided wavelength much shorter than the free-space wavelength other two dimensions of the system are also substantially compressed to deep subwavelength scales. These two features can facilitate realization of ultra-compact optical systems. Additionally we previously mentioned that, at least in mid-IR region of the spectrum, quality of SPPs in graphene might be better than in noble metals.

4.1 Lensing mechanism on graphene

The physical process underpinning operation of our proposed one-atom-thick lens is simply borrowed from conventional optics; function of a conventional optical lens in transforming light waves is replicated within graphene. When light is illuminated onto surface of a conventional lens (e.g., when a plane wave is impinging on surface of the lens), farther away from axis of the lens—which has higher refractive index compared with outside medium—phase fronts experience smaller phase differences. The nonuniform phase difference distribution generates curved phase fronts at the output of the lens, coming into a focus point. The same can be visualized for the SPP surface waves within graphene. Consider the geometry depicted in the left panel of Fig. 4.1. This picture illustrates one of the proposed methods to create nonuniform conductivity: using “uneven ground plane” to create a lentil-shaped inhomogeneity in conductivity of a graphene sheet. In this method, highly doped silicon substrate with uneven height profile may serve as the ground plane. Applying a fixed electric bias between the ground plane and graphene results in different values of electric field at different segments of graphene due to differing distance between the flat graphene and the uneven ground plane. This in turn may lead to an inhomogeneous carrier density and consequently inhomogeneous chemical potential distribution, which produces a nonuniform conductivity pattern across graphene layer. We note that to make numerical

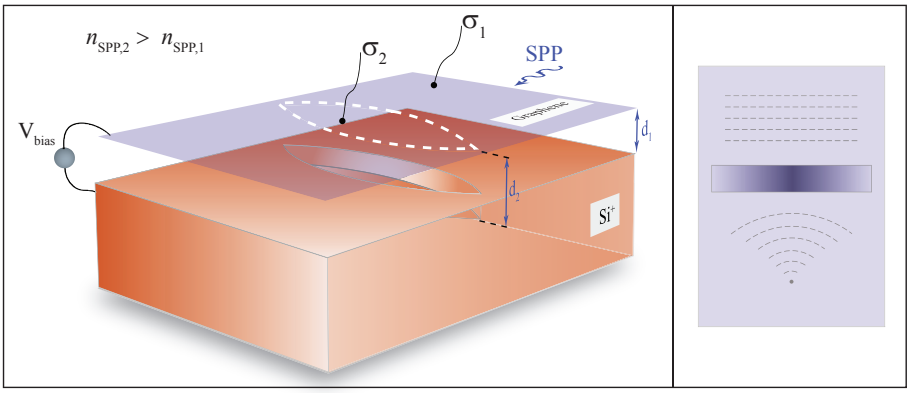

Figure 4.1: Left: Sketch of proposed one-atom-thick lensing system for optical Fourier transforming; geometry consists of a free-standing layer of graphene with inhomogeneous conductivity pattern across. Such inhomogeneity may be achieved by several techniques [106], e.g., by placing a highly doped silicon substrate with uneven height profile as ground plane underneath graphene. Left panel reproduced from Ref. 108 by permission of the American Physical Society. [http://prb.aps.org/abstract/PRB/v85/i7/e075434]. Right: Sketch of a planar gradient index lens similar to the one proposed in Ref. 116.

simulations simpler, we assume that the boundary line between the neighboring regions with different conductivity values is "sharp". In practice, the variation from one region to another is not sharp; however, this will not affect validity of concepts introduced here. Moreover, in practice the distance between the ground plane and graphene is filled with a regular dielectric spacer, e.g. SiO_2. Again for simplicity in our numerical simulations, we assume that graphene is free standing and no spacer or ground plane is present.

In the following we show that this lentil-shaped region with different conductivity (and therefore different equivalent SPP refractive index) acts as a one-atom-thick lens. The shape of the inhomogeneity is similar to cross section of a conventional optical double-convex lens, but given flexibility in tuning graphene conductivity, other shapes can be considered as well. For example a planar gradient index lens can act similar to our proposed lens [116] (Fig. 4.1, right panel).

Fourier transform of an object located at the front focal plane of a conventional double-convex lens is formed at the back focal plane of the lens. Through numerical simulations,

we show that the proposed inhomogeneity within graphene also obtains the Fourier transform of objects located at its front focal line. To show this the following conditions must hold:

(i) The lens must obtain the Fourier transform of a point-like object—which generates circular phase fronts of the SPP on the graphene—placed at its front focal point as linear phase fronts at exit

$$\boxed{\mathcal{F}\{t(x) = \delta(x)\}\Big|_{f_x=\frac{k_x}{2\pi}} = 1}, \tag{4.1}$$

where $\mathcal{F}$ and $t(x)$ denote, respectively, the spatial Fourier transform and transmittance of the object located at the front focal point, and f_x and k_x are spatial frequency and wavenumber, respectively.

(ii) The lens must also obtain the Fourier transform of a uniform object—which generates uniform linear phase fronts—placed at the front focal line, as circular phase fronts converging at back focal point of the lens

$$\boxed{\mathcal{F}\{t(x) = 1\}\Big|_{f_x=\frac{k_x}{2\pi}} = \delta(\frac{k_x}{2\pi})} \tag{4.2}$$

(iii) The lens output must stay invariant, except for a linear phase shift, with respect to shift in the input in the transverse direction; in other words, moving the object along the front focal line must result only in a linear phase variation in the spatial frequency domain at the back focal line. That is

$$\boxed{\mathcal{F}\{t(x) = \delta(x - x_0)\}\Big|_{f_x=\frac{k_x}{2\pi}} = e^{ik_x x_0}} \tag{4.3}$$

(iv) Finally the lens must yield the Fourier transform of an object with a uniform intensity and a linear phase variation located at the front focal line as a converging circular phase fronts to a point shifted along the back focal line

$$\boxed{\mathcal{F}\{t(x) = e^{ik_0 x}\}\Big|_{f_x=\frac{k_x}{2\pi}} = \delta(\frac{k_x}{2\pi} - \frac{k_0}{2\pi})} \tag{4.4}$$

Verifying conditions above, we can assure that the inhomogeneity on the graphene can indeed perform as a lens.

In line with our intuition, our numerical simulations demonstrate that the inhomogeneity indeed exhibits these properties, confirming that the one-atom-thick lens obtains the Fourier transform of the object at its focal line—since everything here occurs on a monolayer, the 2-dimensional object plane of regular optics collapses to a line, hence the descriptor focal "line" [108].

As usual in our simulations, the temperature and the frequency of operation are $T = 3^\circ$ K and $f = 30$ THz, respectively. We emphasize that we could choose any other temperature—e.g., room temperature—in these simulations and still expect similar qualitative effects. The advantage of operating at $T = 3^\circ$ K, however, is that at this temperature the amount of loss in graphene will be much less than the corresponding amount at room temperature. We would like to maintain the chemical potential of the "background" graphene layer at $\mu_c = 150$ meV, corresponding to complex conductivity $\sigma_{g,1} = 0.0009 + i0.07651$ mS. As mentioned in section 2.2.1, for this conductivity, the guided TM SPP has $\Re\{\beta_{SPP,1}\} = 69.34k_0$ and $\Im\{\beta_{SPP,1}\} = 0.71k_0$—equivalently effective SPP index is $n_{SPP} = 69.34$.

As a side note, to create a segment with desired shape and specific conductivity within graphene, the chemical potential must be changed across that segment—for example to create a region that acts as a double-convex one-atom-thick lens, a higher effective index for the SPP surface waves is required. In order for the lens region to have an index larger than the background graphene region ($n_{SPP,1} < n_{SPP,2}$), the ground plane can be patterned such that its distance to the graphene sheet underneath the lens segment (d_2) is larger than its distance to the graphene beneath the background region (d_1). For example, creating a chemical potential $\mu_c = 120$ meV in the lens region, results in complex conductivity $\sigma_{g,2} = 0.0007 + i0.05271$ mS. For this conductivity, $\Re(\beta_{SPP,1}) = 100.61k_0$ and $\Im(\beta_{SPP,1}) = 0.64k_0$

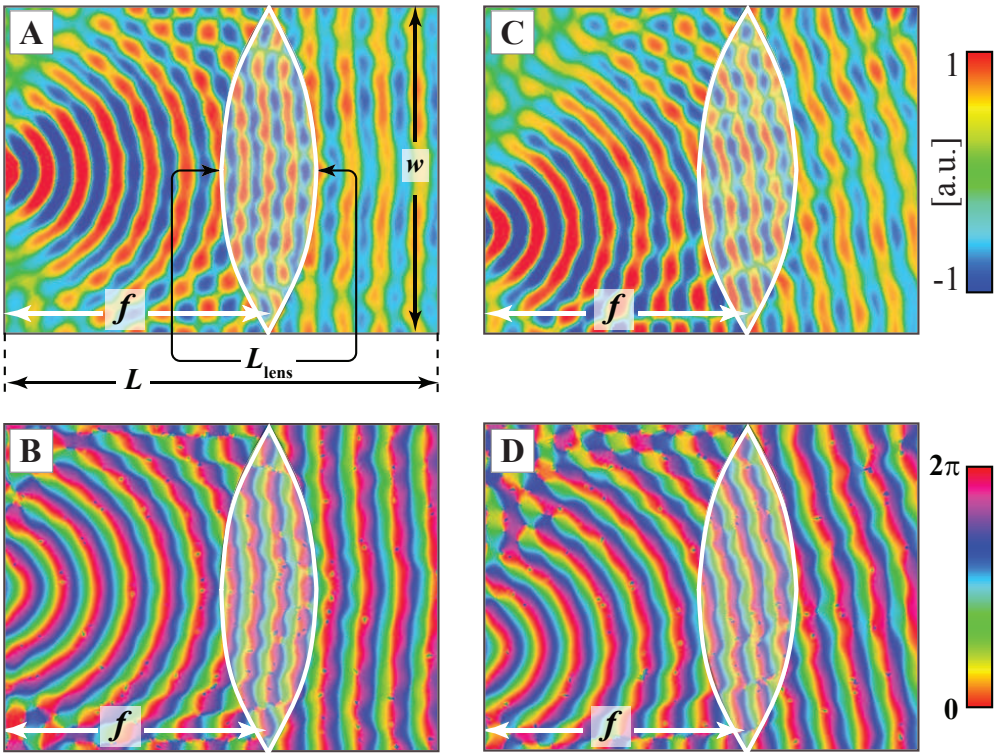

Figure 4.2: Simulation results for Fourier transforming within graphene for the case of point source illumination: **A** Top view of the snap shot in time of transverse component of the electric field of guided SPP wave. The circular waves generated from the point source hit the one-atom-thick lens and exit as an SPP "line" wave. **B** Phase pattern of this SPP wave: this picture demonstrates the "point" to "line" Fourier transformation in **A**. **C** Top view of the snap shot in time of transverse component of the electric field of the SPP wave for case **A**, where the point source is shifted along the left focal line. **D** Phase pattern of the SPP wave in part **C**, showing how the shift in the position of the point source in the left focal line results in the phase shift in the SPP line wave in the exit at the right focal line. Reproduced from Ref. 108 by permission of the American Physical Society. [http://prb.aps.org/abstract/PRB/v85/i7/e075434].

(equivalently $n_{\mathrm{SPP}} = 100.61$). The dimensions for geometries in simulations of Figs. 4.2 and 4.3 are as following: $L = 13.3\lambda_{\mathrm{SPP},1} \approx 1.916\,\mu$m, $L_{\mathrm{lens}} = 2.7\lambda_{\mathrm{SPP},1} = 4\lambda_{\mathrm{SPP},2} \approx 386.8$ nm, and $w = 10\lambda_{\mathrm{SPP},1} \approx 1.444\ \mu$m. Figure 4.2 shows the simulation results for the case in which circular SPP waves generated from a point source, guided along the graphene and impinging onto the double convex lens. Figure 4.2, **A** and **B**, demonstrates the snap shot in time and distribution of the phase of the transverse component of the electric field across

the graphene layer. These results clearly demonstrate that the output of the proposed lens is almost a linear SPP wave at the exit of the lens. So the condition (i) is satisfied. By post processing the simulation results, we estimate the focal length of the proposed lens to be around $f = 4\lambda_{\mathrm{SPP},1} \approx 580.2$ nm. Figure 4.2, **C** and **D**, shows the snap shot in time and phase patterns of the transverse component of the electric field for the case in which the location of point source is shifted down $2\lambda_{\mathrm{SPP},1}$ on the object line. It is clear that the effect of shift appears as a linear phase shift in the spatial frequency domain—on the back focal line. This confirms that condition (iii) holds.

Now we consider the scenario in which the lens is illuminated with a guided SPP surface wave with a linear phase front (see Fig. 4.3). The lens transforms such SPP "line" waves into converging circular SPP waves. Figure 4.3, **A** and **B**, displays the snap shot in time and phase pattern of the transverse component of the electric field across the graphene sheet. We can observe that at the output of lens, circular SPP waves converge at the focal point of the lens. This is a verification of condition (ii). In Fig. 4.3, **C** and **D**, we present the snap shot in time and distribution of the phase of the transverse component of the electric field for the case of oblique incidence. The effect of shift appears as linear phase shift on the image line as the focus moves along the back focal line, asserting that condition (iv) mentioned above holds.

4.2 One-atom-thick 4f system

As an application for the lensing property, in the following we demonstrate a simple example that is analog of an archetypal setup from conventional Fourier optics: a 4f system [34]. A 4f system consists of two identical lenses that are $2f$ apart from each other. This element, which is four focal lengths long, recovers a replica of an object, with even transmittance

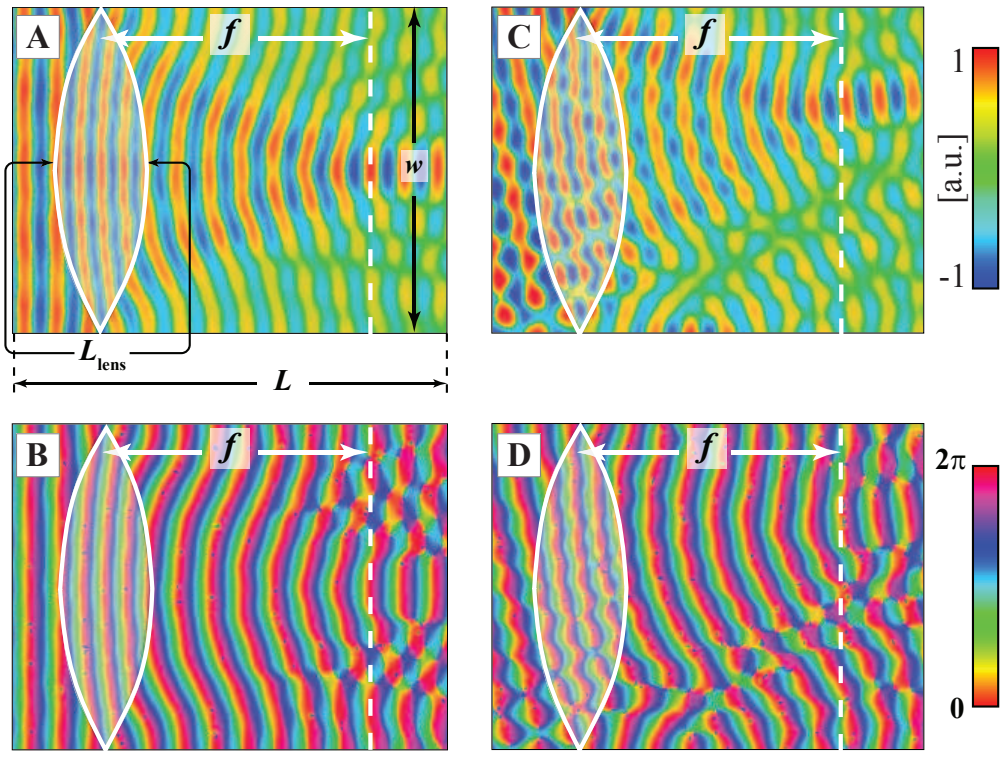

Figure 4.3: Simulation results for the same graphene lens, but for the incident guided SPP "line" wave: **A** Top view of the snap shot in time of transverse component of the electric field of the guided SPP line wave incident on the lens from left, forming an SPP circular wave converging into the focal point on the right. **B** Phase pattern of this SPP wave in **A**. **C** Top view of the snap shot in time of transverse component of the electric field of guided SPP "line" wave oblique incidence. **D** Phase pattern of this guided SPP wave in **C**. This demonstrates the "line" to "point" Fourier transformation and how the phase shift in the SPP line wave on the left can translate into the shift in the location of the focal point on the right. Reproduced from Ref. 108 by permission of the American Physical Society. [http://prb.aps.org/abstract/PRB/v85/i7/e075434].

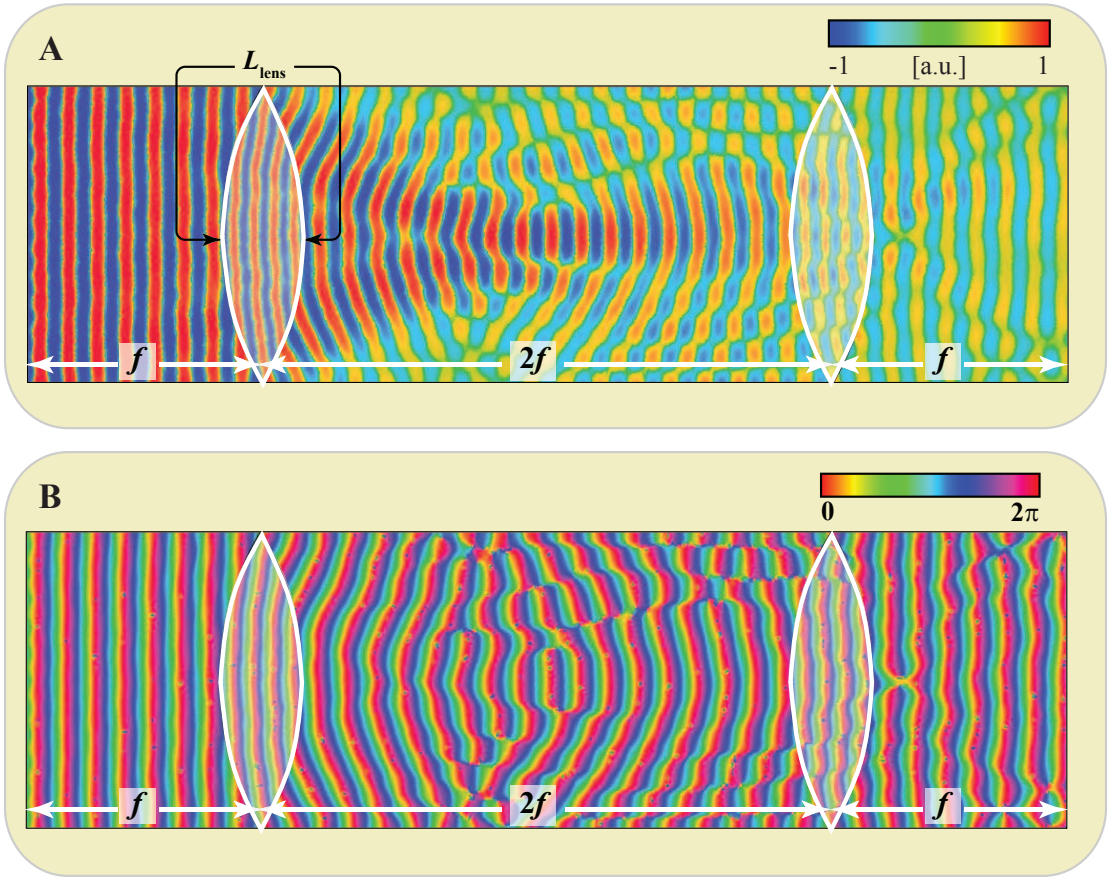

Figure 4.4: A 4f System on graphene: **A** Top view of the snap shot in time of transverse component of the electric field for an SPP "line" wave incidence on the system from left. **B** Phase pattern of this guided SPP wave propagating through the 4f system, clearly showing how this one-atom-thick 4f system transforms the SPP wave from "line" to "point", and then to "line" again. Reproduced from Ref. 108 by permission of the American Physical Society. [http://prb.aps.org/abstract/PRB/v85/i7/e075434].

function of space, placed at one focal length in front of the first lens, at one focal length behind the second lens. This follows from familiar identity $\mathcal{F}\{\mathcal{F}\{t(x)\}\} = t\{-x\}$. The first lens yields the Fourier transform of the object at its back focal line. In turn, the second lens performs another Fourier transform, delivering a duplicate of the object. In Fig. 4.4, the simulation results are presented for a one-atom-thick "4f optical system". The first lens is illuminated with SPP waves with linear phase front. As can be seen, the illuminated waves are approximately recovered at the exit of the second lens.

The 4f system is of particular significance for optical signal processing purposes, since it forms foundation of a "4f correlator", which finds application in implementing the mathematical operations of cross-correlation and convolution [49, 110]. As such a 4f correlator enables a wide variety of image processing operations such as spatial filtering of optical signals [33, 34]. A 4f system is also the basis for functions such as matched filtering and phase-only matched filtering, that are employed in pattern recognition.

In summary our theoretical findings indicate that graphene can be a low-loss platform for Fourier optics functions. Due to tight confinement of the guided SPP wave to the surface of graphene, the entire signal processing occurs effectively in an extremely thin volume around the graphene. As a result, one can envision several parallel graphene sheets closely packed (but far enough apart not to affect the conductivity dispersion of each single sheet) to have parallel and independent optical signal processing. This unique platform could open new vistas in nanoscale and photonic circuitry and massively parallel platforms for high-speed information processing [108].

Chapter 5

Conclusion

5.1 Summary

In this thesis we theoretically and numerically examined prospect of graphene, a monolayer of carbon atoms, as a new platform for one-atom-thick metamaterial and transformation optical devices. Owing to its unusual band structure, graphene exhibits properties unlike that of any conventional material. Although graphene offers various exciting electronic features (which facilitates study of many condensed-matter physics concepts using only a table-top experiment that may not have been possible otherwise), our interest in this work was mainly focused on interaction of electromagnetic waves with this one-atom-thick material and possible applications that could follow in optical and plasmonic design.

In chapter 2, we presented theoretical background underpinning the proposals in chapters 3 and 4. In chapter 2 we first reviewed a theoretical model (Kubo formalism) for graphene conductivity, which was used in our numerical simulations throughout this work. As we mentioned, the results from this formula are in good agreement with experiments by other groups, ensuring validity of physical concepts and discussions presented. The

graphene conductivity is generally a complex quantity and accounts for loss and stored energy in graphene (see the discussion in appendix A). This quantity depends on chemical potential (which is related to carrier concentration in graphene), temperature, frequency and scattering rate (which represents loss). We also observed that the conductivity is related to two transition mechanisms: interband and intraband. The intraband contribution takes a familiar Drude form (free electron gas model) and is dominant below critical frequency $\hbar\omega = 2\mu_c$. Below this critical frequency losses are small, making frequencies lower than this critical value favorable for design of mid-IR metamaterial devices based on graphene. Since CO_2 lasers are available in the range 28 THz to 32 THz, this range was chosen for our studies. In this range of frequency, for temperatures around few Kelvins and for the chemical potentials less than 300 meV losses are relatively small. For frequencies higher than $\hbar\omega = 2\mu_c$, the interband contribution becomes significant and since interband transitions are lossy, these frequencies may not be favorable for realization of optical devices. Then we showed that depending on the sign of imaginary part of the conductivity graphene can support TE and TM surface waves. If imaginary part of the conductivity is positive, graphene can support TM surface plasmon polariton (SPP) surface waves, while TE waves are suppressed. Conversely if the imaginary part of conductivity is negative, the TM modes are not present and instead TE waves are supported. As we studied in detail, TM modes are tightly confined to the surface of graphene, showing potential for small-scale circuitry (in other words they have very large guided wave number $\beta_{\mathrm{SPP,TM}} \gg k_0$). However the TE modes have wave numbers comparable with that of the free-space ($\beta_{\mathrm{SPP,TE}} \sim k_0$), making them less attractive since they cannot be exploited in miniaturized circuits.

In chapter 3, we provided various examples and case studies, suggesting that graphene can indeed be a superb platform for low-dimensional plasmonic metamaterial structures and transformation optical devices. We showed that by creating inhomogeneous patterns across graphene, we can reflect and refract TM SPP surface waves to direct these waves

in desired forms. For example, we offered scenarios in which graphene could be used to build waveguides or beam-splitters by simply varying conductivity nonuniformly across the graphene layer. Several types of waveguides were proposed: a 2D variant of a metal-insulator-metal waveguide, a 2D variant of a optical fiber waveguide and one-atom thick waveguides based on coupling of edge modes. In general two different types of modes could be identified. One set of modes are concentrated in the middle of the graphene, while the other category, the so-called "edge modes", are concentrated around the edges. The edge modes happen to have smaller guided wavelength compared with the middle region modes. Following the waveguiding scenarios presented, resonant cavities based on graphene were studied. It was shown that using a 2D circular cavity one may achieve Purcell factors as high as 10^7 (depending on the distance of the emitter from the cavity), suggesting that graphene might also be an excellent medium for enhanced light-matter interaction. It was noted that this high Purcell factor is largely due to the very small mode volume of the cavity rather than very large quality factor of the cavity. Then we looked at a category of devices based on graphene inspired by conventional mirrors in classic optics. It was argued that a segment within graphene with negative imaginary part of conductivity may act as a mirror for SPP waves. Modified version of conventional image theory was exploited to describe reflection from such region of conductivity. Additionally, we showed that the function of mirror might as well be mimicked by a region of conductivity whose imaginary part is positive but large enough to enable total internal reflection of the TM waves. Mirror is a fundamental element in classic optics and several devices are built upon concept of mirror. Similar devices for SPP surface waves can be envisioned based on graphene, although more compact thanks to atomically thin graphene.

Finally in chapter 4, we introduced the concept of one-atom-thick Fourier optics using graphene. It was illustrated that by creating a region with different effective SPP index (defined as $\frac{\beta_{\text{SPP}}}{k_0}$) that is shaped similar to cross section of a 3D lens, it is possible to achieve

Fourier transforming functions on a single layer of graphene. As it is well known, an optical lens is the building block of optical signal processing systems. This elements is the basis of systems for filtering spatial signals. Our findings can pave the way for realizing high-speed low-dimensional signal processing elements using graphene. In such paradigm, one may envision stacks of graphene layers spaced by dielectric layers – that are only hundreds of nanometer thick – to form a compact optical information processing system that is orders of magnitude smaller than the current state-of-the-art.

5.2 Future directions

The field of graphene metamaterials and transformation optics is in its infancy. In this thesis we talked about several examples of graphene-based metamaterials, however many of these ideas might still be far from implementation and need further detailed studies. Moreover, there are just various directions to pursue on the topics we introduced in this thesis; it is indeed impossible to summarize all of these directions here, but we refer to a subset of them that could be followed in the future.

- **Mid-infrared circuits using graphene**: Interestingly, our first excitement about graphene was whether it can serve as a new platform for optical nano-circuits introduced in Refs. 23 and 25. Although we have had some progresses in this territory (see appendix D for some primary results), this idea is worth investigating and developing further, as it can lead to a new class of circuits that are fast, light and ultra-small.
- **Fourier optics using graphene**: As discussed in chapter 4, graphene is an excellent host for Fourier optics. Although we have laid out the basics and showed thw possibility of Fourier optics functions on graphene, the idea is worth pursuing for further

studies. Expanding ideas in chapter 4, one can achieve larger-scale information processing systems in mid-IR domain that are much faster than the current available systems.

- **Efficient coupling of a plane wave to graphene SPPs**: As pointed out in section 2.2.7, it is of great significance to couple power efficiently to graphene SPPs. Our studies showed that the common techniques in conventional plasmonics are not effective for coupling light with SPP modes (the coupling efficiencies are below 1%). However by proper design of layered nanostructure (such as a plasmonic-dielectric-plasmonic layered nanosphere), one might be able to largely increase the coupling efficiency. This could be subject of further investigation and studies.
- **Inverse scattering problem on graphene and applications for tomography**: Another interesting problem is the study of inverse scattering of SPP from inhomogeneities within graphene. In other words whether it would be possible to retrieve the conductivity of an inhomogeneity by detecting the scattered SPP field due to that entity. This problem particularly is of interest in tomography applications using graphene (see Fig. 5.1). Tomography using graphene can become a powerful technique in imaging non-flat objects (consider an object with uneven height profile) for which direct imaging is not an option, since it may cause damages to the object under study. Additionally this technique is capable of detecting subwavelength features of non-flat objects.

5.3 Final Thoughts

Graphene is indeed intriguing; aside from its 2-dimensionality and low losses in mid-IR, one feature that makes it particularly favorable, is its tunability and the design flexibility

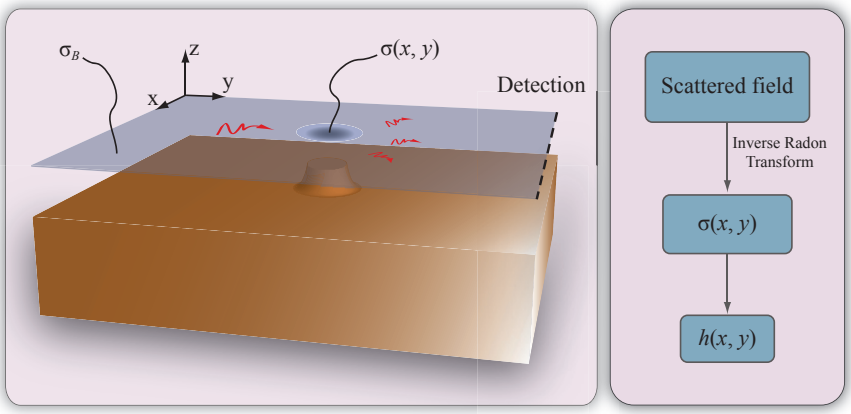

Figure 5.1: Left panel shows a future idea about how graphene may be used to recover the height profile of an unknown bump. On the right panel the steps required to retrieve the profile are illustrated.

it offers. Since graphene's first isolation, prospects for graphene electronics have been extensively studied by condensed matter physicist and engineers. This work and several others suggest that graphene is also an excellent candidate for plasmonics and photonics. Graphene can be the base material for a new generation of circuits that integrate electronics, photonics and plasmonics functionalities.

Appendices

Appendix A

Analogy between Graphene Complex Conductivity and a Parallel RLC Circuit

Here we briefly point out an analogy between graphene complex conductivity model and a parallel RLC circuit (see Fig. A.1). As we know the total admittance of a parallel RLC circuit is written as

$$\begin{aligned} Y &= \frac{1}{-i\omega L} - i\omega C + G \\ &= G + i\left(\omega L - \frac{1}{\omega C}\right) \\ &= G + iB \end{aligned} \tag{A.1}$$

where Y, G and B respectively denote admittance, conductance ($\frac{1}{R}$) and suceptance. Comparing this equation with conductivity of graphene $\sigma = \sigma_{\mathrm{r}} + i\sigma_{\mathrm{i}}$, we can draw a simple analogy: the real part of conductivity represent loss of graphene (similar to conductance of the RLC circuit), while the imaginary part of conductivity relates to the stored energy in graphene (as C and L store energy in different cycles and causing the reactive behavior of the circuit). As a result we might interpret the collective reactive response of the electrons in graphene based on the sign of imaginary part of conductivity. As we have discussed in the main text,

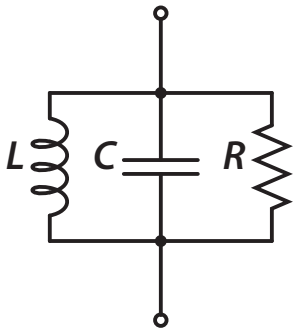

Figure A.1: Analogy between parallel RLC circuit and complex conductivity of graphene.

graphene can attain both positive and negative values of imaginary part. However other conventional 2-dimensional electron gas (2DEG) systems, e.g. GaAs/AlGaAs quantum-well structures, conductivity can only have positive values. We have seen that graphene, due to this feature, can support TE SPP waves, whereas other 2D electron systems do not [67].

Appendix B

Methods for Numerical Simulations

As each simulation required a different treatment and special care, elaborating on subtle details of all simulations in this work is not in the scope of this thesis and probably not in the interest of the readers. As such below we provide the general method of simulations.

We have used commercially available full-wave electromagnetic simulator software, CST Studio Suite™ to perform our numerical simulations [1]. For the purpose of 3D simulations, the thickness of graphene is assumed to be 1 nm, although other extremely small values for this thickness obtain similar results. This technique is based on the derivation of dispersion relation in chapter 2. We assumed 1 nm thickness for graphene and assigned the corresponding permittivity in our simulations according to the derivation shown in section 2.2. As long as the thickness chosen is extremely small compared to the wavelength, the choice of thickness is not essential—for example assume thickness of 0.5 nm for graphene and finding the corresponding permittivity value, yields almost exactly the same simulation results.

Due to the large contrast in the dimensions of the graphene layer, i.e., contrast between thickness and width and between thickness and length, and due to the special form of

the conductivity function of graphene, time-domain method is not appropriate (it usually required a very long run-time and sometimes led to instability) and we chose frequency-domain Finite Element Method (FEM) solver in the CST Studio Suite. This solver solves the problem for a single frequency at a time. For each frequency sample, the system of linear equation is solved by an iterative solver. Adaptive tetrahedral meshing with a minimum feature resolution of 0.5 nm was used in all simulations. A discrete port (a point source which is equivalent of an infinitesimal dipole antenna) or waveguide ports were utilized for the excitation of surface-Plasmon polariton (SPP) wave in the structures. All the simulations reached proper convergence; a residual energy of 10^{-5} of the peak value was reached in the computation region.

To absorb all the energy at the ends of the computational domain and to have approximately zero-reflection boundary on the receiving sides, in all the simulations a technique similar to the well known Salisbury Shield method [29] was implemented (with proper modifications for a TM SPP mode).

Depending on the nature of the problem, perfect magnetic conducting (PMC), perfect electric conducting (PEC) or open boundary conditions were applied to different boundaries, to mimic the two-dimensionality of the geometry.

Appendix C

Universal Plasmon Dispersion for Graphene Nanoribbon Waveguides

Christensen et. al [16] propose an interesting methodology to find a universal dispersion relation for graphene nanoribbons' plasmon modes. In their study they argue that the plasmon modes are of electrostatic nature (due to relatively small size of the waveguide compared with the wavelength of light). As such the modes can be treated as 2D multi-poles. Electrostatic is scale-invariant thus the wavelength does not define an *absolute* length scale. As such the resonances of the nanoribbon system are determined only based on the geometry and optical properties of graphene. By neglecting losses, denoting the width of nanoribbon by W, for each mode, one can define scaling parameter

$$\zeta = \frac{1}{4\pi\epsilon_0}\frac{\Im\{\sigma(\omega)\}}{\omega W}, \tag{C.1}$$

which at resonance peak frequency is independent of W, μ_c and other physical parameters, and only depends on dimensionless quantity $\beta_\infty W$. Then for each mode analytical curves can be extracted (through curve-fitting) for the relation between ζ and $\beta_\infty W$. Such analytical relations with Eq. C.1 can be used to determine the dispersion relation or cutoff condition for SPP modes of graphene. From Eq. C.1 we can also find the width at which

the cutoff occurs

$$W = \frac{\lambda_{\mathrm{SPP}}}{4\pi^2\zeta}, \tag{C.2}$$

which is different from the familiar condition λ_{SPP} for a classical rectangular waveguide. For a detailed discussion of this topic please see [16].

Appendix D

Mid-Infrared nano-circuits using Graphene

The concept of optical nanocircuits using subwavelength plasmonic and conventional dielectric nanoparticles was first proposed by our group in 2005 [25]. Depending on the real part of its permittivity, a nanoparticle can mimic behavior of lumped elements such as inductor and capacitor; a plasmonic nanoparticle whose imaginary part of permittivity is negative can act as an inductor while nanoparticles made up of conventional dielectric ($\Re\{\epsilon\} > 0$) may behave as a capacitor. Additionally any particle with non-zero imaginary part of permittivity can act as a resistor. Field of metamaterial can assist us in realizing desired material properties for these nanoparticles.

Here we propose graphene as a platform for integrated optical nanocircuits. As we have seen throughout this thesis, graphene conductivity can be tuned locally using chemical doping or/and dc electric bias. Also in section 2.2, we introduced an equivalent permittivity based on graphene conductivity. Then we showed that the real part of such equivalent permittivity is linked to the negative of the imaginary part of graphene conductivity

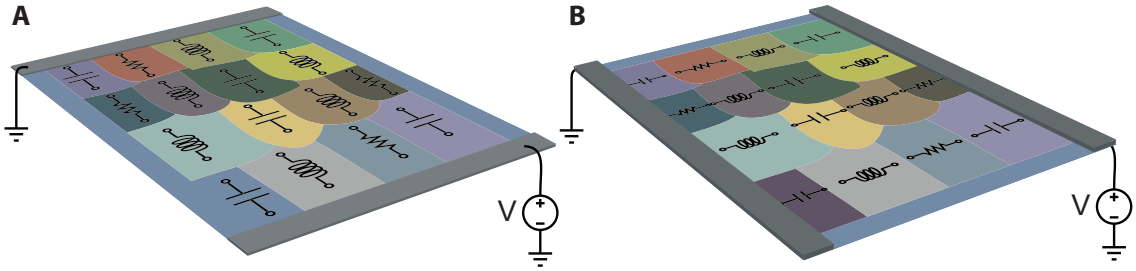

Figure D.1: Optical nanocircuits using graphene: **A** Graphene patches with different conductivity values acting as lumped circuit elements (inductors, capacitors and resistors). **B** Graphene stereo-circuit: depending on the direction of applied current different response can be obtained from the circuit.

($\Re\{\epsilon_{g,eq}\} \propto \Im\{\sigma_g\}$ – see Eq. 2.18a). As such one can hypothesize that a subwavelength* graphene patch, whose imaginary part of conductivity is negative (positive) might act as a capacitor (inductor). Also since $\Im\{\epsilon_{g,eq}\} \propto \Re\{\sigma_g\}$, a graphene patch with non-zero real part of conductivity can also exhibit a resistive behavior. However it is possible to have these patches within one single layer—a single layer's conductivity can be tuned locally so that different locations (patches) possess different values of conductivity (and different signs) (see Fig. D.1, **A**).

In addition the notion of "stereo-circuitry" might be realized using a graphene layer, meaning that depending on the direction of current applied to the circuit, a different response can be expected (Fig. D.1, **A** versus **B**).

The concept of graphene optical nanocircuit is yet to be explored further, but here we present some primary results that show prospect for this type of circuitry. We carry out our simulations for frequencies around 14 THz (13 – 15 THz). Since here we are only interested in showing the concepts, the particular choice of frequency is not of significance.

Consider the geometry illustrated in Fig. D.1. The middle region is a graphene patch with positive imaginary part of conductivity, while the two outer regions next to the middle

*SPP wavelength

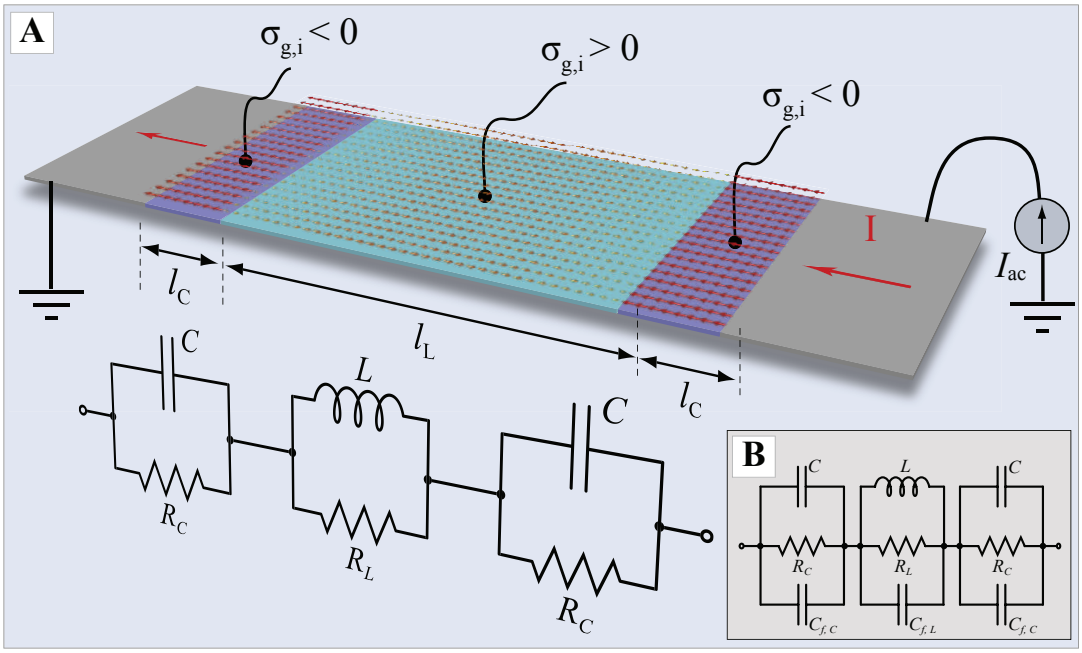

Figure D.2: A series graphene nano-circuit: **A** The geometry of a series graphene nanocircuit; as shown in the bottom part the middle region behaves as an inductor while the two outer regions to the middle region act as capacitors; the material losses of each segment is described as resistor $\Re\{\sigma_g\} \neq 0$ (also a snapshot in time of the electric field vector is shown, indicating that the electric field direction flips upon entering from one patch to another). **B** illustrates the circuit model of the same geometry, however effect of fringe electric field are described as capacitance in parallel with the original elements.

region have negative imaginary part of conductivity. The length of the middle region and outer regions are, respectively, 69.2 nm and 15.4 nm—overall length of circuit is 100 nm, which is much less than the SPP wavelength at 14 THz (~ 775 nm), so the circuit can be deemed as a lumped circuit. This circuit can be fed by two electrodes that are sketched schematically in the figure (note that the structure is 2-dimensional in the lateral direction).

This geometry can be regarded as a series combination of two capacitors and one inductor each shunt with a resistor as shown in Fig. D.1, **A**. Also Fig. D.1, **B**, shows a more sophisticated circuit model for the geometry, describing the effect of fringe electric fields by use of capacitors in parallel with each element.

The total impedance of the circuit is defined as following

$$Z = \frac{V}{I} = -\frac{\int_l \mathbf{E} \cdot d\mathbf{l}}{\oint_S \epsilon \mathbf{E} \cdot d\mathbf{s}}, \tag{D.1}$$

in which l is a line through the circuit and S is a mathematical surface cutting cross section of the circuit [†]. The electric field can be obtained from full-wave numerical simulations. Using the results obtained from simulations, we can find the total impedance of the circuit as a function of frequency (as shown in Fig. D.3). However to verify validity of the equivalent circuit proposed, we have to evaluate the capacitance, inductance and resistance of each lumped element of the equivalent circuit and examine whether the circuit combination proposed yields a similar impedance as the simulations. The admittance of these segments can be obtained using following expressions

$$Y_C = \frac{\sigma_{\mathrm{g},C}}{W} l_C - i\omega C_{\mathrm{f},C}, \quad Y_L = \frac{\sigma_{\mathrm{g},L}}{W} l_L - i\omega C_{\mathrm{f},L}, \tag{D.2}$$

where $\sigma_{\mathrm{g},C}$ and $\sigma_{\mathrm{g},L}$ denote the complex conductivity of the capacitive and inductive segments and W is the width of the circuit (w = 35 nm). The total impedance then is

$$Z = \frac{2}{Y_C} + \frac{1}{Y_L}. \tag{D.3}$$

In Eq. D.2, $C_{\mathrm{f},L}$ and $C_{\mathrm{f},C}$ are equivalent fringe capacitances that capture the effect of the electric field fringe. To compute these fringe capacitances, we assumed that the fringe fields can be associated to two cylindrical wires at two ends of each segment with diameter D equal to the thickness of graphene (t). Based on this idea and the fact that the capacitance of a two-wire transmission line follows the form

$$C_f = \pi\epsilon_0 \frac{W}{\cosh^{-1}\left(\frac{l}{D}\right)}, \tag{D.4}$$

[†]This mathematical surface crosses the middle of that graphene sheet and is extended such that the fringe field lines cross this surface

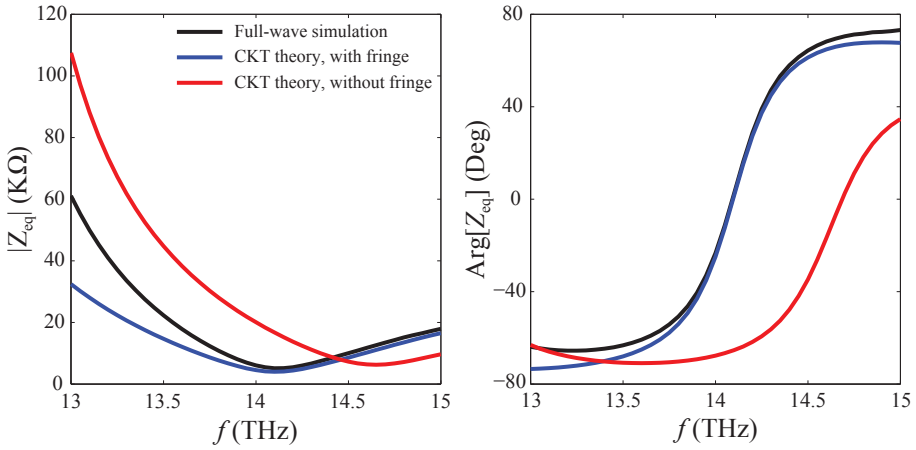

Figure D.3: Series graphene circuit impedance based on numerical simulations and circuit theory.

we can compute the fringe capacitance parallel with each segment. Figure D.3 also shows the impedance of the circuit based on the proposed circuit model (with and without the fringe capacitances). As clearly can be seen the impedance based on the circuit model (with fringe capacitances) mimics very closely the impedance obtained from the simulations (using Eq. D.1).

In summary here we show-cased a graphene-based series circuit, which can be analyzed using conventional circuit theory. Although this study is in its early stage, it may herald a potential for integrated optical nanocircuits, thanks to tunability of graphene conductivity.

Appendix E

Matlab Code for Calculation of Complex Conductivity of Graphene

This is a piece of code written in Matlab that we used to calculate the complex conductivity of graphene using Kubo Formula.

```
%%%%%%%%%%%%%%%%%%%%%%%%%%%%%%%%%%%%%%%%%%%%%%%%%%%%%%%%%%%%%%%%%%%%%%%%%%%%
%                                                                             %
%  Calculation of Conductivity of Graphene using Kubo Formula  %
%                      Author: Ashkan Vakil                                   %
%                                                                             %
%%%%%%%%%%%%%%%%%%%%%%%%%%%%%%%%%%%%%%%%%%%%%%%%%%%%%%%%%%%%%%%%%%%%%%%%%%%%
clc
clear;

j = sqrt(-1);
e = 1.6e-19;
K_B = 1.3806503e-23;
T = 3;
hb = (6.626e-34)/(2*pi);
% tau = 3e-12; % form GW Hanson paper
% tau = .64e-12;  % Soljacic paper
% gamma = 1/(2*tau);
gamma = 0.65460252158e12; % Gusynin J. Phys.: Cond. Mat.
sigma_min = 6.085e-5;
vf = 10^6;

w = pi*2e12*linspace(5,400,200); % CO2 lasers are this range
```

```
m = length(w);
mu_c = 1.6e-19*[.15];
n = length(mu_c);
mu_ct = repmat(mu_c,m,1); % generating the matrix for chemical potential
wt = repmat(transpose(w),1,n); % generating the matrix forfrequency

sigma_d_intra = ...
   -j*((e^2*K_B*T)./(pi*hb^2*(wt-j*2*gamma))).*((mu_ct)/(K_B*T)...
    +2*log(exp(-mu_ct/(K_B*T))+1)); %intraband term
sigma_d_inter = zeros(m,n); % interband term variable definition

eps = 1.6e-19*linspace(0,10,600000);
q = length(eps);

% Interband term calculations
for i = 1:n
    muc = mu_c(i);
    f_d_meps = 1./(1+exp((-eps-muc)/(K_B*T)));
    f_d_peps = 1./(1+exp((eps-muc)/(K_B*T)));
    for k = 1:m
        sigma_d_inter(k,i) = ...
           trapz(eps,-(j*e^2*(w(k)-j*2*gamma)/(pi*hb^2))...
            *(f_d_meps-f_d_peps)./((w(k)-j*2*gamma)^2-4*(eps/hb).^2));
    end
end

sigma_tot = sigma_d_inter+sigma_d_intra; % total conductivity
C = {'k','r','b','c','g','m','y'};
p1 = zeros(1,n);
pp1 = zeros(1,n);
s1 = cell(1, n);
p2 = zeros(1,n);
pp2 = zeros(1,n);
s2 = cell(1, n);

%%%%%%%%%%%%%%%%%%%%%%%%%%%%%%%%%%%%%%%%%%%%%%%%%%%%%%%%%%%%%%%%%%%%%%%%%%%%%%%%
%%%%%%%%%%%%%%%%%%%%%%%%%%%%%%%%%%%%%%%%%%%%%%%%%%%%%%%%%%%%%%%%%%%%%%%%%%%%%%%%
figure(1)
subplot(2,1,1)
for i = 1:n
    hold on
    p1(i) = ...
       plot(1e-12*w/2/pi,(transpose(real((sigma_d_inter(:,i)))))/...
        (e^2/hb/4),'Color', C{i},'Linewidth',2);hold on
    pp1(i) = ...
       plot(1e-12*w/2/pi,(transpose(real((sigma_d_intra(:,i)))))/...
        (e^2/hb/4),'Color', ...
           C{i},'Linewidth',2,'Linestyle','-.');hold on
    s1{i} = sprintf('mu_{c,%d} = %d meV',i,1e3*mu_c(i)/(1.6e-19));
end
```

```
ind = 1:n;
% axis square
box on
xlabel('f (THZ)','fontsize',20,'fontweight','b');
ylabel('Re(\sigma)','fontsize',20,'fontweight','b');
legend(p1(ind), s1{ind});

%%%%%%%%%%%%%%%%%%%%%%%%%%%%%%%%%%%%%%%%%%%%%%%%%%%%%%%%%%%%%%%%%%%%%%%%%%%%%%%
%figure(2)

subplot(2,1,2)
hold on
for i = 1:n
    hold on
    p2(i) = ...
       plot(1e-12*w/2/pi,-(transpose(imag((sigma_d_inter(:,i))))/...
        (e^2/hb/4),'Color', C{i},'Linewidth',2);hold on
    pp2(i) = ...
       plot(1e-12*w/2/pi,-(transpose(imag((sigma_d_intra(:,i))))/...
        (e^2/hb/4),'Color', ...
           C{i},'Linewidth',2,'Linestyle','-.');hold on
    s2{i} = sprintf('mu_{c,%d} = %d meV',i,1e3*mu_c(i)/(1.6e-19));
end
% axis square
box on
xlabel('f (THZ)','fontsize',20,'fontweight','b');
ylabel('Im(\sigma)','fontsize',20,'fontweight','b');
% legend(p2(ind), s2{ind});
```

Bibliography

[1] CST Microwave Studio (from CST Studio Suite 2012). http://www.cst.com/.

[2] A. Alú and N. Engheta. Optical nanotransmission lines: synthesis of planar left-handed metamaterials in the infrared and visible regimes. *Journal of the Optical Society of America B*, 23(571), 2006.

[3] A. Alú and N. Engheta. Theory of linear chains of metamaterial/plasmonic particles as subdiffraction optical nanotransmission lines. *Physical Review B*, 74(205436), 2006.

[4] A. Alú and N. Engheta. Three-dimensional nanotransmission lines at optical frequencies: A recipe for broadband negative-refraction optical metamaterials. *Physical Review B*, 75(0243304), 2007.

[5] D. R. Anderson. Graphene-based long-wave infrared tm surface plasmon modulator. *Journal of Optical Society of America B*, 27(818), 2010.

[6] A. Andryieuski and A. V. Lavrinenko. Graphene hyperlens for terahertz radiation. *Physical Review B*, 86(121108), 2012.

[7] C. A. Balanis. *Advanced Engineering Electromagnetics*. John Wiley & Sons, New York, 1989.

[8] Q. Bao and K. P. Loh. Graphene photonics, plasmonics, and broadband optoelectronic devices. *ACS Nano*, 6(5):3677–3694, 2012.

[9] Q. Bao, H. Zhang, B. Wang, Z. Ni, C. H. Y. X. Lim, Y. Wang, D. Y. Tang, and K. P. Loh. Broadband graphene polarizer. *Nature Photonics*, 5:411–415, 2011.

[10] W. L. Barnes, A. Dereux, and T. W. Ebbesen. Surface plasmon subwavelength optics. *Nature*, 424(824), 2003.

[11] M. L. Brongersma, J. W. Hartman, and H. A. Atwater. Electromagnetic energy transfer and switching in nanoparticle chain arrays below the diffraction limit. *Physical Review B*, 62(24), 2000.

[12] W. Cai and V. Shalaev. *Optical Metamaterials: Fundamentals and Applications*. Springer, New York, 2010.

[13] V. V. Cheianov, V. Falko, and B. L. Altshuler. The focusing of electron flow and a veselago lens in graphene p-n junctions. *Science*, 315(1252), 2007.

[14] J. Chen, M. Badioli, P. Alonso-González, S. Thongrattanasiri, F. Huth, J. Osmond, M. Spasenović, A. Centeno, A. Pesquera, P. Godignon, A. Z. Elorza, N. Camara, F. J. García de Abajo, R. Hillenbrand, and F. H. L. Koppens. Optical nano-imaging of gate-tunable graphene plasmons. *Nature*, 487:77–81, 2012.

[15] P-Y. Chen and A. Alú. Atomically thin surface cloak using graphene monolayers. *ACS Nano*, 5(7), 2011.

[16] J. Christensen, A. Manjavacas, S. Thongrattanasiri, F. H. L. Koppens, and F. J. García de Abajo. Graphene plasmon waveguiding and hybridization in individual and paired nanoribbons. *ACS Nano*, 6(1), 2011.

[17] R. E. Collin. *Foundations for Microwave Engineering*. John Wiley & Sons, New York, 2000.

[18] I. Crassee1, J. Levallois, A. L. Walter, M. Ostler, A. Bostwick, E. Rotenberg, T. Seyller, D. van der Marel1, and A. B. Kuzmenko. Giant faraday rotation in single- and multilayer graphene. *Nature Physics*, 7(1816), 2010.

[19] József Cserti, András Pályi, and Csaba Péterfalvi. Caustics due to a negative refractive index in circular graphene p-n junctions. *Physical Review Letters*, 99(246801), 2007.

[20] R. Dehbashi, D. Fathi, S. Mohajerzadeh, and B. Forouzandeh. Equivalent left-handed/right-handed metamaterial's circuit model for the massless dirac fermions with negative refraction. *IEEE Journal of Selected Topics in Quantum Electronics*, 16(394), 2010.

[21] N. Engheta. Special issue on 'wave interaction with chiral and complex media'. *Journal of Electromagnetic and Waves Applications*, 6(5/6), 1992.

[22] N. Engheta. An idea for thin subwavelength cavity resonators using metamaterials with negative permittivity and permeability. *IEEE Antennas and Wireless Propagation Letters*, 1(1), 2002.

[23] N. Engheta. Circuits with light at nanoscales: Optical nanocircuits inspired by metamaterials. *Science*, 317(5845), 2007.

[24] N. Engheta and G. V. Eleftheriades. Metamaterials: Fundamentals and applications in the microwave and optical regimes. *Proceedings of the IEEE*, 99(10), 2011.

[25] N. Engheta, A. Salandrino, and A. Alú. Circuit elements at optical frequencies: nanoinductors, nanocapacitors, and nanoresistors. *Physical Review Letters*, 95(095504), 2005.

[26] N. Engheta and R. W. Ziolkowski. *Metamaterials: Physics and Engineering Explorations*. IEEE-Wiley, New York, 2006.

[27] L. A. Falkovsky and S. S. Pershoguba. Optical far-infrared properties of a graphene monolayer and multilayer. *Physical Review B*, 76(153410), 2007.

[28] L.A. Falkovsky and C. C. Persheguba. Optical far-infrared properties of a graphene monolayer and multilayer. *Physical Review B*, 76(153410), 2007.

[29] R. L. Fante and M. T. McCormack. Reflection properties of the salisbury screen. *IEEE Transactions on Antennas and Propagation*, 36(10), 1988.

[30] Z. Fei, G. O. Andreev, W. Bao, L. M. Zhang, A. S. McLeod, C. Wang, M. K. Stewart, Z. Zhao, G. Dominguez, M. Thiemens, M. M. Fogler, M. J. Tauber, A. H. Castro Neto, C. N. Lau, F. Keilmann, and D. N. Basov. Infrared nanoscopy of dirac plasmons at the graphene sio_2 interface. *Nano Letters*, 11:4701–4705, 2011.

[31] Z. Fei, A. S. Rodin, G. O. Andreev, W. Bao, A. S. McLeod, M. Wagner, L. M. Zhang, Z. Zhao, M. Thiemens, G. Dominguez, M. M. Fogler, A. H. Castro Neto, C. N. Lau, F. Keilmann, and D. N. Basov. Gate-tuning of graphene plasmons revealed by infrared nano-imaging. *Nature*, 487:82–85, 2012.

[32] J. K. Gansel, M. Thiel, M. S. Rill, M. Decker, K. Bade, V. Saile, G. von Freymann, S. Linden, and M Wegener. Gold helix photonic metamaterial as broadband circular polarizer. *Science*, 325(5947), 2009.

[33] J. D. Gaskill. *Linear Systems, Fourier Transforms, and Optics*. John Wiley & Sons, 1978.

[34] J. W. Goodman. *Introduction to Fourier Optics*. Roberts & Co. Publishers, Colorado, 2005.

[35] J-J. Greffet, M. Laroche, and F. Marquier. Impedance of a nanoantenna and a single quantum emitter. *Physical Review Letter*, 105(117701), 2010.

[36] A. G. Grushin, B. Valenzuela, and M. A. H. Vozmediano. Effect of coulomb interactions on the optical properties of doped graphene. *Physical Review B*, 80(155417), 2009.

[37] V. P. Gusynin and S. G. Sharapov. Transport of dirac quasiparticles in graphene: Hall and optical conductivities. *Physical Review B*, 73(245411), 2006.

[38] V. P. Gusynin, S. G. Sharapov, and J. P. Carbotte. Unusual microwave response of dirac quasiparticles in graphene. *Physical Review Letters*, 96(256802), 2006.

[39] V. P. Gusynin, S. G. Sharapov, and J. P. Carbotte. Magneto-optical conductivity in graphene. *Journal of Physics: Condensed Matter*, 19(2), 2007.

[40] V. P. Gusynin, S. G. Sharapov, and J. P. Carbotte. Sum rules for the optical and hall conductivity in graphene. *Physical Review B*, 75(165407), 2007.

[41] G. W. Hanson. Dyadic greens functions and guided surface waves for a surface conductivity model of graphene. *Journal of Applied Physics*, 103(064302), 2008.

[42] G. W. Hanson. Dyadic greens functions for an anisotropic, non-local model of biased graphene. *IEEE Transactions on Antennas and Propagation*, 56(3), 2008.

[43] P. A. Hidorbro, A. Y. Nikitin, C. González-Ballestero, L. Martín-Moreno, and F. J. García-Vidal. Supperradiance mediated by graphene surface plasmons. *Physical Review B*, 85(155438), 2012.

[44] P. A. Huidobro, M. L. Nesterov, L. Martín-Moreno, and F. J. García-Vidal. Transformation optics for plasmonics. *Nano Letters*, 10(1985), 2010.

[45] E. H. Hwang and S. Das Sarma. Dielectric function, screening, and plasmons in two-dimensional graphene. *Physical Review B*, 75(205418), 2007.

[46] A. Ishimaru. *Electromagnetic Wave Propagation, Radiation, and Scattering*. Prentice Hall, New Jersey, 1991.

[47] M. Jablan, H. Buljan, and M. Soljacic. Plasmonics in graphene at infrared frequencies. *Physical Review Letters*, 80(245435), 2009.

[48] Z. Jacob, L. V. Alekseyev, and E. Narimanov. Optical hyperlens: Far-field imaging beyond the diffraction limit. *Optics Express*, 14(18), 2006.

[49] B. Javidi and J.L Horner. Optical pattern recognition for validation and security verification. *Optical Engineering*, 33(6), 1994.

[50] L. Ju, B. Geng, J. Horng, C. Girit, M. Martin, Z. Hao, H. A. Bechtel, X. Liang, A. Zettl, Y. R. Shen, and F. Wang. Graphene plasmonics for tunable terahertz metamaterials. *Nature Nanotechnology*, 6:630634, 2011.

[51] J. S. Kilby. Invention of the integrated circuits. *IEEE Transaction on Electron Devices*, 23(7), 1976.

[52] J. T Kim and S-Y Choi. Graphene-based plasmonic waveguides for photonic integrated circuits. *Optics Express*, 19(24), 2011.

[53] J-T Kim, J. Kim, H. Choi, C-G. Choi, and S-Y. Choi. Graphene-based photonic devices for soft hybrid optoelectronic systems. *Nanotechnology*, 23(34), 2012.

[54] F. H. L. Koppens, D. E. Chang, and F. J. García de Abajo. Graphene plasmonics: A platform for strong light-matter interactions. *Nano Letter*, 11(8), 2011.

[55] A. E. Leanhardt, T. A. Pasquini, M. Saba, A. Schirotzek, Y. Shin, D. Kielpinski, D. E. Pritchard, and W. Ketterle. Cooling bose-einstein condensates below 500 picokelvin. *Science*, 301(5639):1513–1515, 2003.

[56] U. Leonhardt. General relativity in electrical engineering. *New Journal of Physics*, 8(247), 2006.

[57] U. Leonhardt. Optical conformal mapping. *Science*, 312(5781), 2006.

[58] Z. Q. Li, E. A. Henriksena, Z. Jiang, Z. Hao, M. C. Martin, P. Kim, H. L. Stormer, and D. N. Basov. Dirac charge dynamics in graphene by infrared spectroscopy. *Nature Physics*, 4(532), 2008.

[59] Z. Q. Li, E. A. Henriksena, Z. Jiang, Z. Hao, M. C. Martin, P. Kima, H. L. Stormer, and D. N. Basov. Supplementary information for “dirac charge dynamics in graphene by infrared spectroscopy”. http://www.nature.com/nphys/journal/v4/n7/extref/nphys989-s1.pdf, 2008.

[60] M. Liu, X. Yin, E. Ulin-Avila, B. Geng, T. Zentgraf, L. Ju, F. Wang, and X. Zhang. A graphene-based broadband optical modulator. *Nature*, 474:64–67, 2011.

[61] M. Liu, X. Yin, and X. Zhang. Double-layer graphene optical modulator. *Nano Letters*, 12:1482–1485, 2012.

[62] I. Llatsera, C. Kremersb, A. Cabellos-Aparicioa, J. M. Jornetc, E. Alarcóna, and D. N. Chigrin. Graphene-based nano-patch antenna for terahertz radiation. *Photonics and Nanostructures – Fundamentals and Applications*, 10(4):353–358, 2012.

[63] S. A. Maier. *Plasmonics: Fundamentals and Applications*. Springer, Bath, United Kingdom, 2007.

[64] K. F. Mak, M. Y. Sfeir, Y. Wu, C. H. Lui, J. A. Misewich, and T. F. Heinz. Measurement of the optical conductivity of graphene. *Physical Review Letters*, 101(196405), 2008.

[65] A. Manjavacas, P. Nordlander, and F. J. García de Abajo. Plasmon blockade in nanostructured. *ACS Nano*, 6(2):1724–1731, 2012.

[66] S. A. Mikhailov. Non-linear electromagnetic response of graphene. *Europhysics Letters*, 79(27002), 2007.

[67] S. A. Mikhailov and K. Ziegler. A new electromagnetic mode in graphene. *Physical Review Letters*, 99(016803), 2007.

[68] S. A. Mikhailov and K. Ziegler. Nonlinear electromagnetic response of graphene: frequency multiplication and the self-consistent-field effects. *Journal of Physics: Condensed Matter*, 20(384204), 2008.

[69] E. G. Mishchenko, A. V. Shytov, and P. G. Silvestrov. Guided plasmon in graphene p-n junction. *Physical Review Letters*, 104(156806), 2010.

[70] G. E. Moore. Cramming more components onto integrated circuits. *Electronics*, 38(8), 1965.

[71] A. Y. Nikitin, F. Guinea, F. J. García-Vidal, and L. Martín-Moreno. Edge and waveguide thz surface plasmon modes in graphene micro-ribbons. *Physical Review B*, 84(161407), 2011.

[72] A. Y. Nikitin, F. Guinea, F. J. García-Vidal, and L. Martín-Moreno. Fields radiated by a nanoemitter in a graphene sheet. *Physical Review B*, 84(195446), 2011.

[73] A. Y. Nikitin, F. Guinea, F. J. García-Vidal, and L. Martín-Moreno. Surface plasmon enhanced absorption and suppressed transmission in periodic arrays of graphene ribbons. *Physical Review B*, 85(081405(R)), 2012.

[74] K. S. Novoselov and A. K. Geim. The rise of graphene. *Nature Material*, 6:183–191, 2007.

[75] K. S. Novoselov, A. K. Geim, S. V. Morozov, D. Jiang, M. I. Katsnelson, I. V. Grigorieva, S. V. Dubonos, and A. A. Firsov. Two-dimensional gas of massless dirac fermions in graphene. *Nature*, 438:197–200, 2005.

[76] K. S. Novoselov, A. K. Geim, S. V. Morozov, D. Jiang, Y. Zhang, S. V. Dubonos, I. V. Grigorieva, and A. A. Firsov. Electric field effect in atomically thin carbon films. *Science*, 306(5696), 2004.

[77] L. Novotny and B. Hetch. *Principles of Nano-optics*. Cambridge University Press, New York, 2006.

[78] E. Ozbay. Plasmonics: merging photonics and electronics at nanoscale dimensions. *Science*, 311(5758), 2006.

[79] E. D. Palik. *Handbook of Optical Constants of Solids I*. Academic Press, Orlando, Florida, 1985.

[80] N. Papasimakis, Z. Luo, Z. X. Shen, F. De Angelis, E. Di Fabrizio, A. E. Nikolaenko, and N. I. Zheludev. Graphene in a photonic metamaterial. *Optics Express*, 18(8), 2010.

[81] J. B. Pendry. Negative refraction makes perfect lens. *Physical Review Letters*, 85(18), 2000.

[82] J. B. Pendry, A. Aubry, D. R. Smith, and S. A. Maier. Transformation optics and subwavelength control of light. *Science*, 337(6094), 2012.

[83] J. B. Pendry, D. Schurig, and D. R. Smith. Controlling electromagnetic fields. *Science*, 312(5781), 2006.

[84] J. B. Pendry and D. R. Smith. Reversing light with negative refraction. *Physics Today*, 57(6), 2004.

[85] N. M. R. Peres, R. M. Ribeiro, and A. H. Castro-Neto. Excitonic effects in the optical conductivity of gated graphene. *Physical Review Letters*, 105(055501), 2010.

[86] D. M. Pozar. *Microwave Engineering*. John Wiley & Sons, New Jersey, 2005. 3rd edition.

[87] M. Quinten, A. Leitner, J. R. Krenn, and F. R. Aussenegg. Electromagnetic energy transport via linear chains of silver nanoparticles. *Optics Letters*, 23(17), 1998.

[88] F. Rana. Graphene terahertz plasmon oscillators. *IEEE Transaction on Nano-Technology*, 7(91), 2008.

[89] J. Rho, Z. Ye, Y. Xiong, X. Yin, Z. Liu, H. Choi, G. Bartal, and X. Zhang. Spherical hyperlens for two-dimensional sub-diffractional imaging at visible frequencies. *Nature Communications*, 1(143):450454, 2010.

[90] R. G. Rojas. Wiener-hopf analysis of the em diffraction by an impedance discontinuity in a planar surface and by an impedance half-plane. *IEEE Transactions on Antennas and Propagation*, 36(1), 1988.

[91] N. Rotenberg, M. Spasenović, T. L. Krijger, B. le Feber, F. J. García de Abajo, and L. Kuipers. Plasmon scattering from single subwavelength holes. *Physical Review Letters*, 108(127402), 2012.

[92] Z. Ruan and S. Fan. Superscattering of light from subwavelength nanostructures. *Physical Review Letter*, 105(013901), 2010.

[93] A. Salandrino and N. Engheta. Far-field subdiffraction optical microscopy using metamaterial crystals: Theory and simulations. *Physical Review B*, 74(075103), 2006.

[94] D. Schurig, J. J. Mock, B. J. Justice, S. A. Cummer, J. B. Pendry, A. F. Starr, and D. R. Smith. Metamaterial electromagnetic cloak at microwave frequencies. *Science*, 314(5801), 2006.

[95] B. Sensale-Rodriguez, R. Yan, M. M. Kelly, T. Fang, K. Tahy, W. S. Hwang, D. Jena, L. Liu, and H. G. Xing. Broadband graphene terahertz modulators enabled by intraband transitions. *Nature Communications*, 3(780), 2012.

[96] R. A. Shelby, D. R. Smith, and S. Schultz. Experimental verification of a negative index of refraction. *IEEE Antennas and Wireless Propagation Letters*, 292(5514), 2001.

[97] A. Sihvola. Metamaterials in electromagnetics. *Metamaterials*, 1(1), 2007.

[98] A. Sommerfeld. *Partial Differential Equations in Physics*. Academic Press Inc., New York, 1949. chapter 6: Problems of Radio (English version).

[99] D. L. Sounas and C. Caloz. Edge surface modes in magnetically biased chemically doped graphene strips. *Applied Physics Letters*, 99(231902), 2011.

[100] D. L. Sounas and C. Caloz. Electromagnetic nonreciprocity and gyrotropy of graphene. *Applied Physics Letters*, 99(021911), 2011.

[101] P. Tassin, T. Koschny, M. Kafesaki, and C. M. Soukoulis. A comparison of graphene, superconductors and metals as conductors for metamaterials and plasmonics. *Nature Photonics*, 6:259264, 2012.

[102] T. N. Theis and P. M. Solomon. It's time to reinvent the transistor! *Science*, 327(5973), 2010.

[103] S. Thongrattanasiri, F. H. L. Koppens, and F. J. García de Abajo. Complete optical absorption in periodically patterned graphene. *Physical Review Letters*, 108(047401), 2012.

[104] S. Thongrattanasiri, A. Manjavacas, and F. J. García de Abajo. Quantum finite-size effects in graphene plasmons. *ACS Nano*, 6(2), 2012.

[105] S. Thongrattanasiri, Iván Silveiro, and F. J. García de Abajo. Plasmons in electrostatically doped graphene. *Applied Physics Letters*, 100(201105), 2012.

[106] A. Vakil and N. Engheta. Transformation optics using graphene. *Science*, 332(6035):1291–1294, 2011.

[107] A. Vakil and N. Engheta. Transformation optics using graphene: Supporting online material. http://www.sciencemag.org/content/332/6035/1291/suppl/DC1, 2011.

[108] A. Vakil and N. Engheta. Fourier optics on graphene. *Physical Review B*, 85(075434), 2012.

[109] A. Vakil and N. Engheta. One-atom-thick reflectors for surface plasmon polariton surface waves on graphene. *Optics Communications*, 285(16), 2012.

[110] A. VanderLugt. *Optical Signal Processing*. Wiley, New York, 1993.

[111] V. G. Veselago. The electrodynamics of substances with simultaneously negative values of ϵ and μ. *Soviet Physics Uspekhi*, 10(509), 1968.

[112] J. Wang, Y. Xu, H. Chen, and B. Zhang. Ultraviolet dielectric hyperlens with layered graphene and boron nitride. *Journal of Materials Chemistry*, 31(22), 2012.

[113] T. O. Wehling, K. S. Novoselov, S. V. Morozov, E. E. Vdovin, M. I. Katsnelson, A. K. Geim, and A. I. Lichtenstein. Molecular doping of graphene. *Nano Letters*, 8(1):173–177, 2008.

[114] P. R. West, S. Ichii, G. V. Naik, N. K. Emani, V. M. Shalaev, and A. Boltasseva. Searching for better plasmonic materials. *Laser & Photonics Reviews*, 4(6), 2010.

[115] A. R. Wright, X. G. Xu, J. C. Cao, and C. Zhang. Strong nonlinear optical response of graphene in the terahertz regime. *Applied Physics Letters*, 95(072101), 2000.

[116] H. J. Xu, W. B. Lu, Y. Jiang, and Z. G. Dong. Beam-scanning planar lens based on graphene. *Applied Physics Letters*, 100(051903), 2012.

[117] H. Yan, X. Li, B. Chandra, G. Tulevski, Y. Wu, M. Freitag, W. Zhu, P. Avouris, and F. Xia. Tunable infrared plasmonic devices using graphene/insulator stacks. *Nature Nanotechnology*, 7:330–334, 2012.

[118] X. Yang, J. Yao, J. Rho, X. Yin, and X. Zhang. Experimental realization of three-dimensional indefinite cavities at the nanoscale with anomalous scaling laws. *Nature Photonics*, 6:450454, 2012.

[119] Z. Yu, G. Veronis, Z. Wang, and S. Fan. One-way electromagnetic waveguide formed at the interface between a plasmonic metal under a static magnetic field and a photonic crystal. *Physical Review Letter*, 100(023902), 2008.

[120] W. Zhou, J. Lee, J. Nanda, S. T. Pantelides, S. J. Pennycook, and J-C. Idrobo. Atomically localized plasmon enhancement in monolayer graphene. *Nature Nanotechnology*, 7:161–165, 2012.